Oscillating Foils for Propulsion and Maneuvering of Ships and Underwater Vehicles

by

Douglas Andrew Read

B.S.in Naval Architecture and Marine Engineering
Webb Institute of Naval Architecture, 1997

Submitted to the Department of Ocean Engineering
in partial fulfillment of the requirements for the degree of

Master of Science in Naval Architecture and Marine Engineering

at the

MASSACHUSETTS INSTITUTE OF TECHNOLOGY

February 2001

Author .....
Department of Ocean Engineering
October 31, 1999

Certified by.....
Michael S. Triantafyllou
Professor of Ocean Engineering
Thesis Supervisor

Accepted by.....
Nicholas Patrikalakis
Kawasaki Professor of Engineering
Chairman, Departmental Committee on Graduate Studies

Oscillating Foils for Propulsion and Maneuvering of Ships and Underwater Vehicles

by

Douglas Andrew Read

Submitted to the Department of Ocean Engineering
on October 31, 1999, in partial fulfillment of the
requirements for the degree of
Master of Science in Naval Architecture and Marine Engineering

Abstract

Experiments were performed on a harmonically heaving and pitching NACA 0012 foil with 10 cm chord and 60 cm span. Tests to determine the thrust coefficient and propulsive efficiency of the foil were conducted over a large parameter space. This parameter space included two heave amplitudes ($h_0/c = 0.75$ and 1.00) and five phase angles ($\psi = 70°, 80°, 90°, 100°$, and 110°). Strouhal number ranged from 0.05 to 0.60 and maximum angles of attack varied between 10 and 50 degrees. Planform area thrust coefficients of 2.4 were recorded for 35 degrees maximum angle of attack and efficiencies of up to 71.5% were recorded for 15 degrees maximum angle of attack. A plateau of good efficiency, in the range of 50% to 60%, is noted. A phase angle of 100 degrees between pitch and heave is found to produce the best thrust performance. An extensive study of angle of attack profile was conducted and a simple method to estimate angle of attack for optimal thrust is presented. Higher order heave motion was implemented to alter undesirable angle of attack profiles, with encouraging results. Lift experiments were performed in the context of using the foil as a maneuvering device. Positive mean lift was achieved by adding a static bias to the foil pitch. Using this method, the foil exhibited good thrust vectoring capability. Mean lift coefficients of over 4 were achieved in this manner.

Thesis Supervisor: Michael S. Triantafyllou
Title: Professor of Ocean Engineering

Acknowledgements

Since almost all the work for this thesis was done at the tow tank during the late hours, I have to thank all my tank colleagues for their help and camaraderie. John Kumph, Alex Techet, Dave Beal, Michael Sachinis, Rocky Bryant, Jen Tam, Michael Jakuba, and Albert Wu, thanks for making a windowless basement full of water into a fun place to work. I also have to thank Sam Tolkoff and Chris Lake for invaluable advice on how to finish a thesis on time. I just hope that the tank doesn't get too boring without me, and that The Slayer Hour becomes a tank tradition.

Of course, I wouldn't have gotten anywhere without the help of my advisor, Prof Mike Triantafyllou, and research engineer, Dr. Franz Hover. Thanks for all the great ideas and for supporting me through all my work. You have to admit that all the VCTA work was a cover, though. You guys were sitting around one day and said, "Hey, I wonder how big we could make his thing....."

I would also like to acknowledge the support of MTS Systems Corporation through the George Butzow Fellowship. I acquired valuable experience during my work with the company, and the Fellowship supported a large part of my work.

Many people made my free time more exciting. Thanks to Team Fresh and *Javelin* for some great sailing and terrifying life experience. My Webb roommates (Andy, Gene, Jenny, and Roger) helped me continue the traditions we started there, and Bart, Rob, Sarah, and Karen helped make them even worse.

Of course, the real credit for keeping me at least partly sane goes to Lisa. Thanks for giving me the confidence to keep going and for understanding when we only got to see each other for 10 minutes a day. Even better, thanks for coming to get me after the T stopped running and for a great IAP in Australia!

Contents

List of Figures

List of Tables

Chapter 1

Introduction

Many animals that make their home in the air or water have evolved into astoundingly adept flyers and swimmers. These animals perform extraordinary feats of endurance and maneuverability, feats that we, as scientists and engineers, wish to understand and emulate. The basic means of locomotion involved is the oscillating foil. Many fish, birds, whales, and insects use this device in one way or another. Water borne animals use their tails and other fins for propulsion and maneuvering. Flying animals use their wings to create lift and thrust, as well as to maneuver. The performance of some of these creatures is far beyond that of vehicles designed by humans. Some fish can perform 180 degree direction changes in less than one body length, exhibiting a level of maneuverability that no ship, submarine, or AUV can match [1] . To improve the performance of our designs, we need to study and quantify the characteristics of this type of locomotion.

The basic flow mechanism of the oscillating foil is the vortex wake [9]. This wake can have two forms, one associated with drag and the other with thrust. The drag wake is analogous to the so called von Kármán street behind a bluff body. The shed vortices induce a velocity in the opposite direction of the mean flow, resulting in a mean velocity profile exhibiting a velocity deficit. Under certain conditions, an oscillating foil reverses this vortex pattern so that the vortices induce a velocity in the same direction as the mean flow. This is the thrust producing wake, which exhibits a mean velocity profile with velocity excess (i.e. a jet). As we will see in the literature

review, much research had been done to qualify the vortex shedding patterns of a foil and to determine the parameters that produce a certain vortex pattern. In this work, we will focus on describing the motion of the foil and quantifying the forces and their usefulness in the propulsion and maneuvering of a marine vehicle. We will discuss some of the results in the context of the vortex patterns predicted for our parameters.

1.1 A Review of Previous Work

Several of the relevant papers on the subject of oscillating foil propulsion focus primarily on flow visualization. Others provide both qualitative and quantitative data on thrust producing foils. We will examine a few of these papers briefly in this section. The parameters discussed in these papers are the reduced frequency (k), the Strouhal number (St), the Reynolds number (Re), the heave amplitude to chord ratio (h_0/c), the pitch angle amplitude (θ), and the mean angle of attack (α). The reduced frequency is defined as:

$$k = \frac{\omega c}{2U} \tag{1.1}$$

where ω is the frequency in rad/sec, c is the chord length in meters, and U is the free-stream velocity. The Strouhal number is:

$$St = \frac{fA}{U} \tag{1.2}$$

where f is the frequency in Hz and A is the width of the wake in meters. The wake width can be estimated using the peak to peak excursion of the trailing edge, or more simply by twice the heave amplitude. Finally, the Reynolds number is:

$$Re = \frac{Uc}{\nu} \tag{1.3}$$

where ν is the kinematic viscosity in m^2/s.

Freymuth [2] Professor P. Freymuth performed experiments on a NACA 0015 foil in both pure pitch and pure heave. These experiments focused on flow visualization,

with particular interest in leading and trailing edge vortex interaction and subsequent effect on the wake. The paper illustrates two examples.

For a heaving foil with k=2.7, Re=5200, h_0/c=0.20, and α=5 degrees, a thrust type vortex street was formed. In this case, weak leading edge separation was observed, which traveled down the foil and merged with the trailing edge vortex. This leading edge vortex reaches the trailing edge just as the next cycle starts, reinforcing the vortex forming there. For a foil pitching about the quarter-chord point with k=2.9, Re=12000, α=5 degrees, and θ=20 degrees, a similar observation was made. Again, the reverse von Kármán street was formed, with a weak leading edge vortex reinforcing the trailing edge vortex of the same sign.

It was also observed that when alpha became much larger than 5 degrees, the arrival of the leading edge vortex no longer coincided with the formation of a trailing edge vortex of the same sign. In general, Freymuth noted that large angles of attack in pitch or heave resulted in strong leading edge separation which weakened the thrust producing qualities of the vortex wake. He also noted that reducing the frequency of oscillation caused the vortex roll-up of the wake to become more and more sluggish until the von Kármán street and associated drag profile again became evident.

Koochesfahani [4] M. Koochesfahani conducted more extensive tests on a NACA 0012 foil pitching about its quarter-chord point. These tests were conducted in a low speed water channel at Reynolds number of about 12,000 and small pitch amplitudes of 2 and 4 degrees. The frequency of oscillation was gradually increased to show the transition from the drag vortex wake to the thrust vortex wake. The mean velocity profile of the wake was measured to compliment the dye visualization.

Starting with a stationary foil, the normal Kármán vortex street was observed. At low frequencies, this Kármán street was still preserved, but followed the slowly oscillating path of the trailing edge. At the smaller pitch angle, increasing the pitch frequency eventually led to a pattern in which the alternating vortices were all positioned in a straight line. This pattern occurred at a pitch angle of 2 degrees and frequency of 4 Hz and resulted in a mean velocity profile with neither velocity deficit or excess. In other words, the foil had no drag and the condition marks the transition

point between drag and thrust. Increasing the frequency beyond this point moved the vortices out of line with each other and into the thrust producing configuration. The higher the frequency, the further the vortices were moved from the centerline and the higher the thrust became. At the larger pitch angle (4 degrees), the in-line vortex pattern did not occur. Instead, two vortices of the same sign were shed on each half-cycle, resulting in four vortices shed per cycle. This pattern could be due to the leading edge vortex observed by Freymuth. In this case it is not coalescing with the trailing edge vortex at all, but instead is shed by itself to create two extra vortices per cycle in the wake. In the 2 degree pitch angle case, this pattern did not occur because the pitch angle was too small to allow strong leading edge vortices to form.

Koochesfahani shows that the frequency for vortex roll-up, and therefore the transition to thrust, decreases as the oscillation amplitude decreases. For a pitch angle of 4 degrees the transition to thrust occurs at a reduced frequency of about 3 whereas at 2 degrees of pitch angle the transition does not occur until a reduced frequency of close to 7 is reached. However, if we calculate the Strouhal number based on the peak to peak excursion of the trailing edge, the 2 degree case give St=0.11 and the 4 degree case gives St=0.10 [7].

Anderson [1] J. Anderson performed Digital Particle Image Velocimetry (DPIV) on a foil oscillating in both pitch and heave. She created a vortex pattern map showing wake patterns on a plot of Strouhal number vs. maximum angle of attack for large amplitude (h_0/c=1) motion. A breakdown of the vortex wake regions is shown in Figure 1-1. In region A, the von Kármán street along the path of the trailing edge is again evident. Region B is similar, but a weak leading edge vortex has started to form, even at low angles of attack. Region C, from St=0.20 to 0.50 and α=7 to 50 degrees, contains the two vortex per cycle reverse Kármán street. Interestingly, the constructive merging observed by Freymuth did not occur. Instead, the two-vortex jet wake was formed only by leading edge vortices. In region D, four vortices are shed per cycle, two from the leading edge and two from the trailing edge. Four vortices per cycle are also shed in region E, but at those small angles of attack they are all

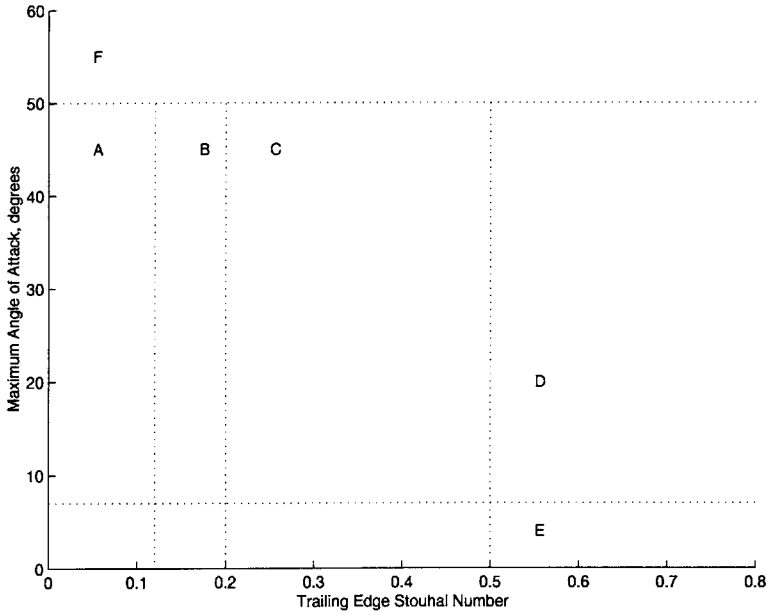

Figure 1-1: Vortex Wake Regions from Anderson

shed from the trailing edge. Finally, region F shows the "piston mode" shedding characterized by very high angles of attack ($\alpha > 50$ degrees). At these angles of attack, large leading and trailing edge vortices are shed simultaneously; the leading edge vortex does not convect down the foil chord.

While region C is the region of optimal wake pattern, the vortex interactions that create the thrust vortex wake do vary with heave amplitude. Anderson made observations in this region for three heave amplitudes. For small heave amplitude ($h_0/c = 0.25$), the jet vortex wake is dominated by trailing edge edge vortices. The upper limit of Strouhal number for Region C is pushed from 0.50 to 0.76. At a larger amplitude ($h_0/c = 0.50$), the jet is produced by both leading edge and trailing edge vortices, with same sign vortices merging at the trailing edge as shown by Freymuth. The upper Strouhal number limit is also increased for this case, up to St=0.55. Increasing the amplitude further ($h_0/c = 1.0$) results in a thrust vortex wake dominated by the leading edge vortices, with small vortices coalescing in the shear layer of the trailing edge. These observations led Anderson to conclude that even though the thrust wake is produced for several heave amplitudes, the optimum double amplitude is of the same order as the chord length.

Triantafyllou et al [7] [8] [9] Professor M. Triantafyllou and his research staff at MIT performed experiments on a NACA 0012 foil in pitch and heave. In fact, the test parameters and experimental configuration were very similar to the device used in the current investigation . The control system and several pieces of hardware are changed in our system; foil geometries are identical.

A large parameter space was tested and quantitative data supplied. Three heave amplitudes were tested, $h_0/c = 0.25$, 0.50, and 0.75. Maximum angle of attack ranged from 5 degrees to 30 degrees in 5 degree increments. Strouhal number ranged from about 0.05 to 0.55, and phase angles of 75, 90, and 105 degrees were tested.

High efficiency and thrust are reported. For $h_0/c = 0.75$, maximum angle of attack = 20.2 degrees, and phase angle = 75 degrees, a maximum efficiency of 87% was obtained at a Strouhal number of 0.30. For the same parameters at St=0.46, an efficiency of just over 80% was obtained with a thrust coefficient of approximately 0.83. The highest thrust coefficient reported was about 1.6 for $h_0/c = 0.75$, phase angle = 90, St = 0.48, and maximum angle of attack = 30 degrees. The efficiency for that run was just over 70%.

The experimental values of thrust, power, and efficiency were compared to analytical and numerical solutions. Linear theory from Lighthill [5] [6] was used for analytical prediction, while numerical simulation from Streitlein and Triantafyllou [8] was used for non-linear prediction. For the high performance parameter set described above, experimental efficiency was higher than that predicted by either linear or non-linear theory. The authors attributed this discrepancy to the formation of strong leading edge dynamic stall vortices.

Gursul and Ho [3] I. Gursul and C.M. Ho performed novel experiments on stationary airfoils in a flow of oscillating velocity. The foil was set at a given angle of attack and the incoming flow varied according to:

$$\frac{U}{U_\infty} = 1 + R\cos(\omega t) \tag{1.4}$$

where U_∞ is the average velocity, ω is the radial frequency, and R is the dimensionless

amplitude. The average lift coefficient was then defined as:

$$C_{L_{avg}} = \frac{\overline{L(t)}}{\frac{1}{2}S\rho U_\infty^2} \tag{1.5}$$

where $\overline{L(t)}$ is the time-averaged lift force.

The experiments were performed on a NACA 0012 foil with a chord of 12.4 cm, giving a Reynolds number of about 5×10^4. Results were presented for 20 degree fixed angle of attack and four values of R. The highest average lift coefficient achieved was about 2.7, occurring at the highest R of 0.70. These average lift results were plotted versus reduced frequency, and showed a well defined peak at about k = 0.80. An estimate of optimum reduced frequency, assuming that the wavelength of the vortices should be about equal to the chord length ($\lambda \approx c$), shows that this optimum value should be about one. Indeed, the experiments seem to support this estimate.

In addition to the time-averaged lift coefficient, Gursul and Ho also present interesting data on the phase-averaged lift coefficient, which quantifies the lift forces over one period. This phase-averaged lift coefficient is defined by:

$$C_L(t) = \frac{L(t)}{\frac{1}{2}S\rho U(t)^2} \tag{1.6}$$

where lift coefficient is calculated instantaneously as lift and velocity vary. Data are presented for the R = 0.70 case, at three reduced frequencies (k = 0.44, 0.60, 0.70). All values of k show a peak in the phase-average lift coefficient at around t/T = 0.50. A maximum value of about 14 was achieved for k = 0.70. Note that the maxima occur at the lowest value of U/U_∞.

The experiments of Gursul and Ho, while not directly applicable to propulsion or maneuvering, provide good insight into the high lift potential of oscillating foils and to the relevant hydrodynamic mechanisms involved.

Chapter 2

Experimental Setup and Methods

2.1 General Description

All experiments were conducted in the MIT Department of Ocean Engineering Testing Tank. The tank is equipped with a two-rail carriage system which carries the experimental device, power supplies, sensor accessories, servoamps, and a PC. Control and data collection functions are performed from an office area known as the bridge. The carriage is connected to the bridge via a 14 channel signal bus, allowing most experimental functions to be performed there. In our case the bus carried five data signals, one carriage mounted camera signal, and connected two servoamp power switches. A remote monitor and keyboard for the carriage mounted PC were located on the bridge for motion control. Another PC was used to collect the data. Preliminary data processing was performed between runs using MATLAB, and allowed us to quickly spot problems and make decisions on what parts of the parameter space to study.

2.1.1 The Testing Tank and Carriage

The tank itself is a rectangular channel of water 30 meters long by 2.6 meters wide and of variable depth. For our experiments, the water depth was around 1.4 meters. Two cylindrical carriage rails run the length of the tank. One is centered over the

tank and the other runs along the wall. The primary structure of the carriage is a 1.8 meter long aluminum box beam suspended by skateboard wheels, allowing it to roll along the overhead rail. (This box beam is labeled Main Carriage in Figure 2-1.) A horizontal structure extends from the box beam to the wall, supported by more skateboard wheels rolling on the wall mounted rail. This horizontal area provides a relatively large flat surface and space to mount the PC, servoamps, power supplies, and bus connections.

Below the main box beam, a servomotor and linear bearing table (or linear drive) are mounted vertically and suspended by a welded aluminum assembly. This arrangement is shown in Figure 2-2. The linear drive was upgraded just prior to our foil experiments. The total available horizontal travel increased from 6 inches to 12 inches, allowing us to perform tests at larger heave amplitudes than was previously possible.

In addition to the linear drive upgrade, the lower carriage was also totally redesigned. It is a rectangular aluminum box beam assembly, attached to the main carriage only through the linear drive. Thus the lower carriage and anything attached to it can move vertically within the constraints of the linear drive travel. Attached to each side of the lower carriage are aluminum plate assemblies which can clamp onto the cylindrical section of several different experimental devices. Although the new lower carriage/linear drive system appears a bit beefy for our foil device, it has several configurations and can oscillate tandem 2 meter long by 7.62 cm diameter cylinders at towing speeds up to 1.5 m/s.

Measurement of linear position was accomplished in two ways. For absolute position measurement, a Linear Voltage Differential Transducer (LVDT) was used. The tubular body of the LVDT was mounted to one of the aluminum box beams of the main carriage assembly, while the plunger was mounted directly to the lower carriage. The LVDT provided the absolute position used to center the device before each run, but it could not measure linear travel over 15.24 cm. For most of our runs the linear travel was 20 cm, so a second linear position measurement was established. This measurement used the encoder signal from the heave motor, converted to an analog

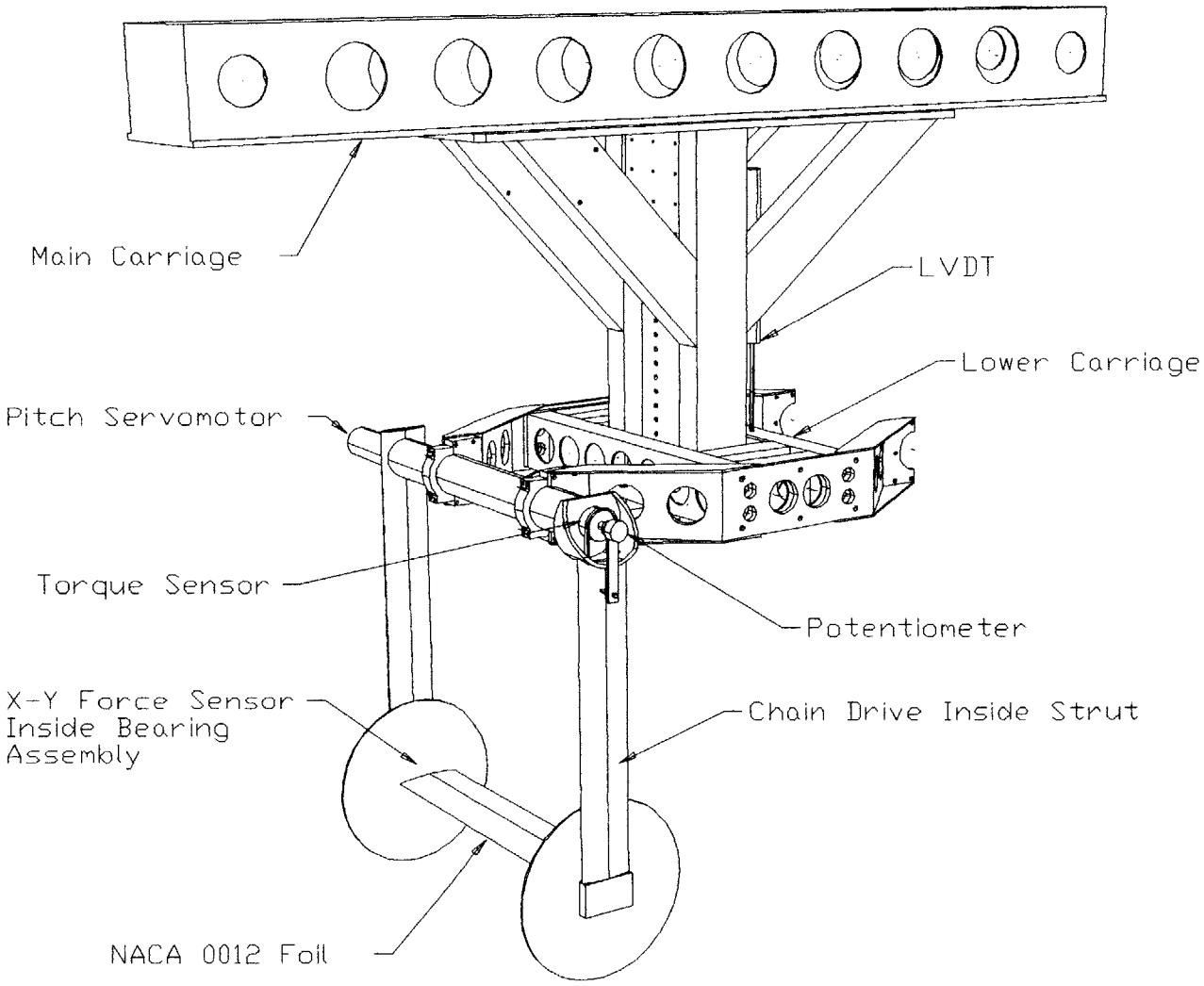

Figure 2-1: Carriage, Front View

signal by the motion control card. We will describe this measurement in more detail in Section 2.1.3.

2.1.2 The Oscillating Foil Device

As we show in Figure 2-1, the main structure of the foil device consists of two streamlined aluminum struts welded to a hollow aluminum cylinder. The foil itself is mounted to bearing assemblies at the end of each strut. The starboard bearing assembly houses a KISTLER 9117 X-Y-Z piezoelectric force sensor, attached via a preloading bolt to the bearing housing for the foil's pitch axle. The port bearing assembly contains the lower cog of the chain drive that actuates pitch motion. Since the lower carriage provides motion in the vertical direction, the foil device itself contains only the pitch drive. The pitch actuator is a Pittman servo-gearmotor located on the starboard side of the foil device, mounted coaxially with the hollow aluminum cylinder. A stainless steel driveshaft inside the cylinder connects the pitch motor to the upper cog of the chain drive. This transmission contains two torsionally rigid flexible couplings, which allow for small misalignments between the motor and upper cog bearing assembly. The chain drive runs through the port strut to the lower cog, which is rigidly attached to the foil's pitch axle.

Between the motor driveshaft and the upper cog is the torque sensor, a KISTLER model 9065. The sensor is sandwiched between two stainless steel discs, one mounted to the driveshaft and the other to the cog. A preload bolt compresses the discs and holds the assembly together. The preload bolt was specially designed to mount to the shaft of a servo-potentiometer (servopot) for angular position measurement. The body of the servopot is prevented from rotating by a small aluminum plate attached to the port strut.

The foil used for all experiments was rectangular with constant NACA 0012 section, chord 10 cm, and span 60 cm. It was constructed primarily of wood, with fiberglass cloth and resin covering. This covering provided an exceptionally smooth finish. Stainless steel axles were inserted on each end of the foil at the 1/3 chord position. The drive axle was additionally reinforced with a thin metal plate cut to

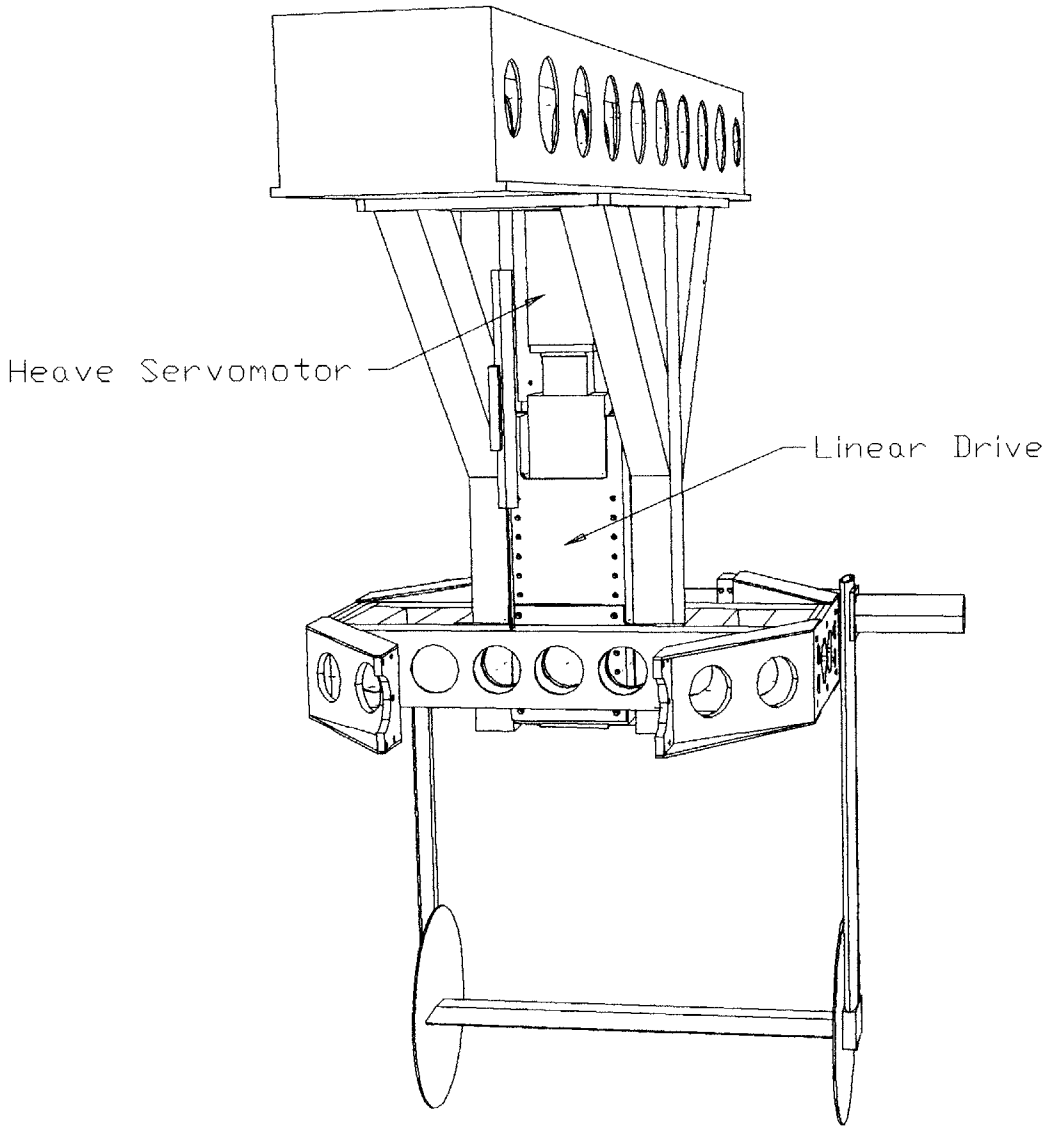

Figure 2-2: Carriage, Back View

the proper NACA 0012 section. This plate was attached to the foil with pins and then welded to the pitch axle, preventing any slippage between the axle and the foil.

As shown in Figure 2-1, plates were used on each strut to prevent flow around the ends of the foil and maintain approximately "2-D" flow. The gap between plate and foil on the port side was less than about 2 mm. The gap on the starboard side was larger, about 6 mm. To reduce this gap, a small solid wood section was constructed to fit over the axle. The section could be removed to expose the axle for hanging calibration weights.

2.1.3 Closed Loop Servo Control

Control of the system was accomplished using a Motion Engineering Incorporated (MEI) three axis, PID motion control card installed in the carriage based PC called Nautilus. A schematic of the system is shown in Figure 2-3. Control code for the foil was written in C++ and used motion duration, Strouhal number, pitch amplitude, heave amplitude, and phase angle as inputs. The code then read the voltages from the potentiometer and LVDT and centered the device using calibrated values of those voltages. Next it triggered the KISTLER charge amplifiers and awaited user input to begin the motion.

The pitch motor was a Pittman model GM14900 gearmotor with an HP 900 optical encoder. A Copley Controls model 413 servo amplifier controlled power to the motor from a 28 volt, 27 amp switching power supply. The original servo motor installed in the foil device was a Pittman 14000 direct drive model, which had no reduction gearing. After several tests using this motor, we discovered that the compliance in the system was too great. No matter how high the proportional gain was set, forces on the foil could backdrive the motor and cause errors in angular position. The 5.9:1 reduction gearing in the motor used for these experiments eliminated this problem in all but the highest load conditions.

The heave motor was a Parker model ML3475B with an optical encoder. The heave servo amplifier was a Parker model BLH150 receiving AC power from a 220 V isolation transformer mounted on the carriage. While the motor had no gearing and

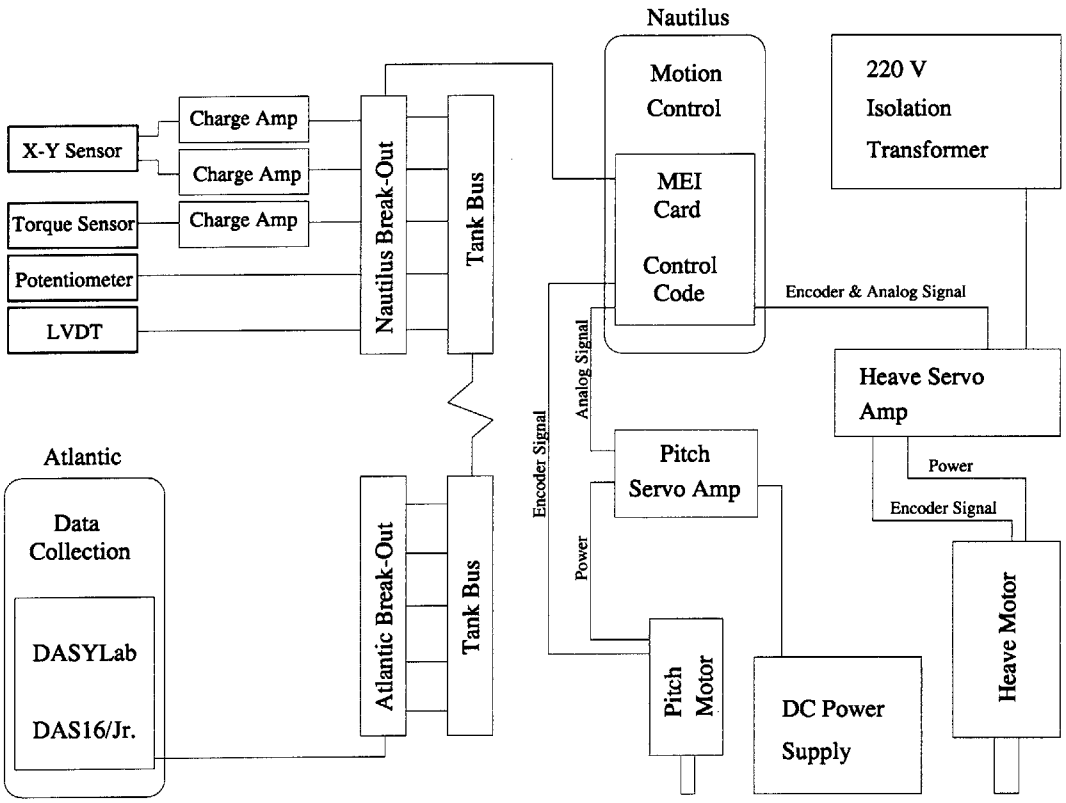

Figure 2-3: Control and Data Collection

the quadruple helix ballscrew in the linear drive provided no mechanical advantage (pitch = 1), this motor was far stronger than the pitch motor and had no noticeable compliance problems.

As mentioned earlier, the encoder signal from the heave motor was recorded as a data signal. Pitch control used axis 0 of the motion control card and heave control used axis 2. Control code was added to sample and scale the heave encoder signal and send it to axis 1. This signal was then sent to the tank bus and read by the data collection card.

2.1.4 Data Collection and Processing

Data collection was accomplished using a DAS16/Jr card and the program DASY-Lab in the bridge computer called Atlantic. The card collected and recorded six data signals simultaneously: Y force, Torque, X force, Pitch position, Heave position (encoder), and Heave position (LVDT). This system is also presented in Figure 2-3.

X, Y, and Torque signals from the KISLTER sensors pass through charge amplifiers and are then passed to the tank bus. The Potentiometer and LVDT were powered by external sources so that a varying voltage is passed to both Nautilus (for absolute positioning) and the tank bus. The encoder signal from axis 1 of the motion control card is also sent to the bus. On the bridge, all six channels from the bus are connected to the Atlantic break-out panel and read by the data collection card. The sampling rate was 200 Hz.

An example of the recorded raw data for a typical propulsion run is shown in Figure 2-4. The data are unprocessed, so the vertical scale is in volts. The horizontal scale is in samples, so at 200 Hz the total time for each run is just over 50 seconds. The typical testing procedure started by entering the parameters for the run and centering the device. The code would trigger the sensors at this point and wait for user input. DASYLab was then started and allowed to record data for about five to ten seconds before carriage motion began. The actual foil oscillation started after another five to ten seconds, giving us a period of steady forces on the foil. The foil then oscillated for the prescribed duration. Once the motion was finished, the control code waited three seconds and disabled the force sensors. After another three to five seconds, DASYLab was stopped and the file was saved. Note that transients at the beginning of the foil motion are small. The equations of motion were multiplied by $1 - e^{-t}$ in the control code to create a sort of ramp for the oscillation. This ramp prevented large transients and eased the mechanical burden on the system, especially at high Stouhal Numbers.

Data processing was accomplished using the program MATLAB. Scripts were written to read, parse, and plot the data, as well as to perform the necessary computations. Data were not filtered for the purpose of calculation. Data displayed in the appendix were filtered using a low-pass, zero phase distortion filter in MATLAB. The necessary derivatives were calculated using a simple center-difference scheme. A calibration matrix was loaded automatically to convert voltages into forces and positions.

The data were centered by the initial zero created before carriage motion started.

This point is important, especially concerning the X or thrust force. Zeroing the data before any motion starts ensures that the drag on the foil will be included in the thrust calculation. Zeroing the data with the portion of the signal after carriage motion starts (before oscillation) excludes this drag and leads to an artificially high value of mean thrust.

2.2 Calibration

2.2.1 Sensor Linearity

All force and position sensors were checked for linear behavior. Force sensors were tested using several known weights, while position sensors were tested against known angles and distances. To find given angles and distances, the encoders on each motor were used. By knowing the number of counts per revolution for each encoder, the sensors could be moved accurately to a given position. This method was checked against known distances and angles, i.e. a ruler and protractor. All sensors exhibited good linearity, within 1.5%. Figures 2-5 to 2-9 show the results of these tests.

All sensors were calibrated before a set of tests were conducted. If a set of experiments lasted several days, calibrations were performed at least every other day. Calibration matrices were written each time to be used in the processing of the data. The values in the calibration matrix were based on a graphical user input, i.e. the user picked loaded and unloaded levels from a graph and MATLAB calculated the difference in voltage for a given weight. The calibration values were consistent from day to day, exhibiting less than 3% drift. Part of this drift could be attributed to slight differences in user input.

In addition to the calibrations above, the pitch zero position was carefully set before each set of experiments. Since the foil was symmetric, it should not produce any lift at zero angle of attack. By measuring the lift on the foil in a steady towing experiment, the pitch zero could be adjusted until the foil produced no lift.

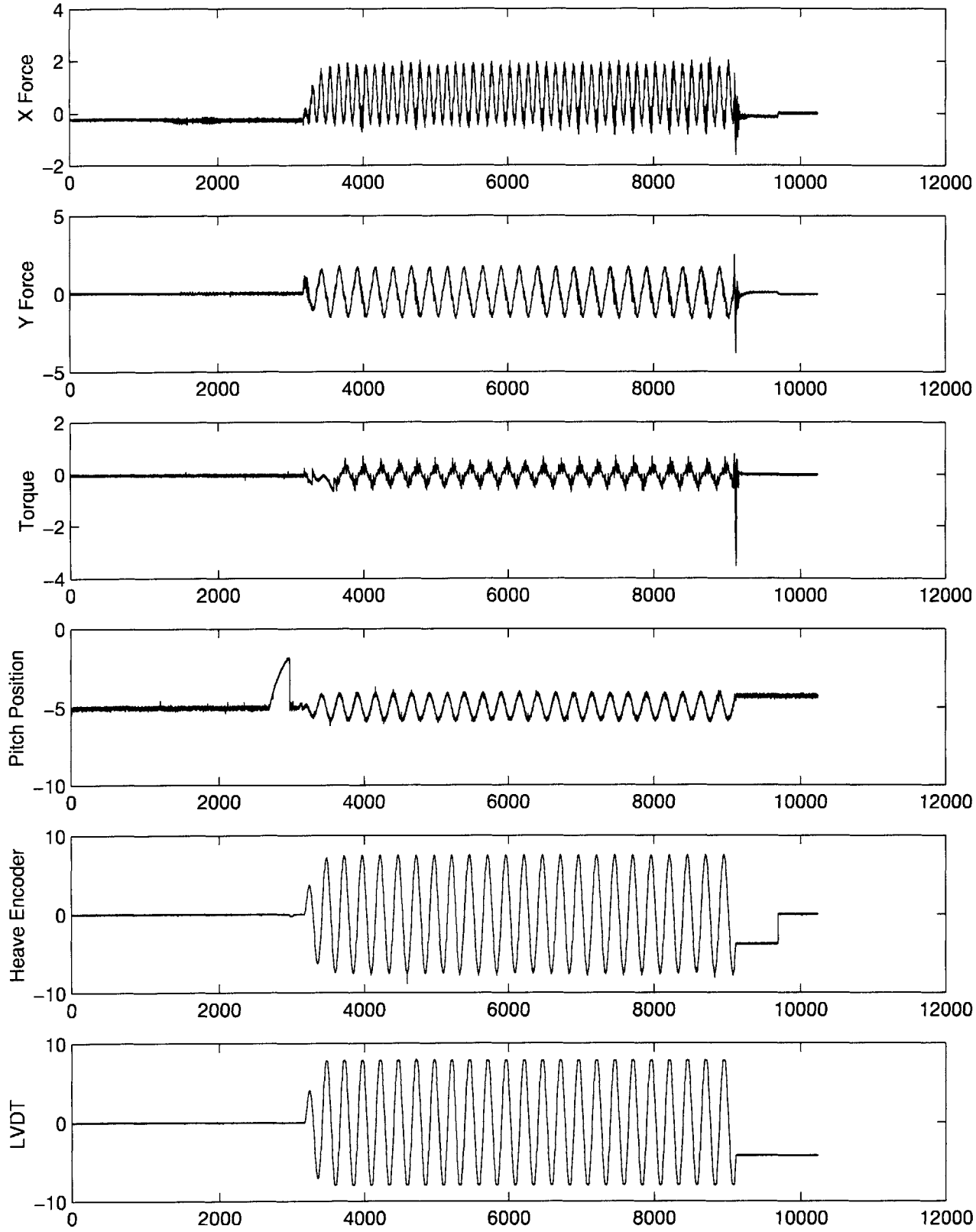

Figure 2-4: Raw Data

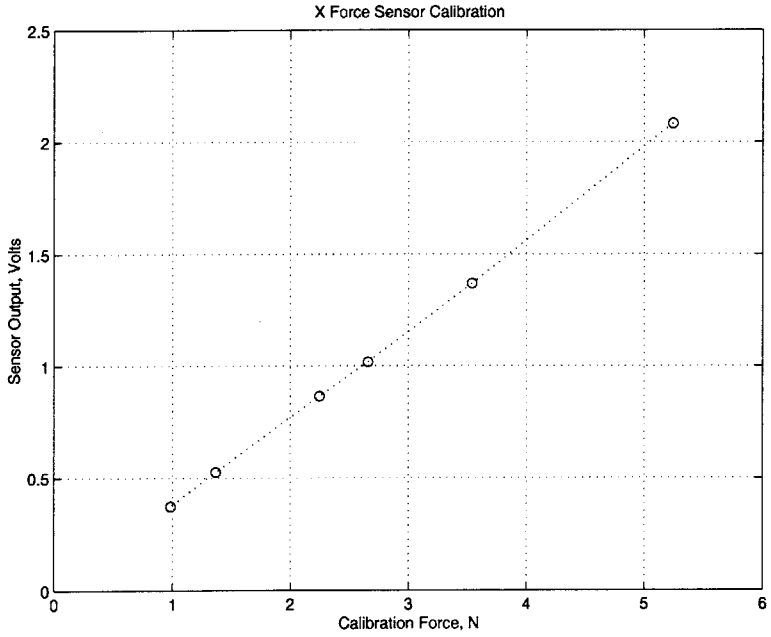

Figure 2-5: Sensor Linearity, X

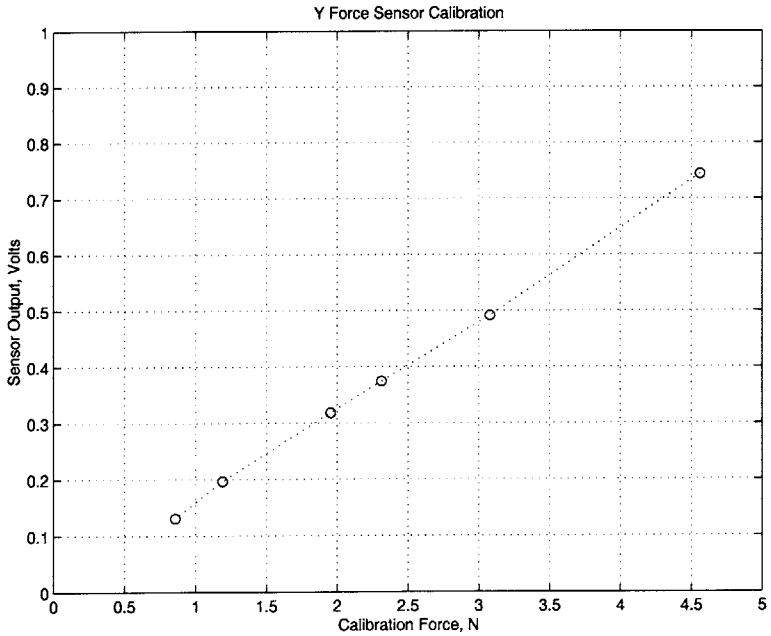

Figure 2-6: Sensor Linearity, Y

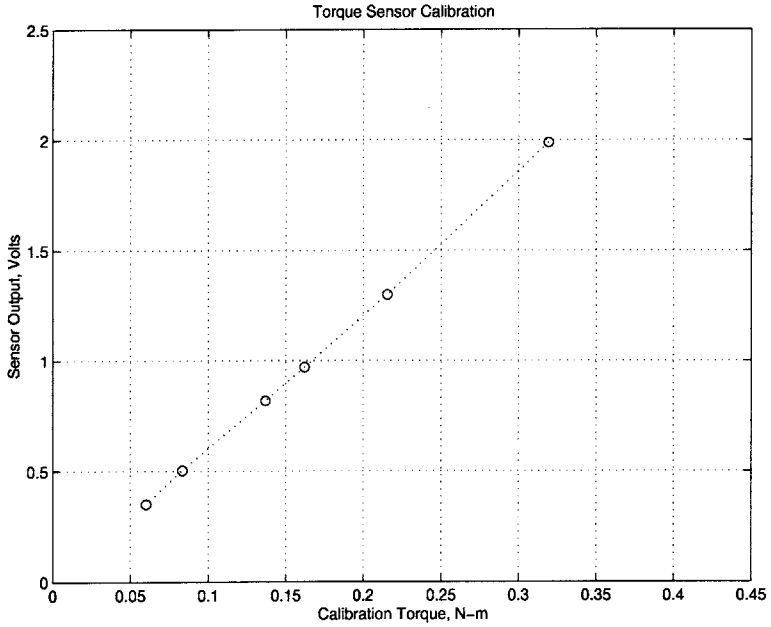

Figure 2-7: Sensor Linearity, Torque

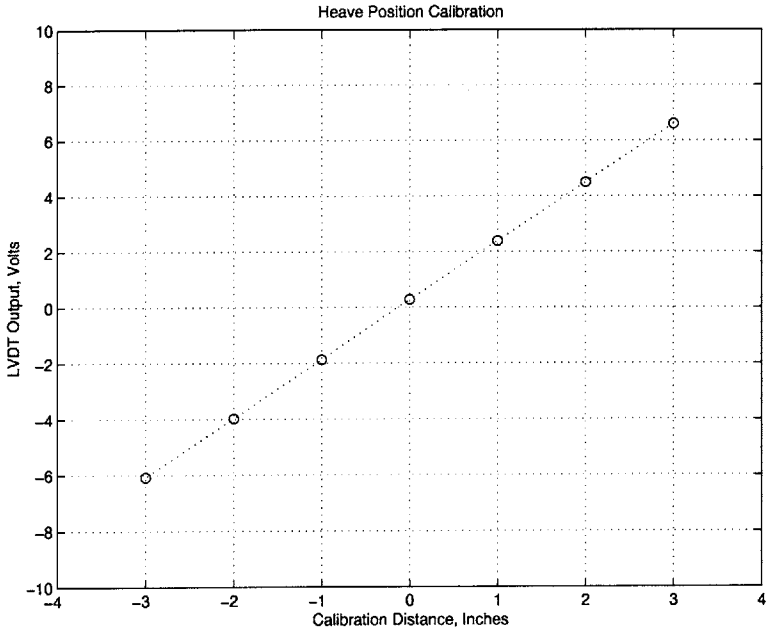

Figure 2-8: Sensor Linearity, Heave (LVDT)

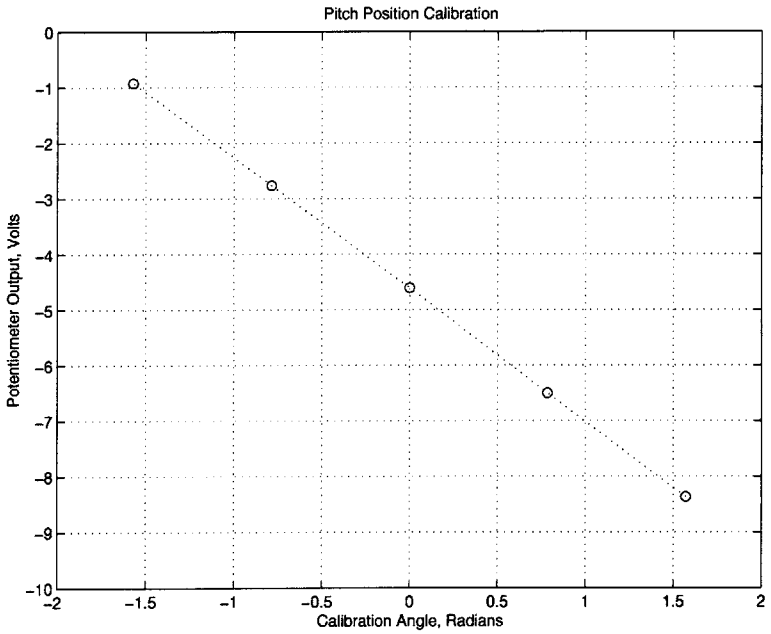

Figure 2-9: Sensor Linearity, Pitch (Potentiometer)

2.2.2 Compensation for One Force Sensor

The mechanical setup of the system, particularly the pitch drive system running through the starboard strut, prevents us from easily installing force sensors at both ends of the foil. When calibrating the X and Y force sensor in the port strut, we hung a weight from the X-Y sensor end of the foil and assumed that the foil was simply supported at each axle. This means that a weight hung at the center of the foil would be evenly distributed at each end. If this premise were true, the force sensor would only see half of the weight actually acting on the foil during a run. We could compensate for this problem by simply doubling the signal from the X and Y force sensor. To validate this assumption, weights were hung at five points along the foil, in quarter chord intervals. The force measured by the sensor when the weight is in the middle of the foil should be half the force measured when the weight is hanging on the port axle. The measured values were off by 0.2% in X and 2.6% in Y. This discrepancy is small for X and acceptable for Y. Results for these tests are shown in Figures 2-10 and 2-11.

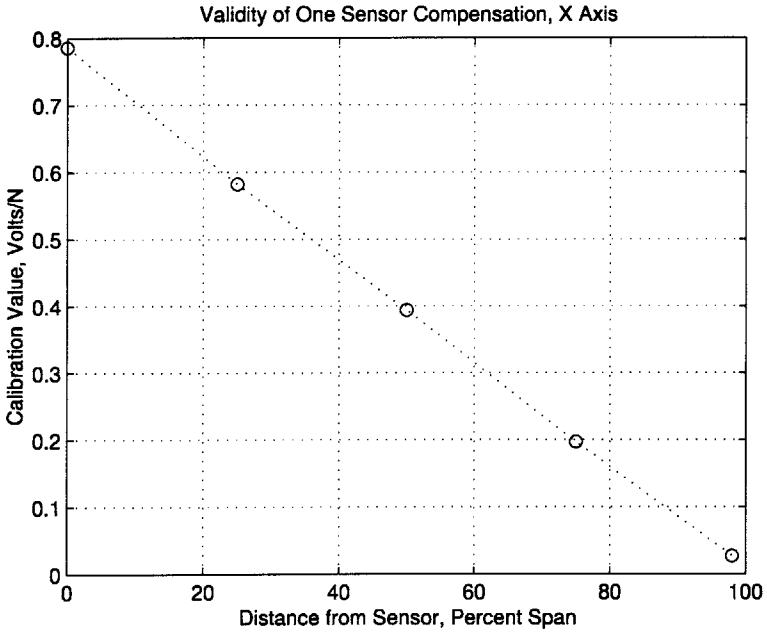

Figure 2-10: Compensation for One Sensor, X

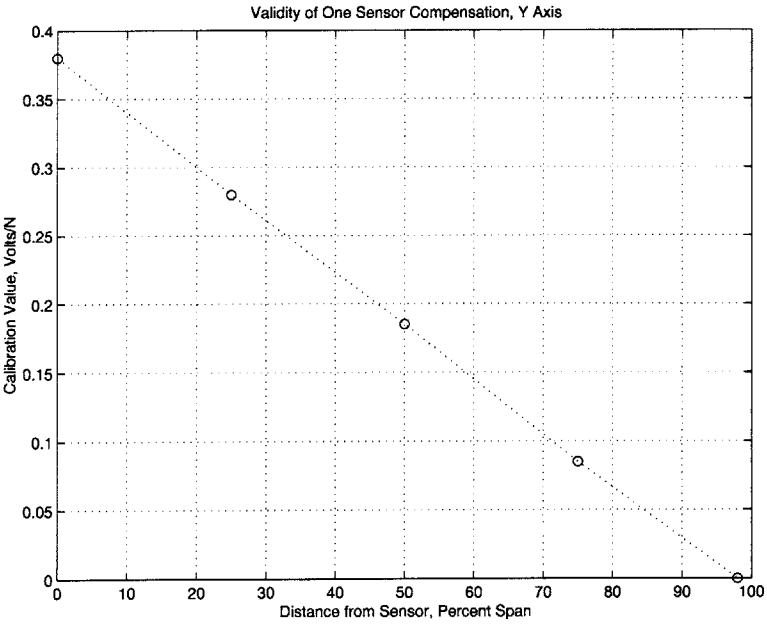

Figure 2-11: Compensation for One Sensor, Y

2.3 Definitions

Before continuing on with the parametric study and results calculations, we need to define a few of the parameters that will be used in the next sections. On of the most important parameters in this study is the Strouhal Number:

$$St = \frac{2h_0 f}{U} \tag{2.1}$$

where h_0 is the heave amplitude in meters, f is the frequency in Hz, and U is the velocity in meters/second. The $2h_0$ term is really an estimate of the width of the foil wake. Since we don't actually know what this value is without some kind of visualization method, we must come up with an approximation. The peak to peak excursion of the trailing edge can also be used, but it is a function of several of the test parameters. Within the parameter space tested, $2h_0$ is a valid estimate of this value. Data for converting between trailing edge Strouhal number and double heave Strouhal number are presented in Appendix D.

Almost all the data presented here will be in non-dimensional form. Force data was reduced to coefficient form using the following equation:

$$C_F = \frac{F}{\frac{1}{2}\rho U^2 cs} \tag{2.2}$$

where ρ is the density of water in kg/m^3, c is the foil chord in meters, and s is the foil span in meters. In most cases U is the towing velocity in m/s. For impulse start experiments where the carriage speed was 0, U is the maximum heave velocity in m/s. F is the measured force, in Newtons. In this work, F can be the total force on the foil or it can be separated into X and Y components. In the case of the latter, C_X would be the drag or thrust coefficient and C_Y would be the lift coefficient. This force can also be the instantaneous force in time or the average over one period.

Chapter 3

Parametric Study

3.1 Equations of Motion

Most experiments were conducted using simple sinusoidal harmonic motion. The heave motion as a function of time, t is

$$h(t) = h_0 \sin(\omega t) \tag{3.1}$$

where h_0 is the heave amplitude in meters, ω is the frequency in rad/sec, and time, t is in seconds. The pitch motion is then

$$\theta(t) = \theta_0 \sin(\omega t + \psi) \tag{3.2}$$

where θ_0 is the pitch amplitude in radians and ψ is the phase angle between pitch and heave in radians.

While these equations appear to be harmless, the resulting angle of attack profile can take several different forms. Thus it is important to know what angle of attack will result from a given combination of parameters. For a foil undergoing only a heave motion, the angle of attack as a function of time is

$$\phi(t) = \arctan\left(\frac{\dot{h}(t)}{U}\right) \tag{3.3}$$

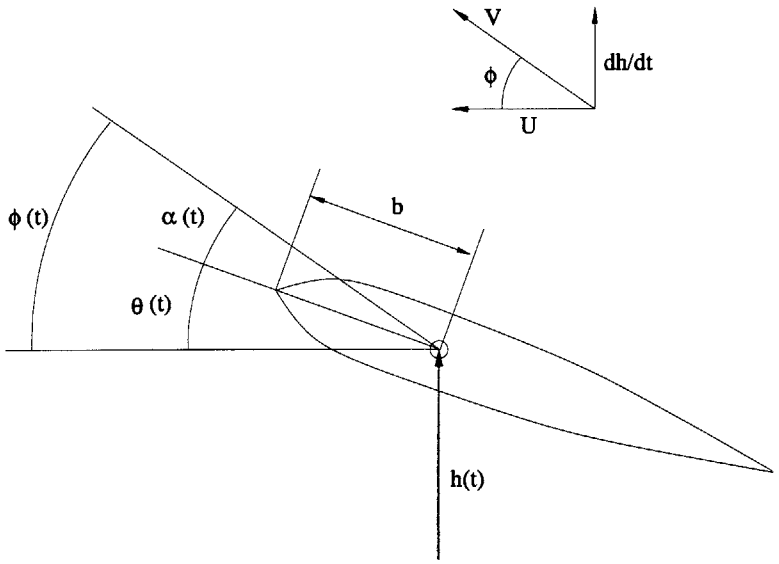

Figure 3-1: Foil Parameters

where U is the forward velocity in meters/sec and $\dot{h}(t)$ is the heave velocity as a function of time. We show the foil parameters in Figure 3-1, as well as the instantaneous velocity vector. Pitching the foil (using a positive θ_0) decreases the angle of attack and thus for a heaving and pitching foil, we subtract the angle of attack due to pitch from the angle of attack due to heave:

$$\alpha(t) = \phi(t) - \theta(t) \tag{3.4}$$

$$\alpha(t) = \arctan\left(\frac{\dot{h}(t)}{U}\right) - \theta(t) \tag{3.5}$$

Leaving us only to solve the simple derivative for heave velocity, which is

$$\dot{h}(t) = h_0\omega\cos(\omega t) \tag{3.6}$$

Substituting equations 3.6 and 3.2 into 3.5, we arrive at the equation defining one of our test parameters, the maximum angle of attack achieved over one period, T:

$$\alpha_{max} = 0 \overset{max}{\rightarrow} T \left\{\arctan\left(\frac{h_0\omega\cos(\omega t)}{U}\right) - \theta_0\sin(\omega t + \psi)\right\} \tag{3.7}$$

The occurrence of the maximum angle of attack varies greatly over the parameter

set. In fact, the above equation has two solutions over a large range of frequencies. We will investigate this behavior in detail in the next section.

3.2 Relevant Variables

We can see from equation 3.7 that the variables for each experiment are:

- Frequency, ω
- Heave Amplitude, h_0
- Pitch Amplitude, θ_0
- Phase Angle, ψ
- Towing Speed, U
- Time, t

All propulsion experiments were conducted at a towing speed of 0.40 m/s. Each run was limited in time by either the number of points that could be stored by the motion control card or the length of the tank and towing speed. High frequency runs were as short as 20 seconds, while low frequency runs were 30 seconds. With duration and towing speed set, we are left with four parameters to specify for each experiment. The frequency is non-dimensionalized with the towing speed and heave amplitude, giving us Strouhal number. θ_0 is calculated to give a desired maximum angle of attack. Heave amplitude is non-dimensionalized with chord length. The inputs specified to describe the motion then become:

- Strouhal Number, St
- Heave/Chord Ratio, h_0/c
- Maximum AoA, α_{max}
- Phase Angle, ψ

The range of the parameter space for these experiments is as follow:

- Strouhal Number, 0.10 to 0.60 (0.02 increment)
- Heave/Chord Ratio, 0.75 and 1.00
- Maximum AoA, 10° to 50° (5° increment)
- Phase Angle, 70° to 110° (10° increment)

At a minimum of two runs per unique parameter set, this is a very large test matrix. As we will see later, this number is substantially reduced by the fact that some angles of attack cannot be achieved above a certain Strouhal Number. Mechanical limitations also played a roll. The maximum Strouhal Number was about 0.42 for $h_0/c = 0.75$ because of an upper limitation on frequency. At $h_0/c = 1.00$ this limit gave Strouhal Numbers up to the value of 0.60 stated above.

3.3 Solving for θ_0

As stated in Section 3.1, the form of the angle of attack profile varies greatly over the parameter space. In addition, we want to define the maximum angle of attack achieved over one period as a test parameter. To this end, we must study equation 3.7 in great detail:

$$\alpha(t) = \left\{ \arctan\left(\frac{h_0 \omega \cos(\omega t)}{U} \right) - \theta_0 \sin(\omega t + \psi) \right\} \tag{3.8}$$

Looking at our four test parameters, we see that we wish to solve for the θ_0 that will give a specific maximum angle of attack for given Strouhal Number, heave/chord ratio, and phase angle. Since the Strouhal Number is a function of the heave amplitude, it is not independent of the heave/chord ratio. Thus the solution of θ_0 for a given Strouhal number and phase angle is independent of h_0/c.

To solve for θ_0, numerical schemes were implemented. A Microsoft Excel Macro using the Goal Seek function works quite well for this task, but almost any iterative solver will do. Figures 3-3 and 3-4 show the result of θ_0 calculations for maximum angles of attack of 15 and 25 degrees. We show here that phase angle has a large

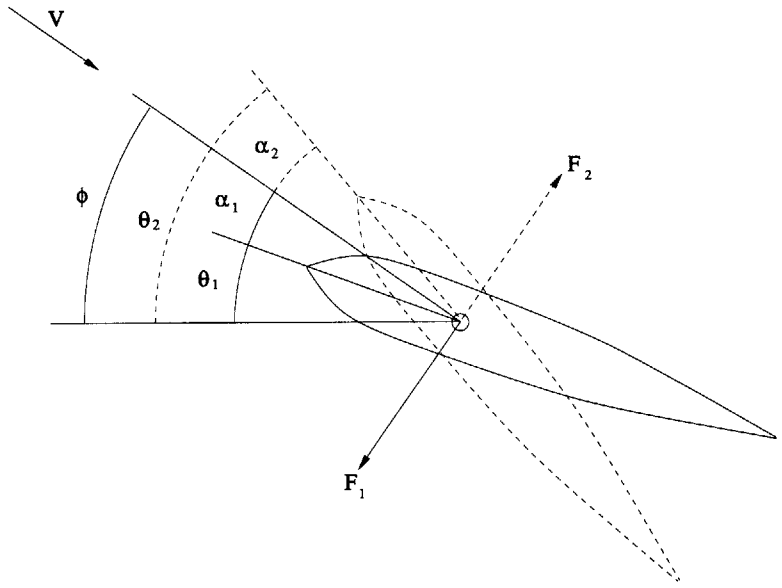

Figure 3-2: Both Angle of Attack Solutions

effect on the θ_0 required for a given maximum angle of attack. Also, θ_0 is symmetric about 90 degrees phase angle. The solution is the same for 80 and 100 degrees, i.e. 90 $\pm$10 degrees.

Of great interest is the fact that beyond a certain Strouhal Number, the solution did not converge for the desired maximum angle of attack. At a phase angle of 70 degrees, for example, a maximum angle of attack as low as 15 degrees cannot be obtained above a Strouhal Number of 0.25. In other words, there is a minimum value of the maximum angle of attack for a given set of parameters. This fact will be illustrated further in the next section.

The dotted line in Figures 3-3 and 3-4 represents an estimate of θ_0 that may be made from equation 3.4. Rearranging, we get:

$$\theta(t) = \phi(t) - \alpha(t) \tag{3.9}$$

As we have already noted:

$$\tan(\phi) = \left(\frac{h_0 \omega \cos(\omega t)}{U} \right) \tag{3.10}$$

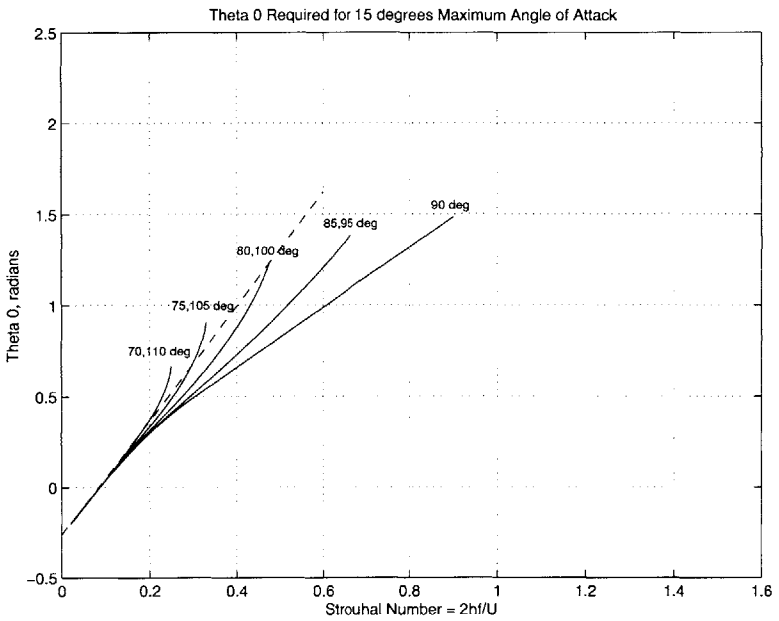

Figure 3-3: θ_0 Required for 15° Maximum Angle of Attack

The maximum value of this equation is:

$$Max(\tan\phi) = \left(\frac{h_0\omega}{U}\right) \tag{3.11}$$

Using Equation 3.9, we see that:

$$Max(\theta(t)) = Max(\phi(t) - \alpha(t)) \tag{3.12}$$

Finally, if $h_0\omega/U$ is small, $\tan\phi \approx \phi$. Substitution gives:

$$\theta_0 = \left(\frac{h_0\omega}{U}\right) - \alpha_0 \tag{3.13}$$

Remembering that $\omega = 2\pi f$ and $St = 2h_0 f/U$, we arrive at a simple, linear estimate for θ_0:

$$\theta_0 = St\pi - \alpha_0 \tag{3.14}$$

As we show in Figures 3-3 and 3-4, this estimate is only valid up to Strouhal Numbers of about 0.20. Unfortunately, the range of interests for these experiments is from Strouhal Numbers of about 0.20 to 0.60. Worse, it doesn't make a good initial guess

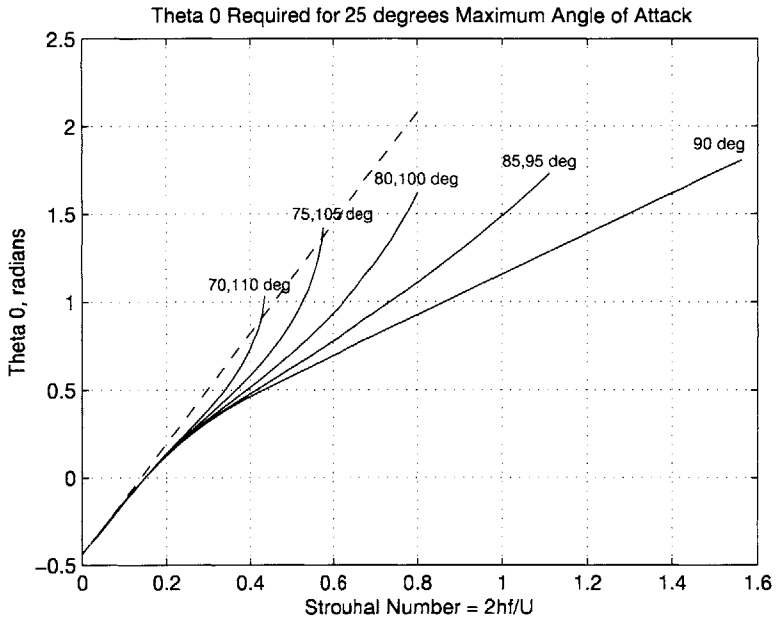

Figure 3-4: θ_0 Required for 25° Maximum Angle of Attack

for our iterative solver since there are two solutions to the angle of attack equation. The problem is that $h_0\omega/U$ is not really small in the range tested. Using the equation:

$$\theta_0 = \arctan(St\pi) - \alpha_0 \tag{3.15}$$

is not really any more complex than Equation 3.14, and provides the correct result if the phase angle is 90 degrees. At other phase angles, Max $\theta(t)$ is still θ_0, but it no longer occurs at the same point in the cycle as Max $\phi(t)$ and we must use Equation 3.8.

The double solution to the angle of attack equation results from the fact that the foil can always be pitched up or down with respect to the instantaneous oncoming flow. Think of a steady airfoil having either a positive or negative angle of attack, producing either lift (as in an aircraft) or a down force (as in a race car). Analogously, the oscillating foil can have two θ_0 solutions producing the same maximum angle of attack. One solution will orient the foil in a thrust producing position, while the other will result in a drag producing position (see Figure 3-2).

Figure 3-5 shows a more complete version of 3-3, with both θ_0 solutions shown.

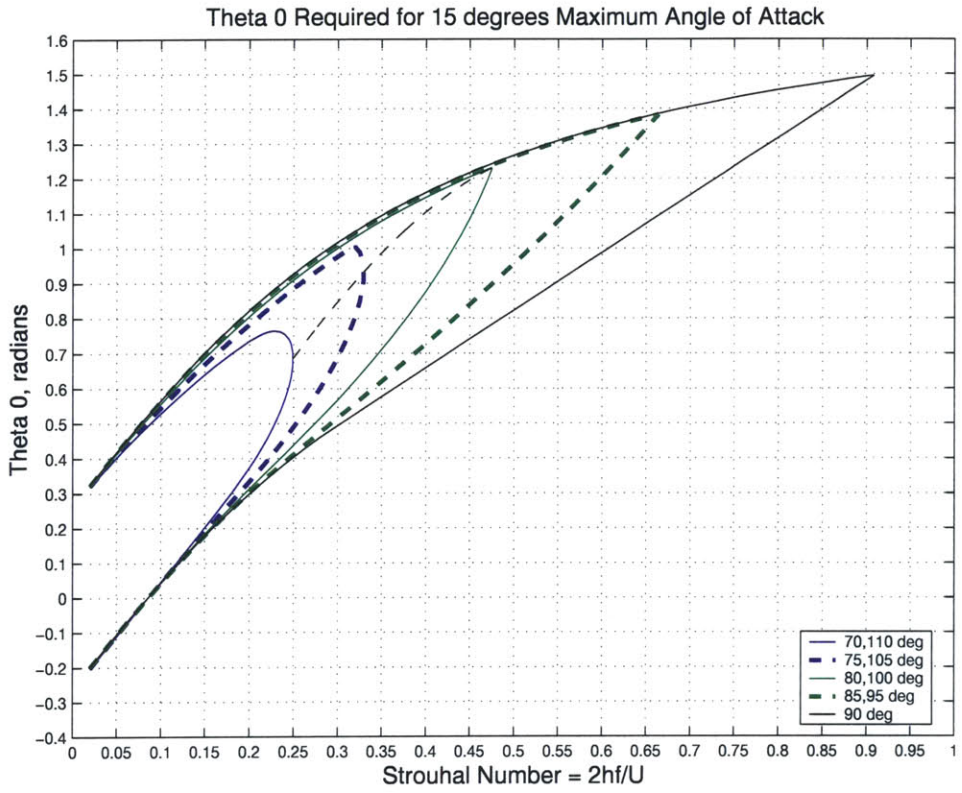

Figure 3-5: Bifurcation of Angle of Attack Equation showing both thrust and drag producing solutions

The thin dotted line connects the points where the thrust and drag producing values of θ_0 converge for each phase angle. As we will see, the closer one gets to one of these convergence points, the lower the thrust producing performance of the foil.

3.4 Resulting Angle of Attack Profiles

The angle of attack profile can take several forms. In the following figures, we show the relation between the selected parameters and the resulting profile. We will refer to Figure 3-5 to map each parameter variation onto the parameter space.

In Figure 3-6, Strouhal Number and phase angle are held constant while θ_0 varies from 0.55 to 1.15. This set of θ_0 values covers the entire range from thrust production, through the minimum value of maximum angle of attack, to drag production. Following a line of constant Strouhal Number (St = 0.30) on Figure 3-5, we see the result of each θ_0 and the relation to the plotted contours:

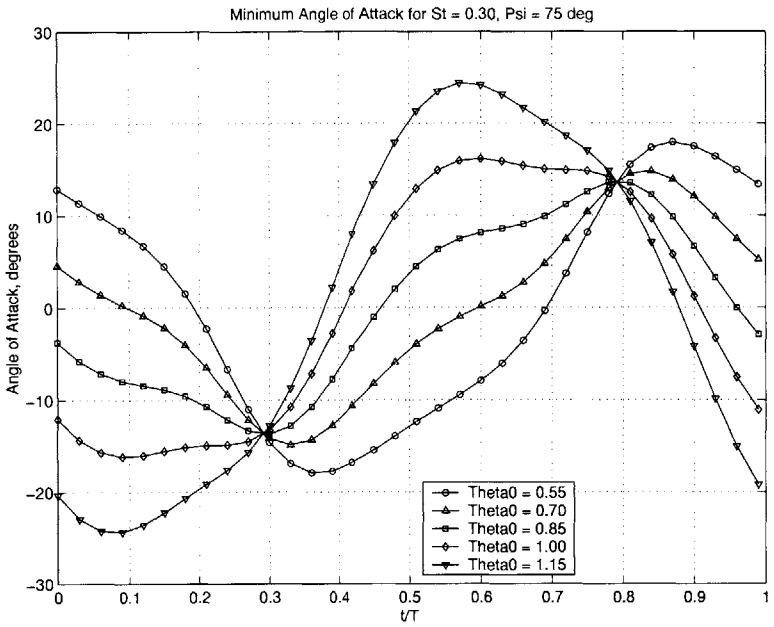

Figure 3-6: Angle of attack profile showing result of increasing θ_0 for St = 0.30, $\psi = 75°$.

- $\theta_0 = 0.55$, below the calculated contour for thrust production at $\psi = 75°$, $AoA_{max} > 15°$
- $\theta_0 = 0.70$, on the calculated contour for thrust production at $\psi = 75°$, $AoA_{max} \approx 15°$
- $\theta_0 = 0.85$, near the convergence point for drag and thrust production, $AoA_{max} \approx 14°$(minimum value)
- $\theta_0 = 1.00$, on the calculated contour for drag production at $\psi = 75°$, $AoA_{max} \approx 15°$
- $\theta_0 = 1.15$, above the calculated contour for drag production at $\psi = 75°$, $AoA_{max} > 15°$

Thus for a gradual increase of θ_0, the lowest maximum angle of attack obtained was about 14°. We illustrate, therefore, that for this phase angle and Strouhal Number, maximum angles of attack less than 14° are not possible using this motion.

In Figure 3-7, Strouhal Number is held constant and θ_0 is selected such that the maximum angle of attack is also constant. Phase angle varies from 70° to 110° in

20° increments, showing the result of phase angles less than or more than 90°. For reference, the heave position is plotted as a solid line. Looking at Figure 3-5, we see that each angle of attack profile falls exactly on the contour for that phase angle at $St = 0.20$. The effects of phase angle are clear:

- $\psi = 70°$, Maximum absolute angle of attack occurs before the heave zerocrossing.
- $\psi = 90°$, Maximum absolute angle of attack occurs at the heave zerocrossing.
- $\psi = 110°$, Maximum absolute angle of attack occurs after the heave zerocrossing.

It should be noted that the heave downcrossing and upcrossing is the point of highest heave velocity. In general, having the highest angle of attack occur at the highest heave velocity should produce the larger force. All other things being equal, we expect a phase angle of 90° to produce the largest thrust.

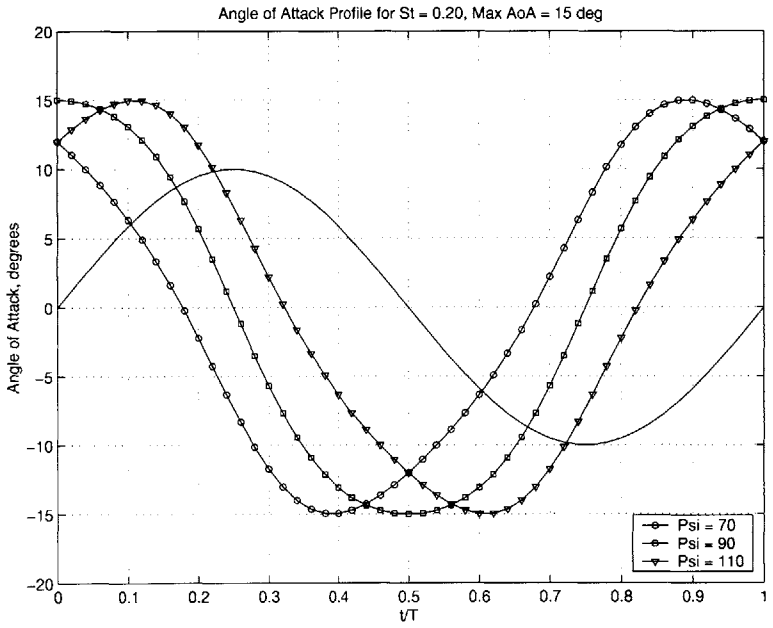

Figure 3-7: Angle of attack profile showing result of varying phase angle for St = 0.20, Max AoA = 15°.

In Figures 3-9 and 3-8 we show the evolution of the angle of attack profile *along*

one of the phase angle contours of Figure 3-5. θ_0 is adjusted over the range of Strouhal Numbers so that the maximum angle of attack remains constant. The goal is to see what happens to the angle of attack profile as we approach the convergence of drag and thrust producing θ_0 values along the thrust producing branch of the contour.

In Figure 3-8 we show this evolution for a phase angle of 90° and constant maximum angle of attack of 15°, following the contour of Figure 3-5 from a Strouhal Number of 0.10 to its termination at 0.908. We note the following:

- Low Strouhal Number (St = 0.10), Angle of Attack is sinusoidal with Max AoA occurring at T/2.
- Intermediate Strouhal Number (St = 0.30), Angle of Attack is flattened sinusoid with Max AoA occurring over about 40% of T.
- High Strouhal Number (St = 0.50), Angle of Attack begins to show multiple peaks per cycle.
- Very High Strouhal Number (St = 0.70 to 0.908), Max Angle of Attack occurs six times per cycle.

It is interesting to note the behavior of the angle of attack at the termination Strouhal Number of 0.908. As stated above, the angle of attack reaches the maximum value of 15° six times over one period, while heave and pitch maxima occur only twice per period.

In Figure 3-9 we note similar trends. Phase angle is now 80° and maximum angle of attack is again 15°. As we noted earlier, the maximum Strouhal Number for that angle of attack decreases at phase angles lower or higher than 90°. Looking at Figure 3-5, we follow the contour for $\psi = 80°$ from a Strouhal Number of 0.25 to its termination at 0.475.

At low Strouhal Number, we see the same deformed sinusoid noted in Figure 3-7. As Strouhal Number increases, a multi-peaked profile again appears. Unlike the previous example at 90° phase angle, the maximum angle of attack is never reached

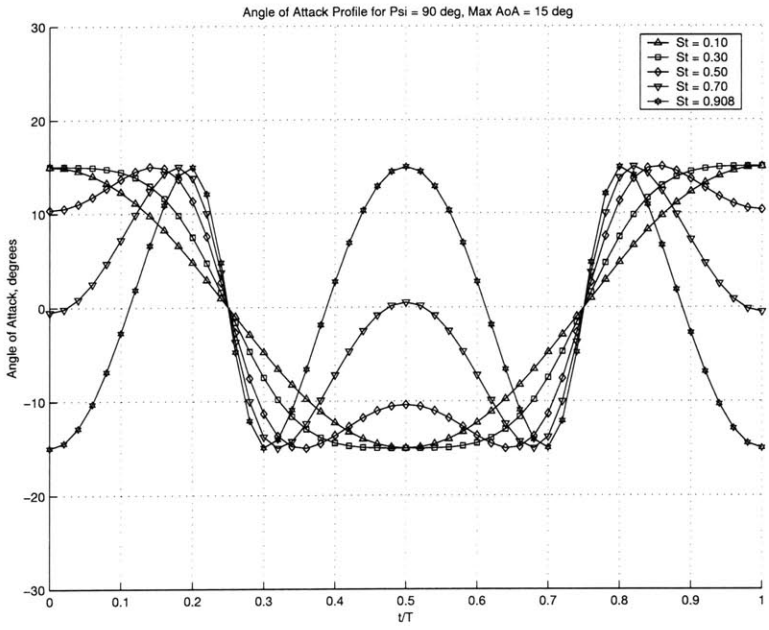

Figure 3-8: Angle of attack profile showing result of increasing Strouhal number for $\psi = 90°$, Max AoA = 15°.

more than four times in one period. Of special interest is the profile where St = 0.40. In most cases, the angle of attack has a value of zero for only an instant. In this instance we see an angle of attack profile that is nominally zero for about 20% of one period. In addition, the angle of attack is quite low ($\approx 2°$) at the maximum heave velocity. We would not expect this case to produce large amounts of thrust. By inspecting the angle of attack profile, we can get an idea of what performance to expect from a given set of parameters.

Figure 3-10 takes this inspection one step further, following the same contour as Figure 3-9 but then backing up along the drag producing branch. In other words we trace the same thrust producing θ_0 contour as before, from St = 0.25 to 0.475, then reverse direction from the termination Strouhal Number and follow the drag producing θ_0 from St = 0.475 to 0.25.

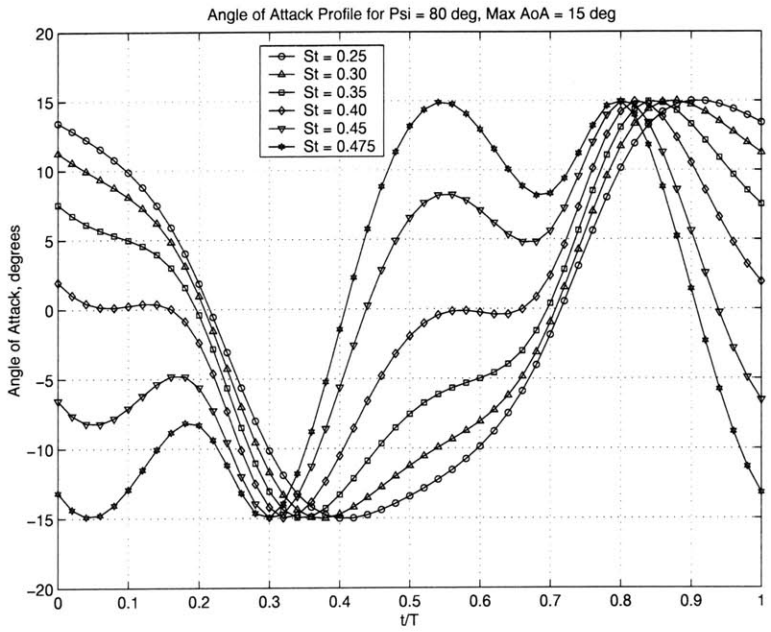

Figure 3-9: Angle of attack profile showing result of increasing Strouhal number for $\psi = 80°$, Max AoA $= 15°$.

3.5 Higher Order Equations of Motion

As we will see in Chapter 4, the thrust producing performance of a given set of parameters tends to decrease when the angle of attack profile takes on the multi-peaked forms discussed above. In order to recover performance at higher Strouhal Numbers, we need to alter the angle of attack profile so that it again resembles a sinusoid. The problem lies in the first term of equation 3.8, which is:

$$\arctan\left(\frac{\dot{h}(t)}{U}\right) \tag{3.16}$$

The goal is to alter the heave motion in such a way that the higher order harmonics in $\arctan(\omega\cos(\omega t))$ are cancelled, and therefore do not cause the multi-peaked profiles we see as we near the terminal Strouhal Number.

To this end, we departed from a simple sinusoidal motion and added higher order terms so that the heave as a function of time became:

$$h(t) = h_0[G_1\sin(\omega t) + G_3\sin(3\omega t) + G_5\sin(5\omega t)] \tag{3.17}$$

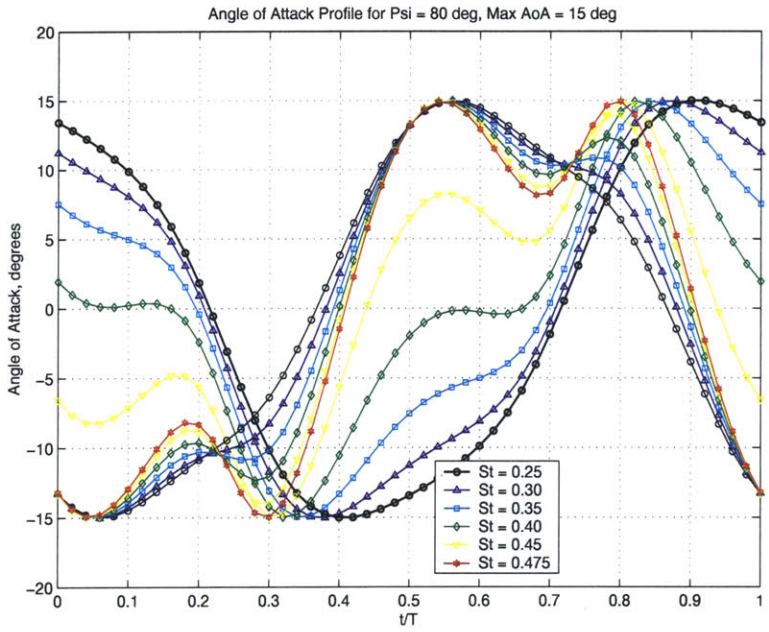

Figure 3-10: Angle of attack profiles for both thrust and drag solutions and increasing Strouhal number, parameters of Figure 3-9

and the new heave velocity is then:

$$\dot{h}(t) = h_0[\omega G_1 \cos(\omega t) + 3\omega G_3 \cos(3\omega t) + 5\omega G_5 \cos(5\omega t)] \tag{3.18}$$

where G_1, G_3, and G_5 are coefficients found in Table 3.1. θ_0 can be found using an iterative solver, just as before.

Strouhal Number	G1	G3	G5
0.32	1.00000	0.02152	0.00063
0.36	1.00000	0.02553	0.00084
0.40	1.00000	0.02946	0.00107
0.44	1.00000	0.03326	0.00130
0.48	1.00000	0.03691	0.00154
0.52	1.00000	0.04039	0.00107
0.56	1.00000	0.04370	0.00201
0.60	1.00000	0.04684	0.00224

Table 3.1: Coefficients for heave fix

In Figures 3-11 and 3-12 we show the effect of this higher order heave motion.

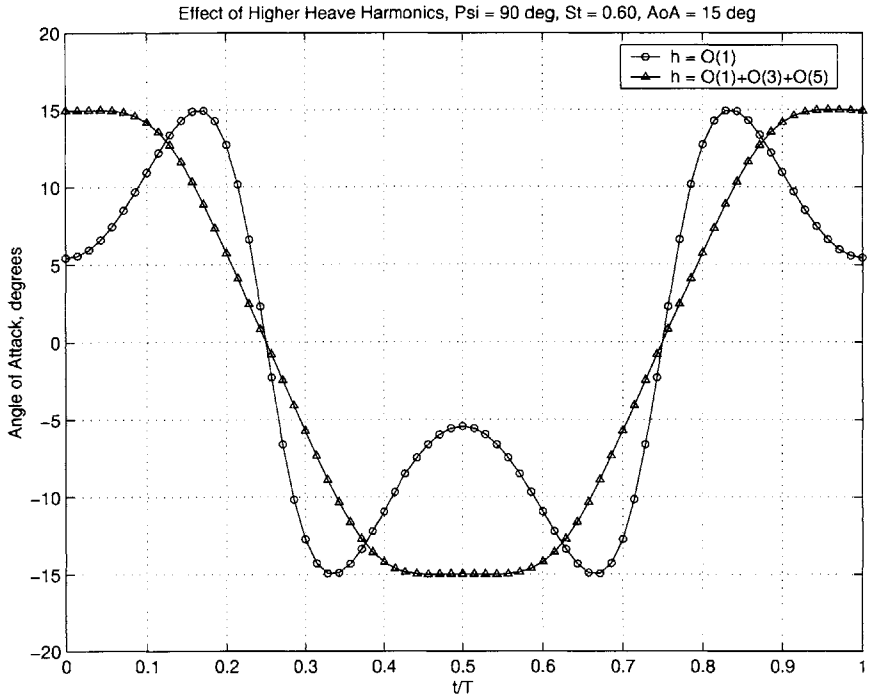

Figure 3-11: Effect of higher order heave motion on angle of attack profile for $\psi = 90°$, St = 0.60, Max AoA = 15°.

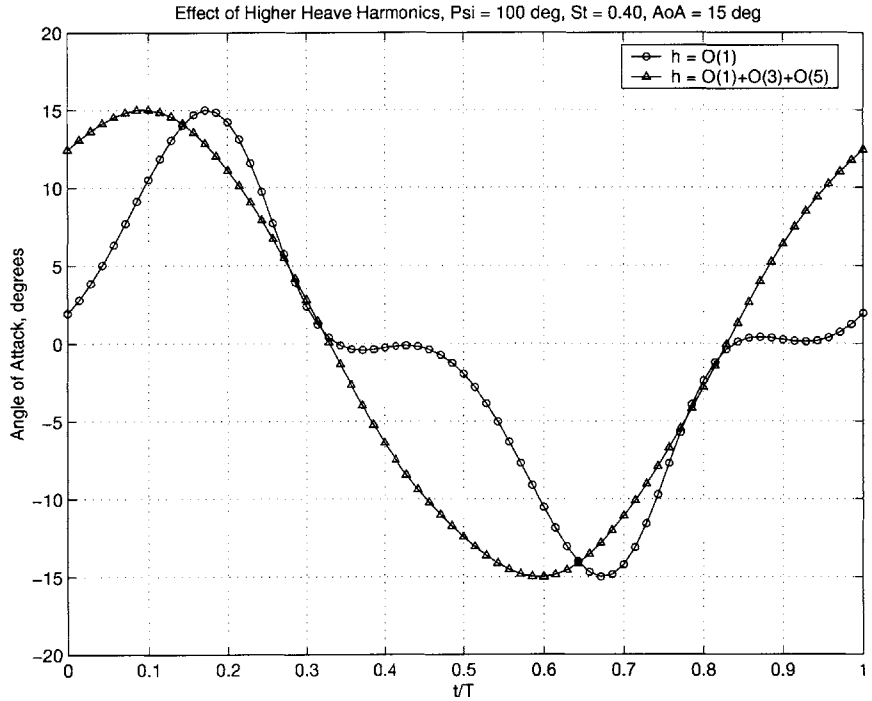

Figure 3-12: Effect of higher order heave motion on angle of attack profile for $\psi = 100°$, St = 0.40, Max AoA = 15°.

Adding the third and fifth order harmonics to the heave motion was easy in our case. The new equation for heave was simply typed into the motion control software. If mechanical means are used to create the motion, i.e. a Scotch Yoke, implementation will be more difficult. If such implementation is undertaken, it is important to note that most of the gain can be realized with only the third order harmonic.

Using this higher order heave motion, we see a large change in the angle of attack profile. Note, however, that it represents only a slight change in the heave motion. In the next chapter, we will see that this slight change can have a drastic effect on performance

Chapter 4

Propulsion Experiments

The thrust and efficiency for each run were calculated from the five data traces recorded by DASYLab. From these data, we need to find the time-averaged forces and power into the system. The average thrust force is:

$$F = \frac{1}{T}\int_0^T X(t)dt \tag{4.1}$$

and the input power per cycle is:

$$P = \frac{1}{T}\left(\int_0^T Y(t)\frac{dh}{dt}dt + \int_0^T Q(t)\frac{d\theta}{dt}dt\right) \tag{4.2}$$

The derivatives of heave and pitch position were calculated numerically using a center-difference scheme in MATLAB. The time average of each signal or product of signals was not calculated over one period, but over the maximum number of steady cycles for a given run.

The towing speed, U, was 0.40 m/s for all runs. This speed corresponds to a Reynolds number of approximately 40,000 (based on foil chord). Recalling the geometry of the foil, we now have all the necessary information to find the thrust coefficient and propulsive efficiency. The thrust coefficient is:

$$c_T = \frac{F}{\frac{1}{2}\rho c s U^2} \tag{4.3}$$

where ρ is the fluid density, c is the foil chord, and s is the foil span. Similarly, the power coefficient is:

$$c_P = \frac{P}{\frac{1}{2}\rho c s U^3} \tag{4.4}$$

where P is the power in, defined in Equation 4.2. The propulsive efficiency is simply the power out divided by the power in, or:

$$\eta_P = \frac{FU}{P} \tag{4.5}$$

Note that the thrust coefficient could also be defined by the swept area of the trailing edge instead of the projected planform of the foil. The maximum excursion of the trailing edge is a function of the heave amplitude, pitch amplitude, phase angle, and pitch axis location along the chord of the foil. Fortunately, it can be approximated by just the heave amplitude so that the peak to peak excursion of the trailing edge is simply $2h_0$. Equation 4.3 becomes:

$$c_{T_{SA}} = \frac{F}{\rho h_0 s U^2} \tag{4.6}$$

In the following figures, c_T is defined as in equation 4.3. To convert c_T to $c_{T_{SA}}$, multiply by 1/2 for $h_0/c = 1$ and by 2/3 for $h_0/c = 0.75$.

4.1 Results for Simple Harmonic Motion

In Figures 4-1 and 4-2 we show the results of experiments conducted at $h_0/c = 0.75$ and 90 degrees phase angle. Oscillations up to about 1.2 Hz were possible, giving a maximum Strouhal number of 0.44. Maximum angle of attack varies from 10 degrees to 40 degrees. Contours are calculated from experimental points taken at increments of 0.04 Strouhal Number and 5 degrees maximum angle of attack. At least two runs were conducted at each point to validate repeatability.

In Figure 4-1 we show a maximum thrust coefficient of 1.10 for both 30 and 35 degrees maximum angle of attack at a Strouhal number of 0.40.

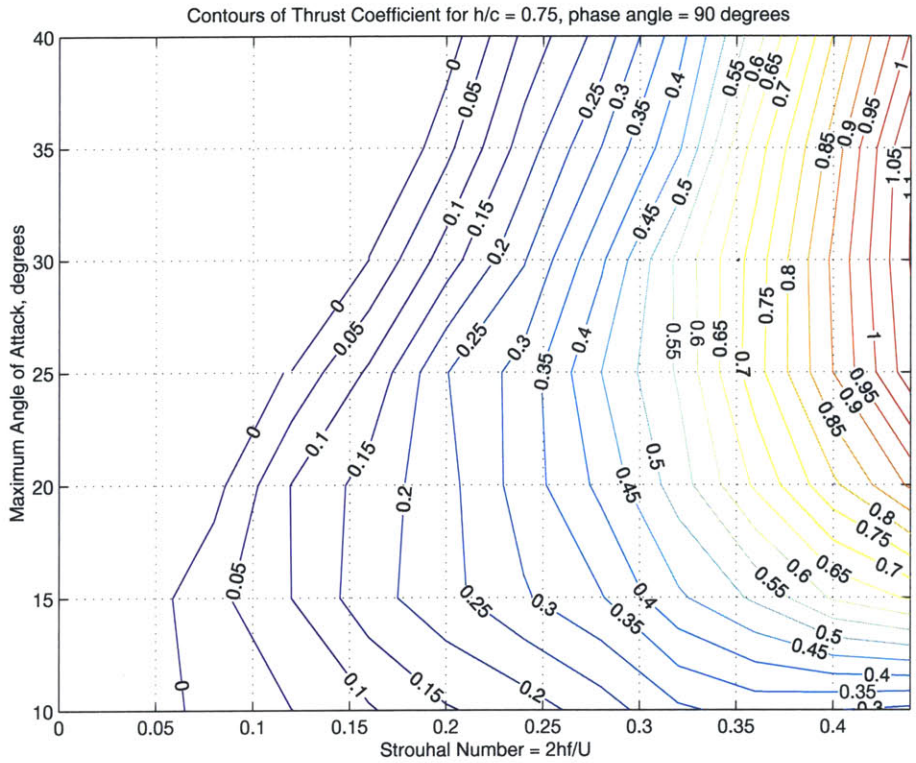

Figure 4-1: Contours of thrust coefficient for $h_0/c = 0.75$ and $\psi = 90°$

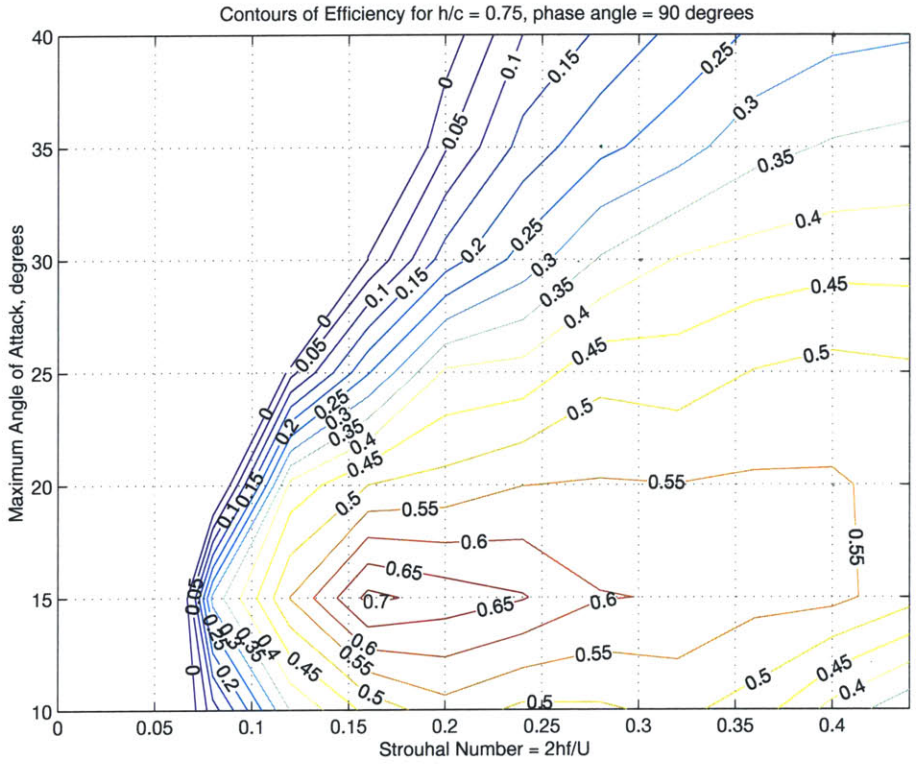

Figure 4-2: Contours of efficiency for $h_0/c = 0.75$ and $\psi = 90°$

Thrust coefficient increases with higher Strouhal Number in every case except 10 degrees maximum angle of attack. Also of special note is the transition from drag to thrust. The lowest contour in the figure is the point at which the average force in the x direction was zero. This contour represents the transition in the wake between drag and thrust producing vortex patterns. At low maximum angles of attack, this zero-crossing occurs at a low Strouhal number, around 0.06. As maximum angle of attack increases, the transition occurs at higher Strouhal numbers. At 40 degrees maximum angle of attack, transition to thrust did not occur till a Strouhal number of over 0.21 was reached.

In Figure 4-2 we show a maximum efficiency of 71.5% at 15 degrees maximum angle of attack and Strouhal number of 0.16. This efficiency peak is not significant, however, since the corresponding thrust coefficient is only 0.18. Much more significant is the 50%+ plateau of efficiency in the region of Strouhal numbers from 0.35 to 0.44 and angles of attack from 15 to 25 degrees. Referencing figure 4-1 we find 55.6% efficiency at a thrust coefficient of 0.79 for 20 degrees maximum angle of attack and Strouhal number 0.40. At 25 degrees maximum angle of attack and Strouhal number 0.44, we find 50.8% efficiency and thrust coefficient 1.08. These thrust coefficients correspond to swept area thrust coefficients of 0.53 and 0.72 respectively, and could be useful for propulsion.

Figures 4-3 and 4-4 show the results of experiments conducted at $h_0/c = 1.00$ and 90 degrees phase angle. Oscillations up to about 1.2 Hz were again possible, with higher heave amplitude giving a maximum Strouhal number of 0.60. Maximum angle of attack varies from 10 to 50 degrees. Contours are calculated from experimental points taken at increments of 0.04 Strouhal Number and 5 degrees maximum angle of attack, except at 45 degrees maximum angle of attack. No data were taken for this parameter.

In Figure 4-3 we show a maximum thrust coefficient of 2.20 at 35 degrees maximum angle of attack and Strouhal Number of 0.60. A nearly identical value of 2.17 is recorded at 30 degrees angle of attack and the same Strouhal Number. Referencing Figure 4-4, we see that the efficiencies are 36.2% and 44.2%, respectively.

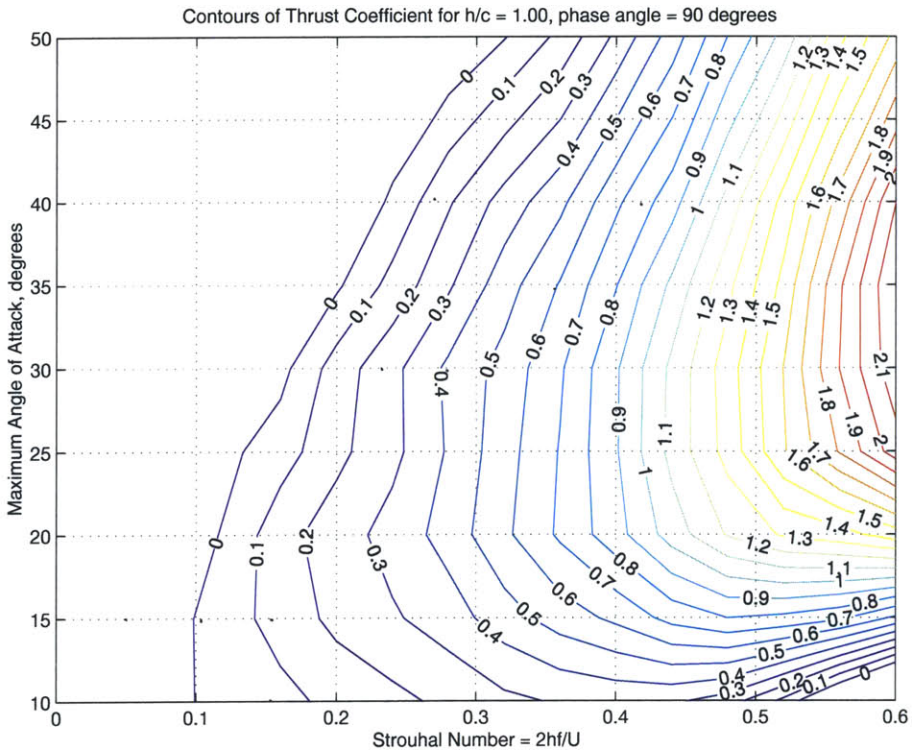

Figure 4-3: Contours of thrust coefficient for $h_0/c = 1.00$ and $\psi = 90°$

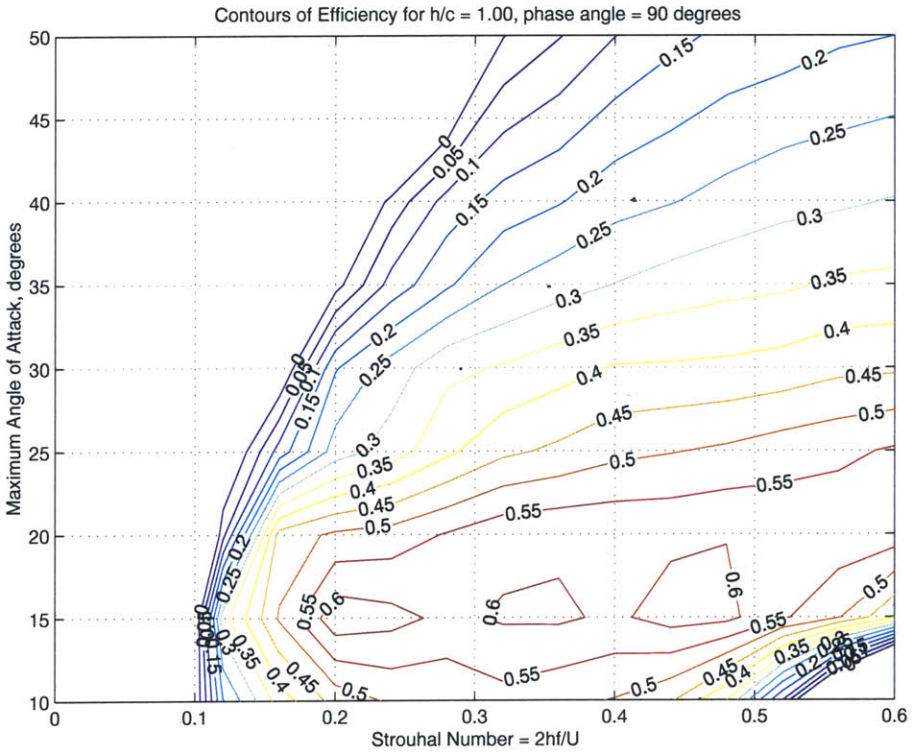

Figure 4-4: Contours of efficiency for $h_0/c = 1.00$ and $\psi = 90°$

Again note the zero-level contour of thrust coefficient. Trends are similar to those for $h_0/c = 0.75$, with the zero-crossing at lower Strouhal number for low maximum angle of attack (10 and 15 degrees) and increasing for high angles of attack. For $h_0/c = 1.00$, however, the transition starts at $St = 0.10$ for low angles of attack and increases to about $St = 0.24$ for 40 degrees angle of attack. At the highest angle of attack of 50 degrees, which we did not test for $h_0/c = 0.75$, the transition occurs at a Strouhal number of over 0.32.

Of great interest is the transition from thrust *back* to drag for high Strouhal Number and low angle of attack. We see this in Figure 4-3 for 10 degrees angle of attack and Strouhal number over about 0.54. As discussed in Chapter 3, lower angles of attack at high Strouhal Number are more susceptible to multi-peaked angle of attack profiles. In this case, the angle of attack profile has become distorted enough to cause the foil to produce drag.

In Figure 4-4 we show a peak efficiency of 63.4% at 15 degrees angle of attack and Strouhal Number of 0.20. As in the previous experiments, the corresponding thrust coefficient is low, with a value of 0.229. Again, a plateau of useful efficiency is present, in the same general parameter space as in the previous case. The contour plot also shows two other peaks at higher Strouhal numbers of about 0.35 and 0.45. These are shallow peaks, however, and can be considered part of the plateau. It can be noted that the plateau of efficiency above 55% extends to higher Strouhal Numbers for $h_0/c = 1$.

The useful efficiency plateau for $h_0/c = 1.00$ occurs between about 15 and 25 degrees maximum angle of attack and Strouhal number from 0.30 to 0.60. At 25 degrees angle of attack and Strouhal Number 0.60, we find an efficiency of 55.6% and thrust coefficient of 2.05. This number translates to a swept area thrust coefficient of about 1.03. Again, these numbers reflect useful application to propulsion.

In general, some parametric combinations show promise for propulsion. Efficiency is high in some cases, but is not paired with good thrust performance. Large thrust coefficients are attainable with moderate to good efficiency, however. Both heave amplitudes show similar thrust performance, but lower mechanical frequencies allowed

us to reach higher Strouhal numbers with the higher heave amplitude. At these higher Strouhal numbers, large thrust coefficients were attained. It should be noted, though, that swept area thrust coefficients are higher for the lower heave amplitude. Finally, efficiency at low Strouhal number is better for $h_0/c = 0.75$, while efficiency at high Strouhal number (in the range of good thrust performance) is slightly better for $h_0/c = 1.00$. Time traces of the data for selected parameter sets are included in Appendix A.

4.1.1 Instantaneous Lift Vectors

The previous section shows results for time-averaged forces on the foil. These forces are functions of time, however, and vary greatly over one period of oscillation. By looking at the forces in time, we can see more clearly the mechanisms and trends in thrust discussed above. In Figures 4-5 and 4-6 we plot instantaneous force magnitude and direction with relation to heave position. We show results for two maximum angles of attack, 15 and 35 degrees, and two Strouhal numbers, 0.40 and 0.60. The foil travels left to right. All four vector plots are for $h_0/c = 1$.

In Figure 4-5 we see results for a moderate Strouhal number of 0.40 and both maximum angles of attack. For 15 degrees angle of attack we see the instantaneous force vectors resulting in a relatively high efficiency (60%), and moderate thrust coefficient (0.62). For 35 degrees maximum angle of attack the efficiency was lower (30%), and the thrust coefficient was higher (0.80). In both cases, we can see that a large amount of mean lift is generated to produce a relatively small amount of mean thrust. In other words, most of the force created by the foil is vertical, with a relatively small horizontal component. This proportion will be discussed further in the next chapter.

The 35 degree angle of attack case has a higher thrust coefficient, but is half as efficient. We can see that the 35 degree case has much higher mean lift vectors. Since these runs were conducted at the same Strouhal number, towing speed, and heave amplitude, they have identical heave velocities as a function of time. Looking at equation 4.2 we see that the lift component of the power into the system would be

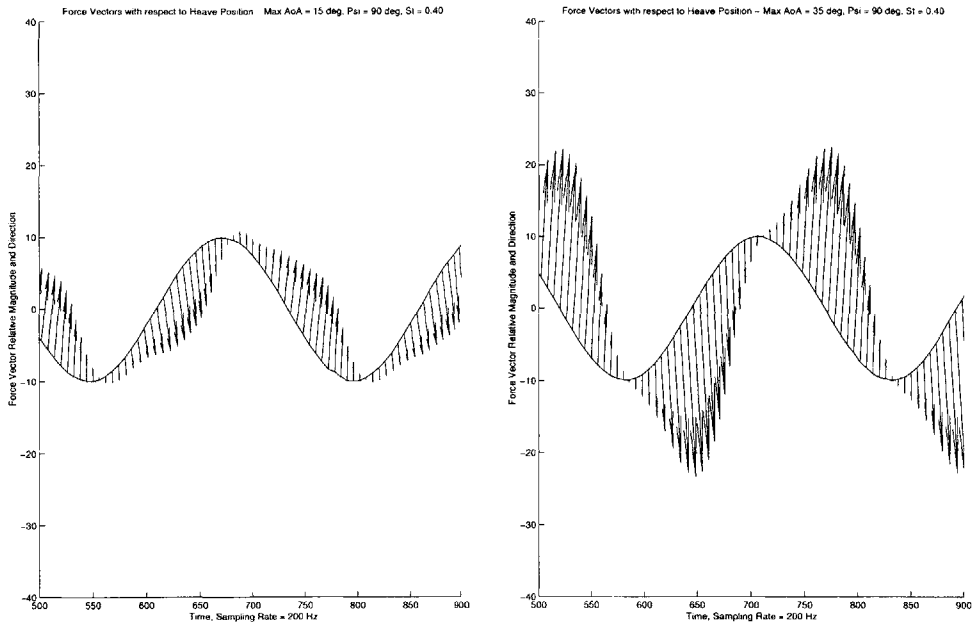

15° 35°

Figure 4-5: Thrust Vectors for $\psi = 90°$, St = 0.40

higher for the 35 degree angle of attack case. The torque component of the power is usually small compared to the lift, say 10% of the power into the system. Even though 35 degrees angle of attack produces about 30% more thrust than 15 degrees, the power into the system is around 2.5 times higher, resulting in half the efficiency.

In both the 15 and 35 degree cases we also note a gradual change in the magnitude of the force vectors as the foil passes though the maximum heave position between an upstroke or downstroke. At higher Strouhal numbers we will see that the transition can be quite abrupt. In the case of an experiment near terminal Strouhal number, the transition can even take place at a completely different location in the heave cycle.

In Figure 4-6 we again show instantaneous force vectors for 15 and 35 degrees maximum angle of attack, but at a higher Strouhal number of 0.60. For 15 degrees maximum angle of attack, the thrust coefficient was 0.58 and the efficiency was 40%. Both thrust and efficiency curves are dropping off at this point, and it is probable that thrust transitions back to drag at a higher Strouhal number. As we can see from the force vectors, these parameters exhibit a deformed angle of attack profile. The maximum forces occur where the heave velocity is zero and the minimum forces

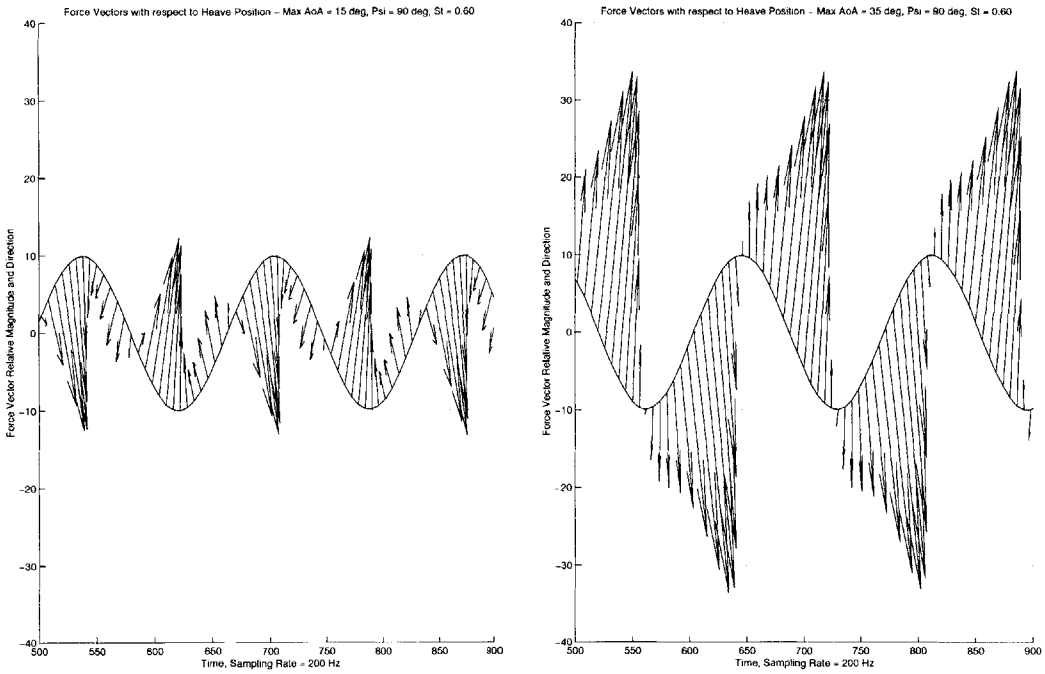

15° 35°

Figure 4-6: Thrust Vectors for $\psi = 90°$, St = 0.60

occur where the heave velocity is maximum. This plot thus shows what happens to the instantaneous force vectors as a parameter set approaches terminal Strouhal number.

For the 35 degree maximum angle of attack case at 0.60 Strouhal number, we see the instantaneous force vectors for a very high thrust parameter set. The thrust coefficient for this case was 2.20 and the efficiency was 36%. The magnitude of the force vectors is relatively large at nearly every point in the heave cycle, with a very brief period of low force magnitude at zero heave velocity. The thrust component of the force vectors is still small compared to the lift component, but the magnitude of the forces is so large that a relatively high thrust component is produced anyway. For reference, the mean of the absolute value of the Y force was about twice the magnitude of the mean X force for this run.

4.2 The Effects of Phase Angle

Up to this point, all experiments were conducted with phase angle between pitch and heave of 90 degrees, pitch leading heave. In Figures 4-7 to 4-13 we show the results of different phase angles for $h_0/c = 1.00$ and 0.75 and angles of attack from 15 to 35 degrees. Phase angles tested were 90 degrees ± 10 degrees and ± 20 degrees. The upper limit on Strouhal number for each phase angle is described in Chapter 3.

In Figure 4-7 we see the results of five phase angles for $h_0/c = 0.75$ and 15 degrees angle of attack. For these particular parameters, no benefit is gained over 90 degree phase angle. We can, however, note some trends that will persist through the data set.

First, there is a distinct decrease in thrust coefficient with increasing Strouhal number. This decrease occurs as the terminal Strouhal number is approached for the given set of parameters. As discussed in Chapter 3, a given angle of attack is not achievable above a certain Strouhal number for a given phase angle. This point, representing the convergence of drag and thrust producing θ_0 values, is the terminal Strouhal Number. Here we see the results of distortions in the thrust producing angle of attack profile as Strouhal number increases toward the terminal value.

Second, phase angles above 90 degrees are generally affected less by angle of attack distortions than those below 90 degrees. Higher phase angles will still show decreasing thrust, but this decrease will begin at a higher Strouhal number so that a higher thrust coefficient is obtained before the decline.

In Figure 4-8 we see some benefits beginning to appear for 20 degrees maximum angle of attack. First, the thrust coefficient for 100 degrees phase angle is slightly higher than that for 90 degrees up to Strouhal Number of about 0.32. The efficiency at 100 degrees is also higher in this range, with an increase of about 7% at St = 0.16. As in previous examples, this gain has little use since it occurs in combination with such a low thrust coefficient.

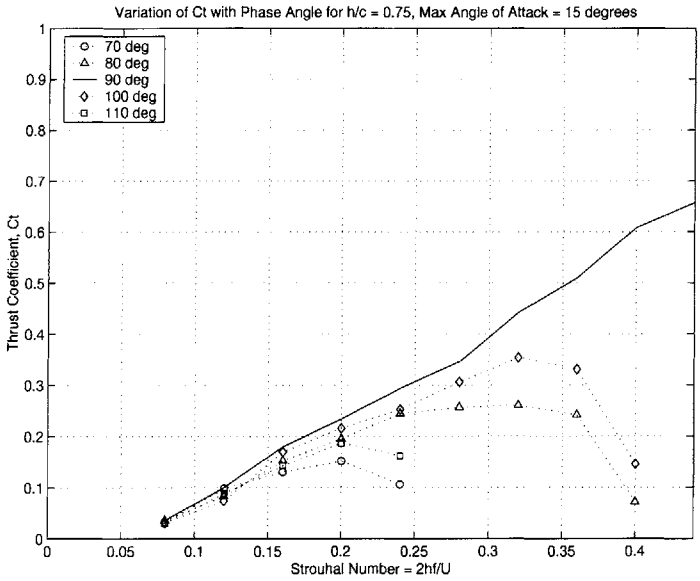

Thrust Coefficient

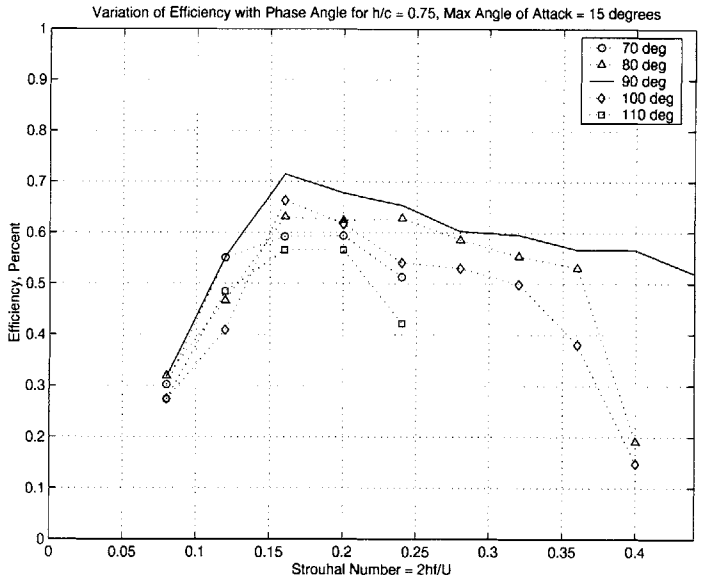

Efficiency

Figure 4-7: Effect of phase angle for Max AoA = 15°, $h_0/c = 0.75$.

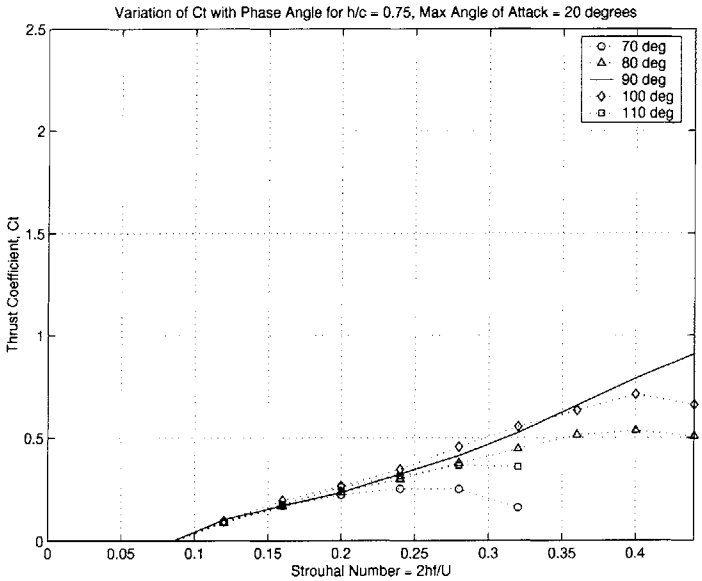

Thrust Coefficient

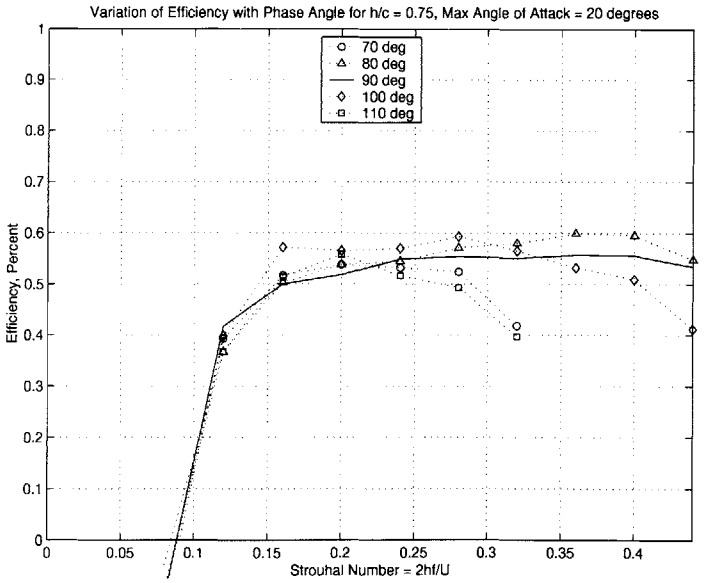

Efficiency

Figure 4-8: Effect of phase angle for Max AoA = 20°, $h_0/c = 0.75$.

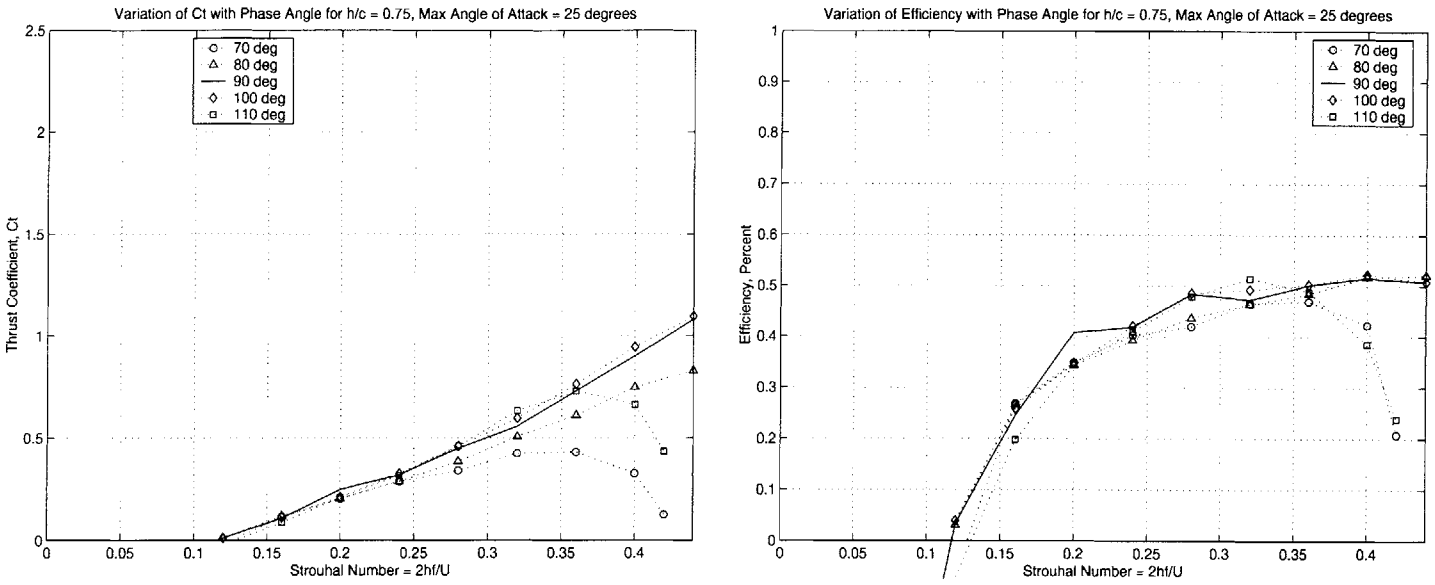

Thrust Coefficient Efficiency

Figure 4-9: Effect of phase angle for Max AoA = 25°, $h_0/c = 0.75$.

Efficiency gains also occur for 80 degrees phase angle, but these are in the range of Strouhal number from about 0.28 to 0.44, where more useful thrust is available. Unfortunately, the thrust decline has started in this range and counters the efficiency increase. Note that the thrust decline is not as pronounced as maximum angle of attack increases and the terminal Strouhal number becomes larger.

In Figure 4-9 we see almost no benefit in efficiency, with only 2% to 4% gains for 100 and 110 degrees at Strouhal Number 0.32. Thrust gains for 100 degree phase angle are in a higher range for these parameters, from Strouhal number 0.28 to 0.44. Also of interest is the fact that the highest thrust coefficient for Strouhal Number 0.32 is achieved at 110 degrees phase angle.

In the higher heave amplitude runs we see similar trends, but are able to investigate higher Strouhal numbers. In Figure 4-10 we show a large efficiency gain of around 11% for 70 degrees phase angle at Strouhal number of 0.16. As before, it occurs at a low Strouhal number and has a low thrust coefficient. Note the shallow triple-peaked shape of the efficiency curve for 90 degrees, which was noted in Section 4.1. No benefits are evident for thrust with these parameters, but we note two interesting items. First, we see thrust decrease for 90 degrees phase angle. At lower h_0/c, we

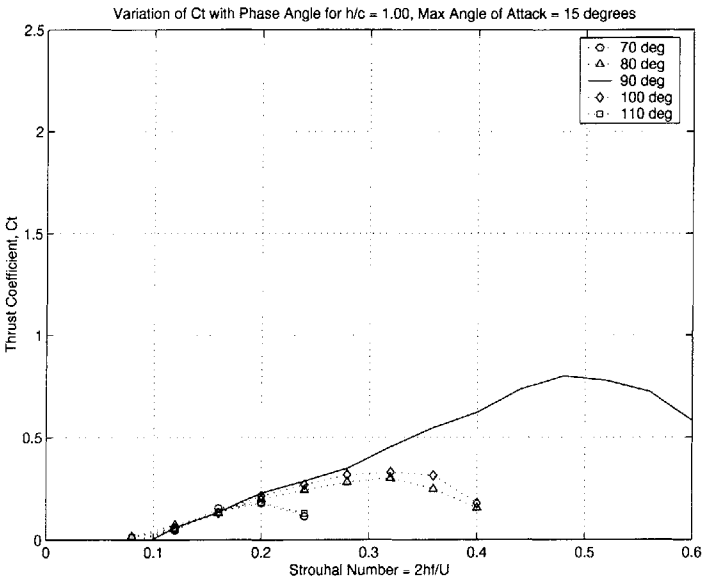

Thrust Coefficient

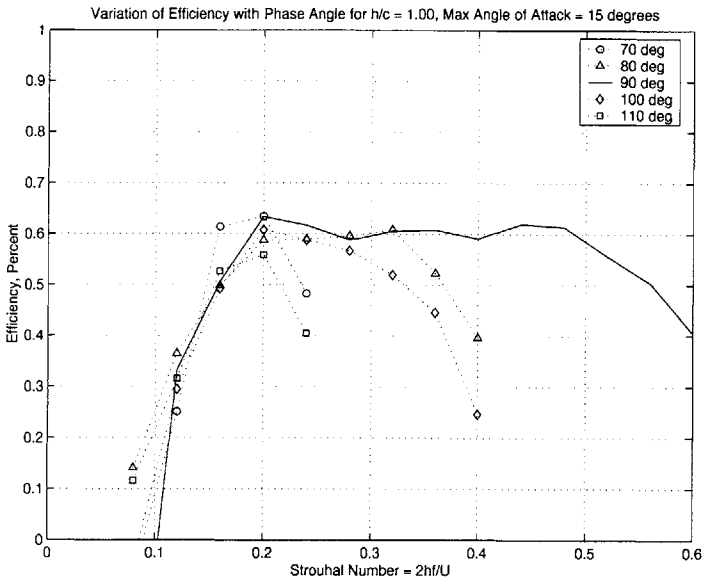

Efficiency

Figure 4-10: Effect of phase angle for Max AoA = 15°, $h_0/c = 1.00$.

could not attain a high enough Strouhal number to see this trend, since 90 degrees phase angle is the least susceptible to the decline. Second, these data show the most change in thrust zero-crossing due to phase. The change is very small, however, leading to the conclusion that phase angle has little to do with transition from thrust to drag. This trend is not unexpected, though, since phase angle has little effect on angle of attack profile at low Strouhal number.

In Figure 4-11 we see more small efficiency gains at low Strouhal Number. One efficiency gain of about 4% is attained at a higher Strouhal Number of 0.40 for 80 degrees phase angle. The thrust coefficient at that point is around 0.60, which could be useful. Note the plateau-like shape of the efficiency curve for 90 degrees phase angle. Thrust coefficients show the same trends discussed above, with no gain over 90 degrees phase angle. The higher maximum angle of attack here keeps the thrust curve for 90 degrees from declining, but we do see that the slope decreases above a Strouhal number of about 0.48.

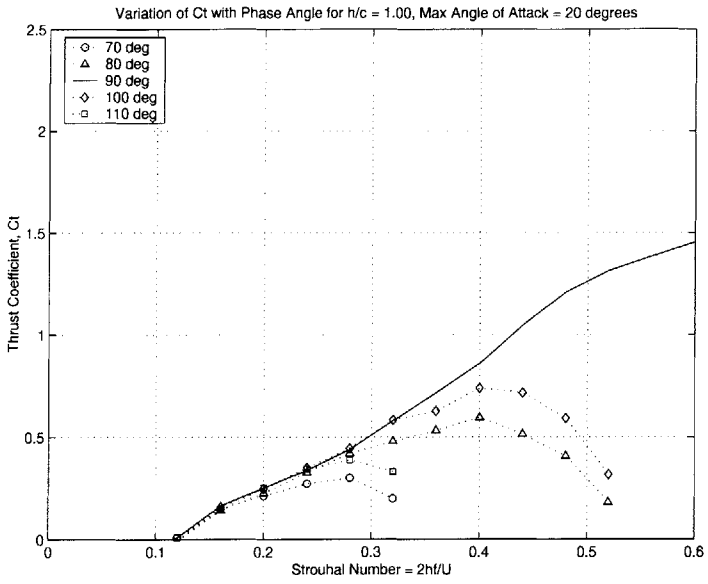

Thrust Coefficient

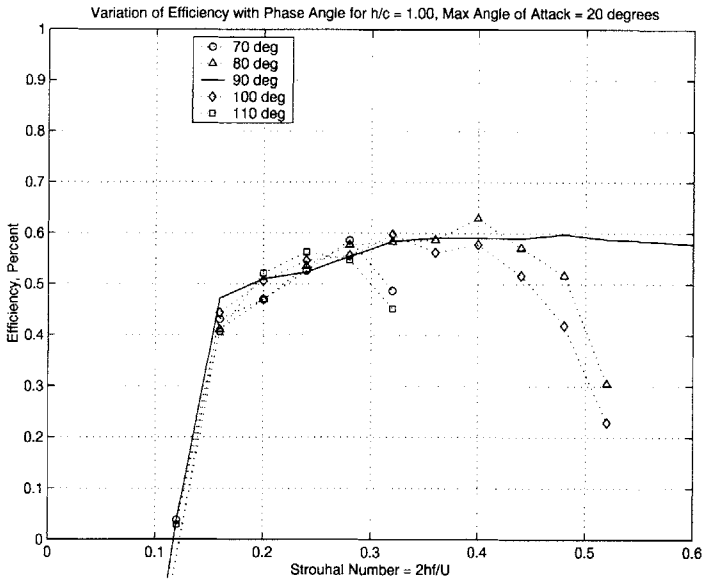

Efficiency

Figure 4-11: Effect of phase angle for Max AoA = 20°, $h_0/c = 1.00$.

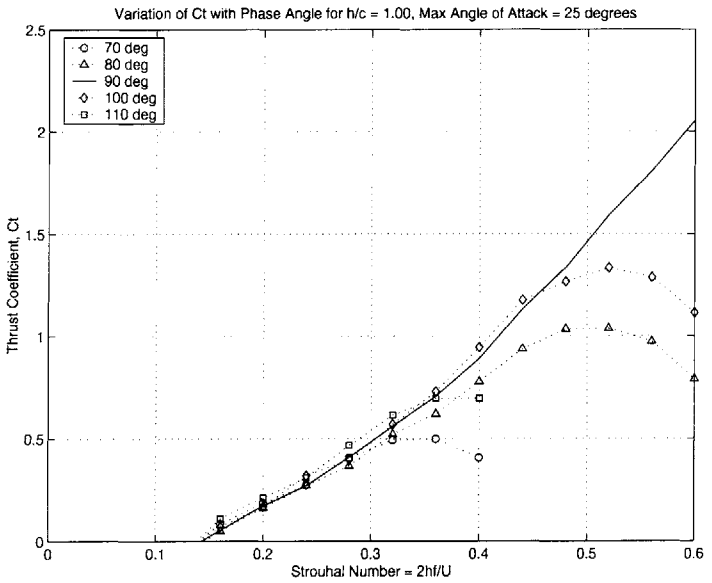

Thrust Coefficient

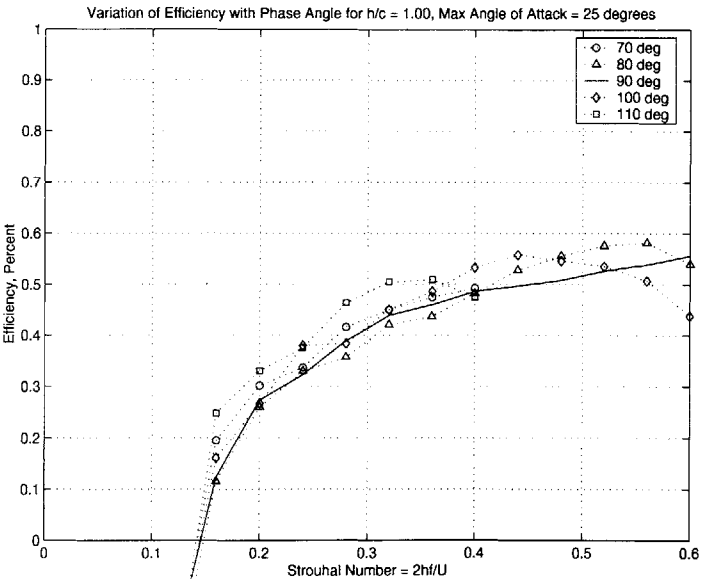

Efficiency

Figure 4-12: Effect of phase angle for Max AoA = 25°, $h_0/c = 1.00$.

In Figure 4-12 we show increases in efficiency over the entire range of Strouhal numbers tested. Peaks occur in different parts of the range for different phase angles. Between Strouhal numbers of 0.24 and 0.36, 110 degrees phase angle show the most benefit, with a maximum improvement of around 8% at Strouhal number 0.28. The highest efficiency for Strouhal numbers from 0.40 to 0.48 occurred with 100 phase angle, with a maximum improvement of about 6% at Strouhal number of 0.44. In the highest range of Strouhal numbers, from 0.48 to 0.60, 80 degrees phase angle shows improvement, with a maximum benefit of about 5% at Strouhal number of 0.52. In addition, the benefits in efficiency for 110 and 100 degrees phase angle are matched by corresponding gains in thrust coefficient. For 110 degrees phase angle at Strouhal numbers of 0.28 and 0.32, efficiency and thrust coefficient are both higher than for 90 degrees phase angle. The same is true for 100 degrees phase angle at Strouhal number of 0.40 and 0.44. Also note that the thrust curve for 90 degrees phase angle shows no sign of decline even up to a Strouhal number of 0.60. In the previous Figures, we see that 100 degrees phase angle generally provides an increase in thrust coefficient up to a certain Strouhal number. We can also note that the benefit extends to a higher Strouhal number as maximum angle of attack increases. For these reasons, 100 degrees phase angle experiments continued for 30 and 35 degrees maximum angle of attack at $h_0/c = 1$. Figures 4-13 show the results of these experiments.

In Figure 4-13 we see a general increase in both efficiency and thrust coefficient for 100 degrees phase angle in the range tested. For 30 degrees maximum angle of attack, the thrust coefficient is consistently higher up to a Strouhal number of 0.52, where the slope of the curve begins to decrease. At Strouhal number of 0.60, both values of thrust coefficient are about 2.16. The efficiency for 100 degrees phase angle at this point is 51.5%, a useful 6% higher than that at 90 degrees phase angle . At Strouhal number of 0.52, performance is markedly increased. The thrust coefficient here is 1.77 for 100 degrees phase angle and 1.60 for 90 degrees phase angle. Efficiency increases from 41.9% to 50.3%, an appreciable 8.4% increase.

For 35 degrees maximum angle of attack we see that thrust coefficient for 100 degrees phase angle is finally higher than that for 90 degrees phase angle all the way

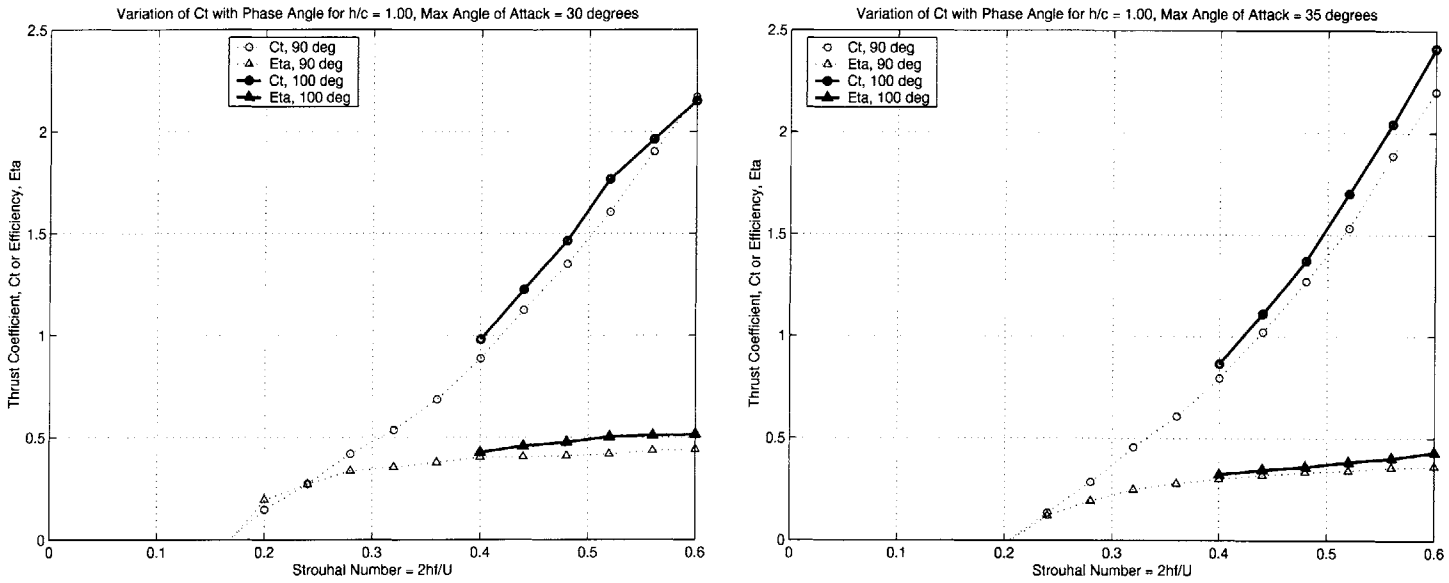

Figure 4-13: Effect of 100° phase angle for $h_0/c = 1.00$

up to a Strouhal number of 0.60. Efficiency also show a slight increase across the range. Peak performance is attained at the highest Strouhal number, 0.60, with a thrust coefficient of 2.41 and efficiency of 43.1%.

Phase angles other than 90 degrees exhibited performance benefits in some cases. Efficiency gains of 5 to 10% were recorded, but thrust performance declined markedly at higher Strouhal numbers. This decrease in thrust is due to the fact that phase angles other than 90 degrees are more susceptible to corrupted angle of attack profiles, i.e. the distortions appear at a lower Strouhal number. Thrust performance is better for 100 degrees phase angle in some cases, especially at high values of maximum angle of attack where the terminal Strouhal number is much larger than the highest Strouhal number tested.

4.3 Higher Order Heave Motion

In the previous section, we have noticed some efficiency advantages to phase angles other than 90 degrees. If these advantages occur at a relatively high Strouhal number (i.e. close to the terminal Strouhal number), they were accompanied by the declining thrust performance associated with distorted angle of attack profiles. More frequently, phase angles other than 90 degrees showed worse efficiency at high Strouhal number, mimicking the decline in thrust performance. In an effort to recover this lost performance, foil kinematics were altered in such a way that the angle of attack profile retained a generally sinusoidal shape, avoiding forms with more than two peaks per cycle. Namely, the heave motion was changed to include third and fifth order terms. A more complete description of the method can be found in Section 3.5. In Figures 4-14 to 4-19 we see the results of experiments conducted with this higher order heave motion. All experiments of this type were conducted at $h_0/c = 1$.

In Figure 4-14 we show results for a maximum angle of attack of 15 degrees for both 80 and 100 degrees phase angle. At 80 degrees phase angle, we see the typical thrust result from these tests. The thrust coefficient curve for the higher order heave motion continues on at the slope of the curve for the first order motion, essentially negating the decline in thrust coefficient. In this case we see a lower initial efficiency when compared to the first order motion, with improved efficiency at the highest Strouhal number. At Strouhal number 0.40, efficiency increased from 40% to 60% and thrust coefficient increased from 0.16 to 0.43, a substantial improvement. Results for 100 degrees phase angle show a similar trend, with efficiency increasing from 25% to 51% and thrust coefficient increasing from 0.18 to 0.54 at Strouhal number of 0.40.

Since thrust decline occurred for 90 degrees phase angle at angles of attack of 20 degrees or less, higher order heave motion tests were run for these cases. In Figure 4-15 we see the results of tests at 90 degrees phase angle and 15 degrees maximum angle of attack. Substantial improvement was again realized at a Strouhal number of 0.60, as efficiency increased from 41% to 56% and thrust coefficient improved from 0.58 to 1.21.

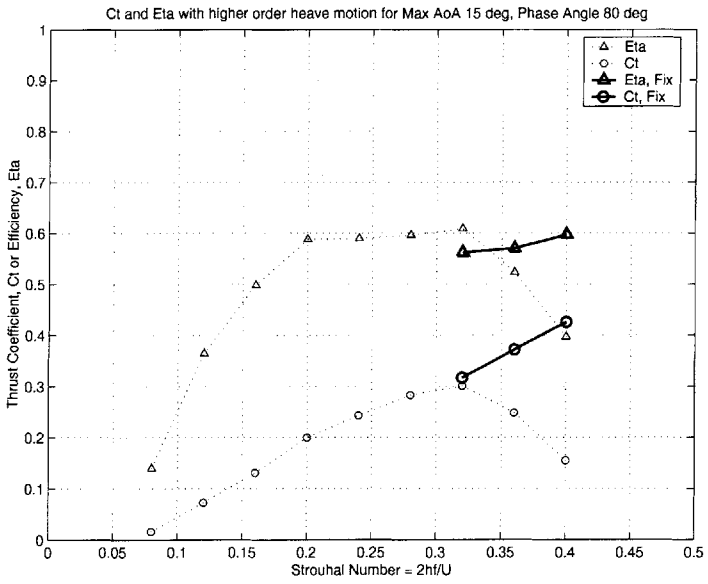

80°

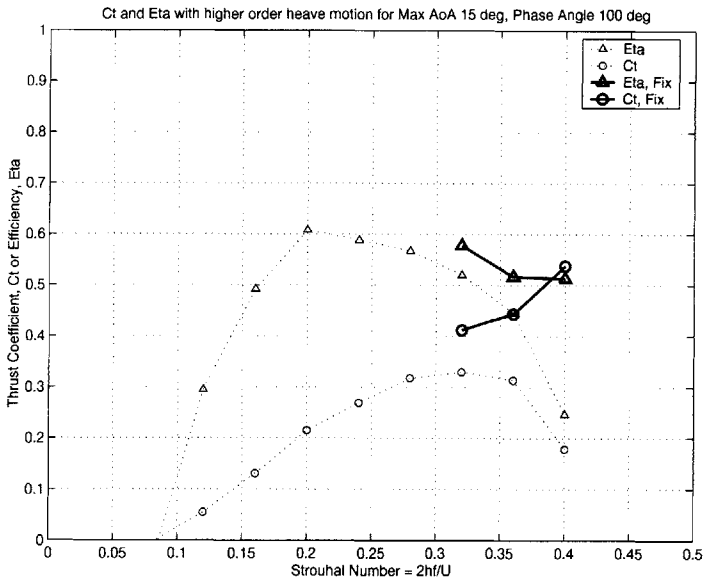

100°

Figure 4-14: Effect of higher order heave motion for Max AoA = 15°, $\psi = 80°, 100°$, $h_0/c = 1.00$

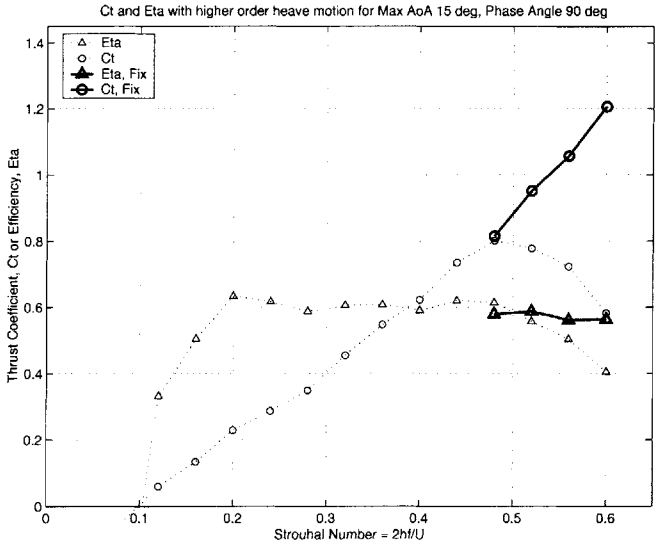

Figure 4-15: Effect of higher order heave motion for Max AoA = 15°, $\psi = 90°$, h_0/c = 1.00

Test at 80, 90, and 100 degrees phase angle were repeated for 20 degrees maximum angle of attack. The results are shown in Figures 4-16 and 4-17. For 80 degrees phase angle, we see the usual trend in thrust coefficient. The slope of the thrust curve does decrease after a Strouhal number of 0.48, indicating that the angle of attack profile may be deforming even with the higher order heave terms. Efficiency for these runs remains high at around 60%. Two points of good performance exist, at Strouhal numbers of 0.48 and 0.52. At St = 0.48, efficiency increases from 52% to 61% and thrust coefficient from 0.41 to 0.88. At St = 0.52, efficiency increases from 31% to 57% and thrust coefficient jumps from 0.18 to 0.90. Results for tests at 100 degrees phase angle show similar trends, without any decline in the thrust curve slope. The efficiency plateau is around 55% to 60%. At a Strouhal number of 0.52, efficiency increases from 23% to 55% and thrust coefficient increases from 0.32 to 1.25.

For 90 degrees phase angle we see less improvement, with little to no change in efficiency and gains in thrust only above Strouhal number 0.52. At Strouhal number 0.60, efficiency remains unchanged at 58% and thrust coefficient increases from 1.45 to 1.71.

For maximum angle of attack of 25 degrees, higher order heave motion experiments were conducted only at 80 and 100 degrees phase angle. Results are shown in Figure 4-18. Trends are the same, but performance is quite good. For 80 degrees phase angle and 0.60 Strouhal number, efficiency increases slightly from 54% to 57%. Thrust coefficient improves from 0.79 to 1.73. For 100 degrees phase angle, efficiency at a Strouhal number of 0.60 increases from 44% to 53%. Thrust coefficient improves from 1.11 to 2.09.

The last set of experiments using higher order heave motion were conducted at 30 degrees maximum angle of attack and 100 degrees phase angle. We show the results in Figure 4-19. Efficiency remains nearly unchanged, but a slight gain is realized in an already high thrust coefficient at Strouhal number 0.60. Efficiency actually decreases slightly from 51% to 49% while thrust coefficient increases from 2.15 to 2.43, the highest mean thrust recorded in this work.

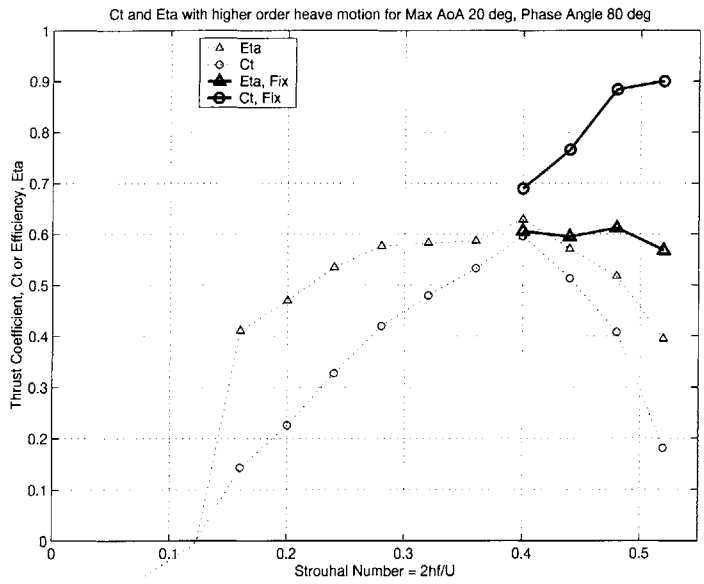

80°

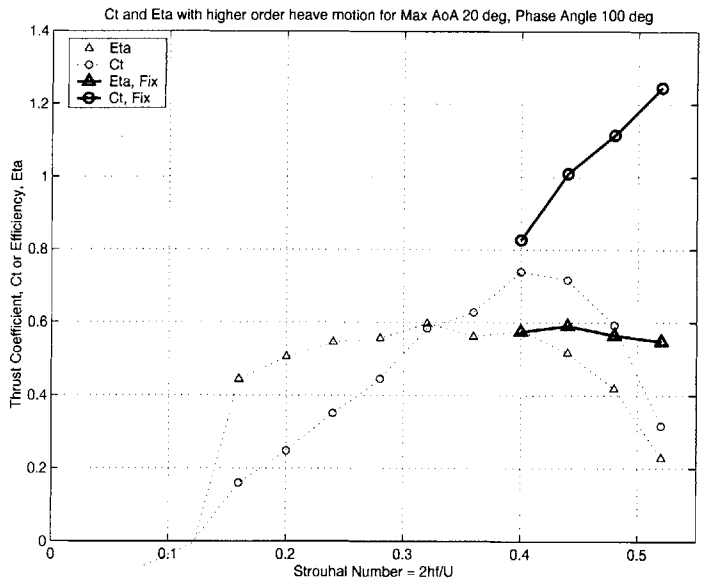

100°

Figure 4-16: Effect of higher order heave motion for Max AoA = 20°, $\psi = 80°, 100°$, $h_0/c = 1.00$

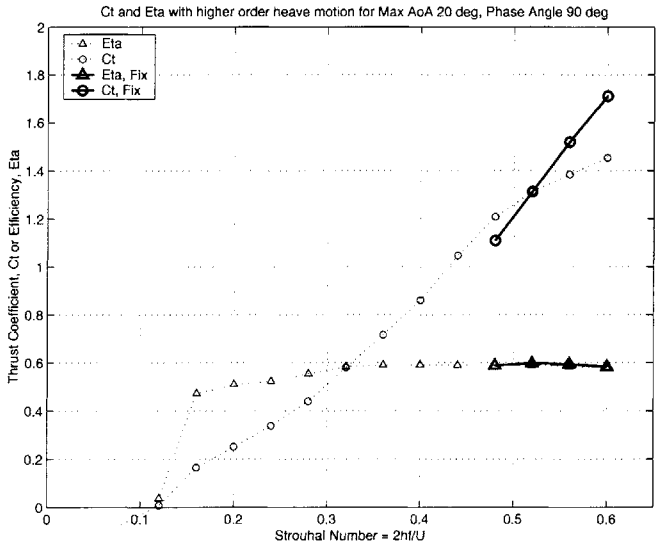

Figure 4-17: Effect of higher order heave motion for Max AoA = 20°, $\psi = 90°$, h_0/c = 1.00

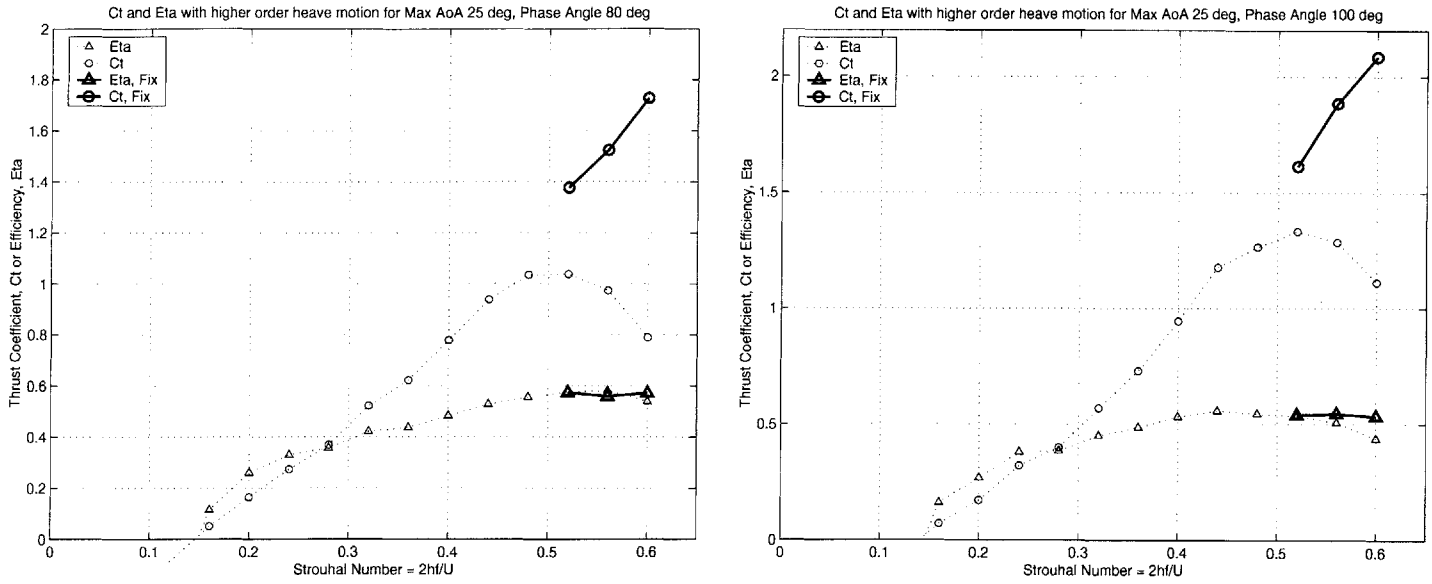

Figure 4-18: Effect of higher order heave motion for Max AoA = 25°, $\psi = 80°, 100°$, $h_0/c = 1.00$

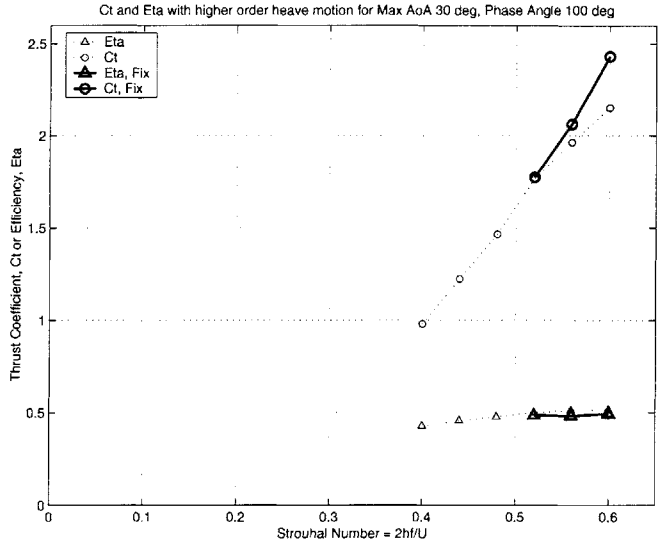

Figure 4-19: Effect of higher order heave motion for Max AoA = 30°, $\psi = 100°$, h_0/c = 1.00

Higher order heave motion experiments are quite encouraging. Small changes in the heave motion can effect drastic changes in performance by preventing corrupted angle of attack profiles. Since the distorted angle of attack profile is no longer present, the performance decline caused by phase angles other than 90 degrees is negated. As mentioned above, the highest thrust coefficient recorded in this work occurred during one of these experiments. These results suggest that controlling the angle of attack through slight modifications to foil motion should be studied further.

4.4 Braking

As discussed in Chapter 3, two solutions to the angle of attack equation usually exist. One of these solutions has an instantaneous lift vector with X component in the thrust direction, the other with X component in the drag direction. So far, we have been interested in producing thrust, and have thus used the appropriate θ_0 value. One small set of runs was conducted to examine the performance of the foil in a slowing down or braking situation. For 30 degrees maximum angle of attack, 90 degrees phase angle, and $h_0/c = 1$, the drag producing value of θ_0 was used and the results compared to thrust producing runs using the same parameters. We show the results in Figure 4-20. Unlike the thrust producing solution, which produces drag

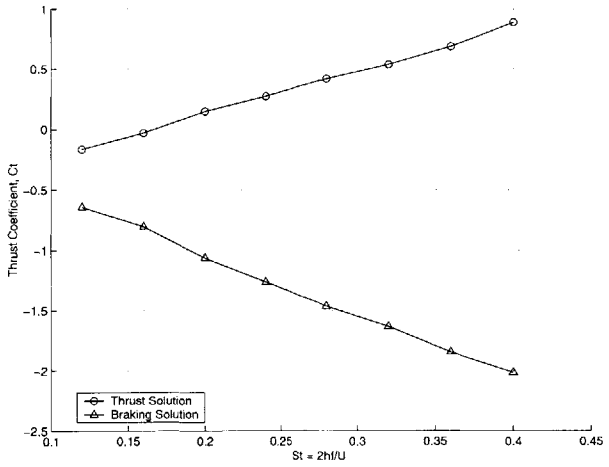

Figure 4-20: Braking

at low Strouhal number and transitions to thrust as Strouhal number increases, the drag solution produces a negative value of thrust coefficient over the entire range of Strouhal numbers tested. From these experiments, we see that the magnitude of the drag force is generally over twice as large as the magnitude of the thrust force. Braking forces are transient, of course. Unlike a steady propulsion case, the vehicle would slow down and the available force would change as soon as the initial force is applied. Keep in mind that these braking experiments, as well as maneuvering experiments in the next chapter, were conducted at a constant towing speed.

Still, changing to a reversing force simply by increasing θ_0 would be quite conve-

nient. For a marine vehicle, this type of braking force could be quite useful. Instead of reversing an engine or using a reversing gear set, the foil propelled vehicle could simply increase pitch amplitude to slow down.

Chapter 5

Oscillating Foil Maneuvering

Many animals use oscillating foils for locomotion. While the propulsive performance of these animals may be hard to measure, the maneuvering capabilities they posses can be easily observed. Even in the home aquarium, we can witness fish turning 180 degrees in less than one body length. While water jets, bow thrusters, and podded propulsion systems all provide certain levels of thrust vectoring capability, they would be hard pressed to match this kind of performance.

5.1 Maneuvering by Pitch Bias

As we noted in Chapter 4, our oscillating foil device produced instantaneous force vectors with relatively small thrust components. Thus most of the force produced by the foil was in the form of lift, but the force was symmetric and the mean lift was zero.

By adding some bias to the angle of attack, we hope to take advantage of these large lift forces for maneuvering. The simplest was to accomplish this task is to add some static offset, or bias, to the pitch angle. In the propulsion tests, the mean pitch (θ) of the foil was at zero angle of attack to the mean flow. In the maneuvering case, we tell the foil that the mean pitch position is now at some non-zero angle of attack to the mean flow. The foil then oscillates about this new mean pitch, effectively biasing the angle of attack by that many degrees and in that direction. For example,

a foil under certain parameters oscillates so that it has 15 degrees maximum angle of attack. In this case, the foil would experience ± 15 degrees angle of attack. If we added a 5 degree positive bias to the foil, it would pitch up 5 degrees for its initial position and see that position as zero. Once oscillations began, the foil would see +10 degrees and -20 degrees angle of attack.

Experiments were conducted in the parameter space of good thrust producing runs from the propulsion results. For 90 degrees phase angle, maximum angles of attack of 25, 30, and 35 degrees were tested. A phase angle of 100 degrees was also tested at 30 and 35 degrees maximum angle of attack since these runs produced very high thrust. All pitch biases were positive to minimize free surface effects. As a result the mean lift forces are in the up (positive) direction. For each set of parameters, the mean lift and thrust coefficient over one cycle are given. Since these forces would be transient in a real application, the maximum instantaneous lift coefficient is also recorded.

5.1.1 Results

In Figure 5-1 we show the mean thrust coefficient for 90 degrees phase angle and 25 degrees maximum angle of attack. Bias angle ranges from 0 to 30 degrees in 5 degree increments, with Strouhal number ranging from 0.32 to 0.60 in 0.04 increments. We note that adding the pitch bias always decreases the thrust coefficient and that the effects of higher Strouhal number diminish as the bias angle increases. At 30 degrees bias angle, the thrust coefficient appears to be almost independent of the Strouhal number. Also, the thrust coefficient becomes negative at around the point where the bias angle is equal to the zero bias value of maximum angle of attack. In this case the 25 degree bias angle case produces a negative thrust coefficient below a Strouhal number of 0.50, and a small positive thrust coefficient above. Finally, it is important to note that small bias angles still produce useful amounts of thrust.

In Figure 5-2 we show both mean and instantaneous lift coefficients for the parameters of Figure 5-1. We note that very large values of lift are obtained. These high numbers are not surprising, as we have noted the proportion of lift to thrust

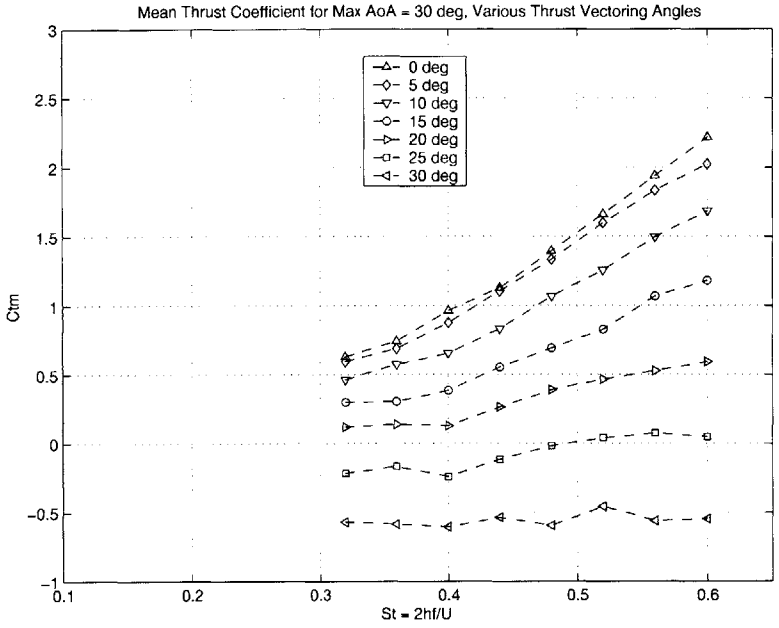

Figure 5-1: Mean Thrust Coefficient for various static pitch offsets, Max AoA = 30°

component of the forces in previous propulsion runs. To quantify this observation, Figure 5-2 shows the instantaneous lift coefficients obtained when no pitch bias was applied. Even in these cases, when the mean lift is zero, we obtain instantaneous lift coefficients of up to 6.28 at 0.60 Strouhal number.

The maximum lift coefficient obtained for these parameters was 4.231 with a maximum instantaneous lift coefficient of 12.661. In this case, as in all the pitch bias cases tested, the maximum lift values were obtained at a Strouhal number of 0.60. In general, we note that the values of mean lift are large relative to a steady flow case. The highest mean lift occurred at a pitch bias angle of 30 degrees and, as stated above, the maximum angle of attack relative to zero bias angle was also 30 degrees. For these parameters, the angle of attack over one cycle will have a minimum of 0 degrees and maximum of 60 degrees. The stall angle for a NACA 0012 foil is about 16 degrees, so we know that stall is taking place over part of each cycle. A rudder of this section would have a maximum lift coefficient of about 1.6 at 16 degrees, just before stall. Obviously, unsteady effects are allowing much higher mean lift coefficients to be obtained. In fact, these mean lift coefficients could only be obtained using multiple slat and flap wings or boundary layer control, things not often implemented into

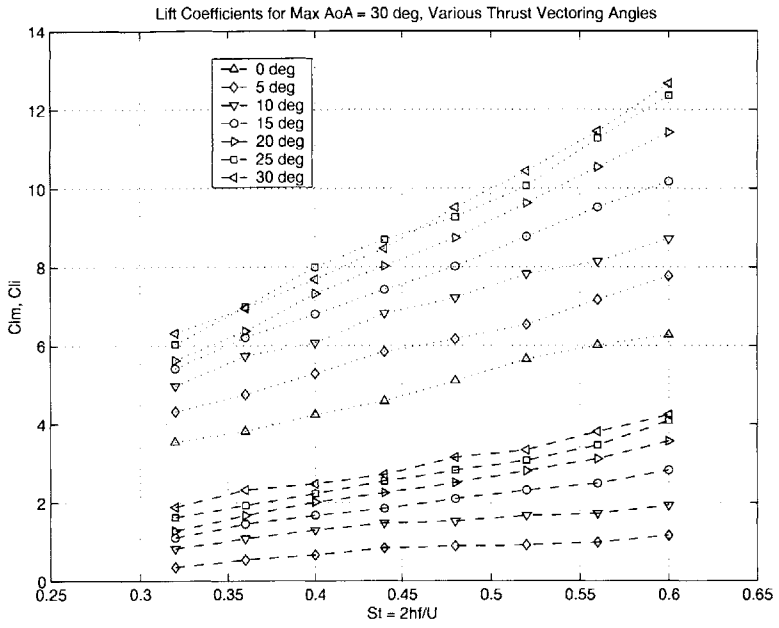

Figure 5-2: Mean and Instantaneous Lift Coefficient for various static pitch offsets, Max AoA = 30°

rudders.

In observing these and the following data, we must remember two things. First, except in the connotation of bird flight, these will be transient forces. While we towed the foil at constant speed, using the foil to maneuver a ship will result in a different ship heading and velocity. The relative flow to the foil would then change, resulting in different forces. (In birds the forces could sustain flight at a given speed, resulting in a pseudo-steady flight condition.) Second, we must remember we are merging our control surface and propulsor into one device. Comparing the forces reported here to, say, the lift to drag (L/D) ratio of a wing or rudder is difficult. The magnitude of both drag and thrust achieved here are generally much larger than the steady drag of a streamlined wing, leading to low ratios of F_Y/F_X relative to these wings. On the other hand, we can also produce a pure lift force. In this case the drag would approach zero and L/D would approach infinity.

For now we can simply state that the foil can produce relatively large forces in a wide range of directions. It may be easier to think of the total force magnitude and direction instead of its components. We will discuss this view further in the next

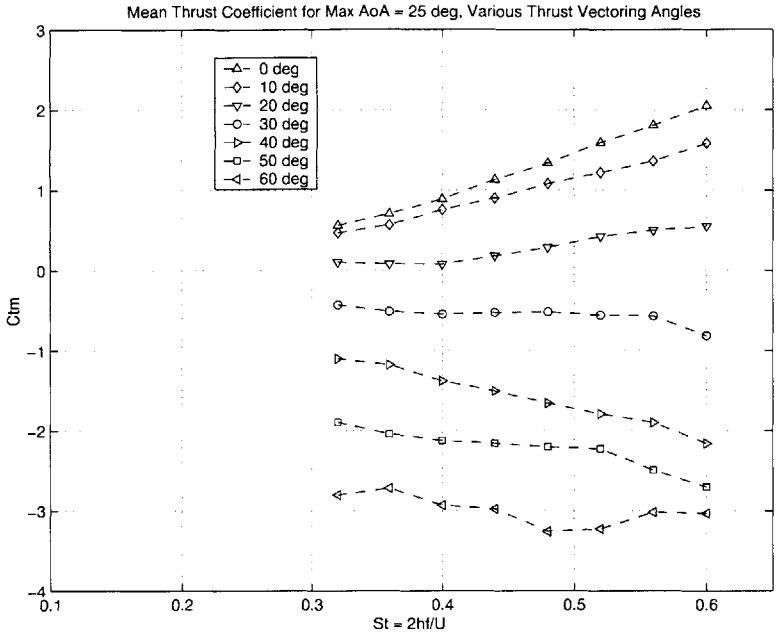

Figure 5-3: Mean Thrust Coefficient for various static pitch offsets, Max AoA = 25°

section.

In Figures 5-4 and 5-3 we again show mean thrust and mean and instantaneous lift. For these runs the maximum angle of attack was 25 degrees and phase angle was again 90 degrees. In these runs we tested the effects of very large pitch bias angles. The pitch bias was varied from 0 to 60 degrees in 10 degree increments.

The trends for these runs are similar to those in previous tests, but now we see very large negative thrust coefficients at pitch bias angles of 40, 50, and 60 degrees. Beyond 30 degrees bias, the thrust coefficient again shows dependence on Strouhal Number, becoming larger in magnitude as St increases. At 60 degrees bias angle, this dependence is more disorganized. The largest magnitude thrust coefficient appearing at a Strouhal number less than 0.60. This maximum negative thrust coefficient was -3.26 at St = 0.48.

Mean and instantaneous lift again show large values. The highest mean lift coefficient was 5.468 at 60 degrees bias and St = 0.60. The highest instantaneous lift coefficient was 16.595 at the same parameters. Comparing these runs to the previous tests at 30 degrees bias, we see that the mean lift is higher at 4.727 and the instantaneous lift is lower at 11.920. Figure 5-4 also shows an increase in the slope of the

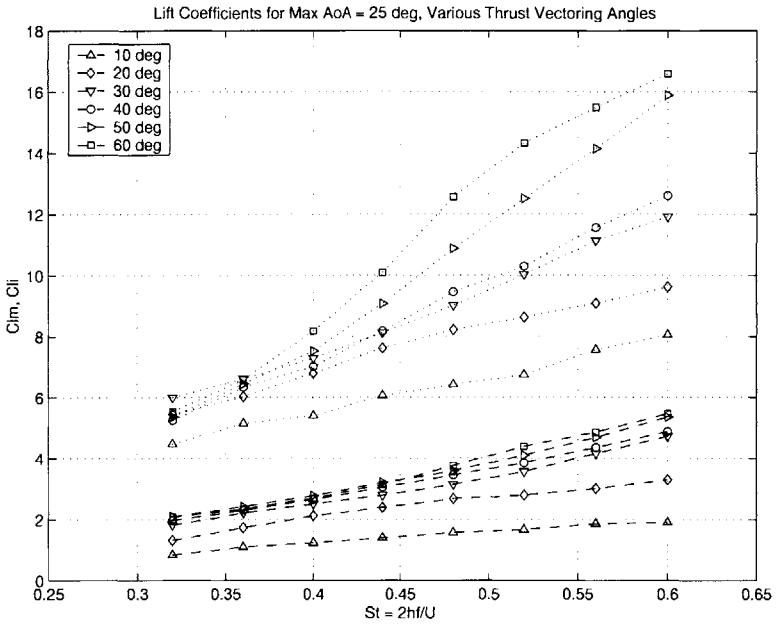

Figure 5-4: Mean and Instantaneous Lift Coefficient for various static pitch offsets, Max AoA = 25°

instantaneous lift curve above St = 0.40 for bias angles over 40 degrees. This trend is not reflected in the mean lift curve, but could still be of interest in fast braking and turning since it is accompanied by a large negative thrust. Again we must consider that the vehicle may be quickly changing direction while the carriage was not. Experiments would have to be conducted on a free body to see just how fast that body would react to these forces.

Since some of the largest forces from the propulsion tests were obtained at 30 and 35 degrees max angle of attack for 90 and 100 degrees phase angle, a few more experiments were conducted to investigate maneuvering performance for these parameters. Due to time constraints, the parameter space was reduced in size to three bias angles (10, 20, 30 degrees) and five Strouhal numbers (0.40, 0.45, 0.50, 0.55, 0.60). The results of these tests are shown in Figures 5-5 to 5-10. Table 5.1 tabulates the data for these and previous runs at 30 degrees bias and St = 0.60.

While table 5.1 shows the maximum values obtained in these experiments, it does not clearly show which parameter set provided the best performance. The problem lies in the fact that we are not comparing mean lift coefficients against a common

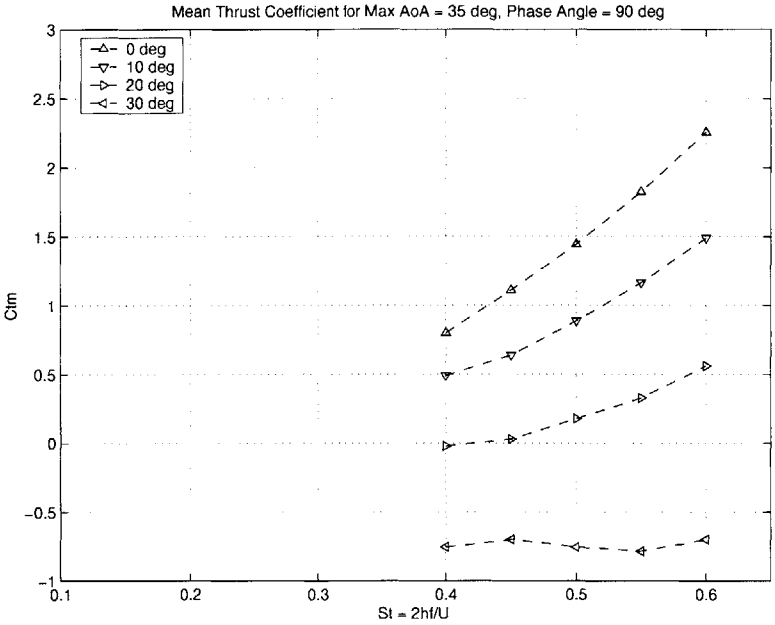

Figure 5-5: Mean Thrust Coefficient for various static pitch offsets, Max AoA = 35°

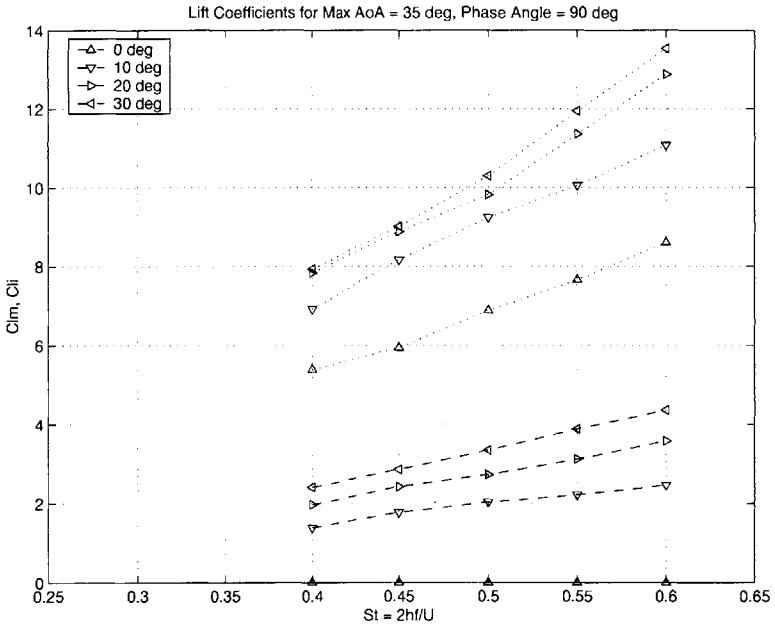

Figure 5-6: Mean and Instantaneous Lift Coefficient for various static pitch offsets, Max AoA = 35°

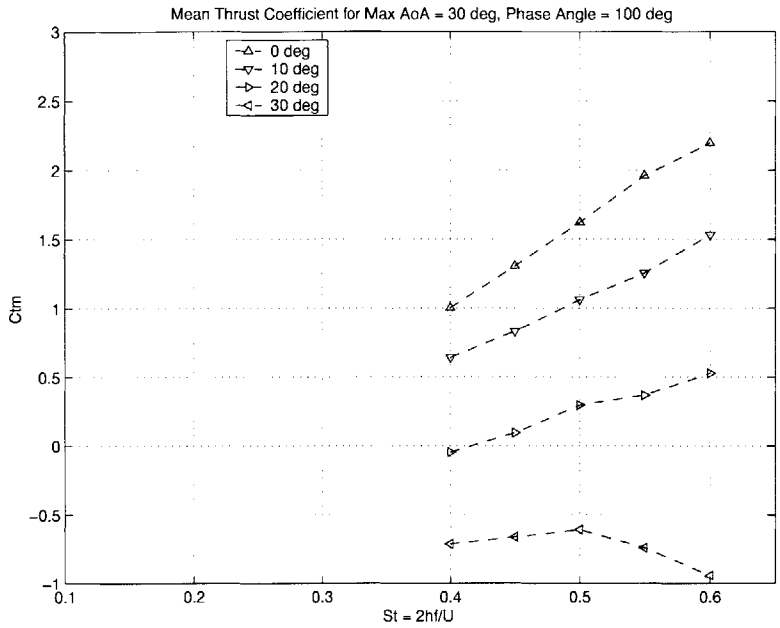

Figure 5-7: Mean Thrust Coefficient for various static pitch offsets, Max AoA = 30°, Psi = 100°

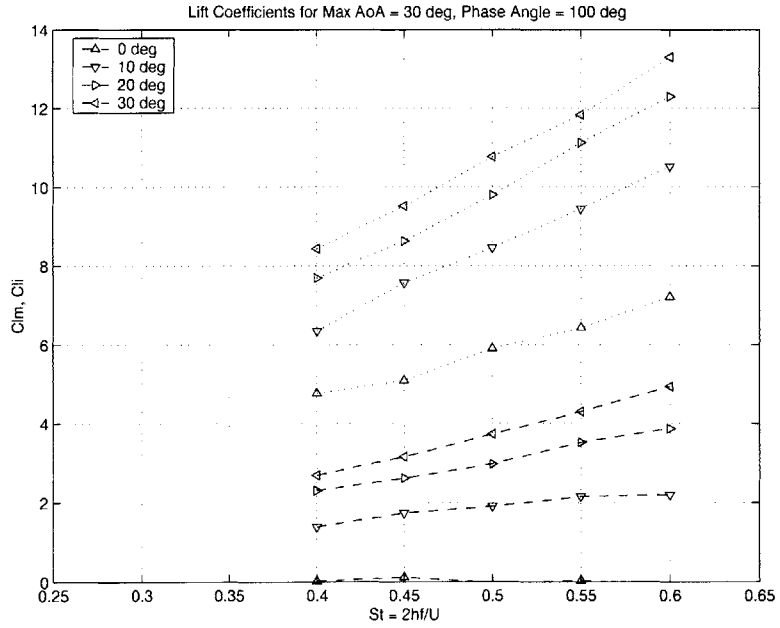

Figure 5-8: Mean and Instantaneous Lift Coefficient for various static pitch offsets, Max AoA = 30°, Psi = 100°

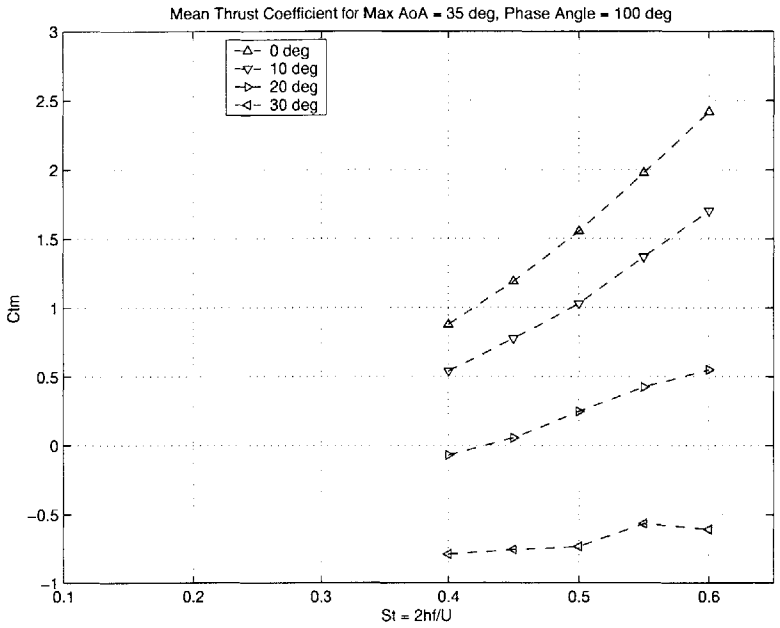

Figure 5-9: Mean Thrust Coefficient for various static pitch offsets, Max AoA = 35°, Psi = 100°

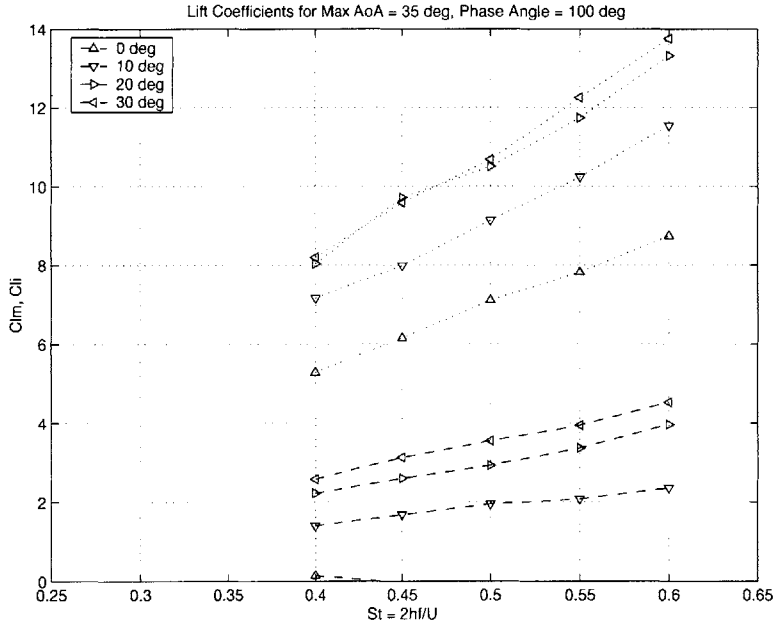

Figure 5-10: Mean and Instantaneous Lift Coefficient for various static pitch offsets, Max AoA = 35°, Psi = 100°

Phase Angle	Max AoA	Ctm	Clm	Cli
90	25	-0.817	4.727	11.920
90	30	-0.546	4.231	12.661
90	35	-0.697	4.362	13.542
100	30	-0.940	4.936	13.298
100	35	-0.609	4.525	13.755

Table 5.1: Force Coefficients for 30° pitch bias, St = 0.60

mean thrust coefficient. As mentioned above, some bias angle exists where the mean X force is zero. At St = 0.60, for example, we see the X force switches from thrust to drag somewhere between 20 and 30 degrees bias angle. In fact, this is the case for every parameter set in Table 5.1. In order to compare mean lift coefficients at zero mean thrust coefficient, a third order polynomial was fit to the these data. Using this polynomial, we first interpolated the bias angle at which zero thrust occurred for each case. A second interpolation was then used to find the mean lift at this bias angle. The results are shown in Table 5.2.

Phase Angle	Max AoA	Clm	Bias Angle
90	25	3.94	24.32
90	30	4.07	25.37
90	35	3.93	24.51
100	30	4.34	24.02
100	35	4.29	24.07

Table 5.2: Estimated pure lift coefficients and bias angles for Ctm = 0, St = 0.60

Comparing the estimated mean lift coefficients we note that 100 degrees phase angle shows slightly better performance. We also note that 30 degrees maximum angle of attack (with respect to zero bias angle) shows the highest performance in both the 90 and 100 degree phase angle cases. The estimated bias angles resulting in zero X force are quite close, even though there is a 10 degree difference in maximum angle of attack.

Pitch bias is a simple and effective way to obtain a maneuvering force from a foil

propulsion system. Due to unsteady effects, large mean and instantaneous lift forces are available. These large forces are present in the zero pitch bias propulsion cases in Chapter 4, but are balanced over one cycle of oscillation. By simply adding a bias to the foil pitch, this balance is negated and large forces are realized. Depending on the amount of bias used, thrust can be maintained while maneuvering. Conversely, a large braking force can also occur. This thrust vectoring will be discussed further in Section 5.1.2. Time traces and vector plots of selected parameter sets are presented in Appendix B.

5.1.2 Available Maneuvering Vectors

In the previous section, we showed the results of the pitch bias maneuvering tests as they were recorded from the X and Y force sensor. Since the oscillating foil is used for both propulsion and maneuvering, however, is may be better to think about the magnitude and direction of the forces produced instead of their components. We show the results of these calculations in Figures 5-11 to 5-13. In all figures, the vector at 0 degrees is the propulsion result for those parameters, with a mean lift force of zero. Vectors between 0 and 90 degrees represent parameters which provide a maneuvering force while still creating a propulsion force, while vectors over 90 degrees create a maneuvering and braking force. Imagine a ship with the bow sitting on the number 180 and the stern sitting on the center of the chart.

In Figure 5-11 we see the maneuvering vectors for 90 degrees phase angle, 30 degrees maximum angle of attack, and St = 0.48. Each vector represents a 5 degree increment in bias angle, so that we see a range from 0 to 30 degrees. The vector just slightly past 90 degrees is interesting, since it is a recorded condition of the interpolations we made in the previous section. For these parameters, the mean force on the foil was almost purely lift while towed at 0.40 m/s. This pure lift occurs at around 25 degrees bias angle, exactly in the range of the interpolated data in Table 5.2.

In Figures 5-12 and 5-13 we see the maneuvering vectors for 90 degrees phase angle and 25 degrees maximum angle of attack. Figure 5-12 shows results for St =

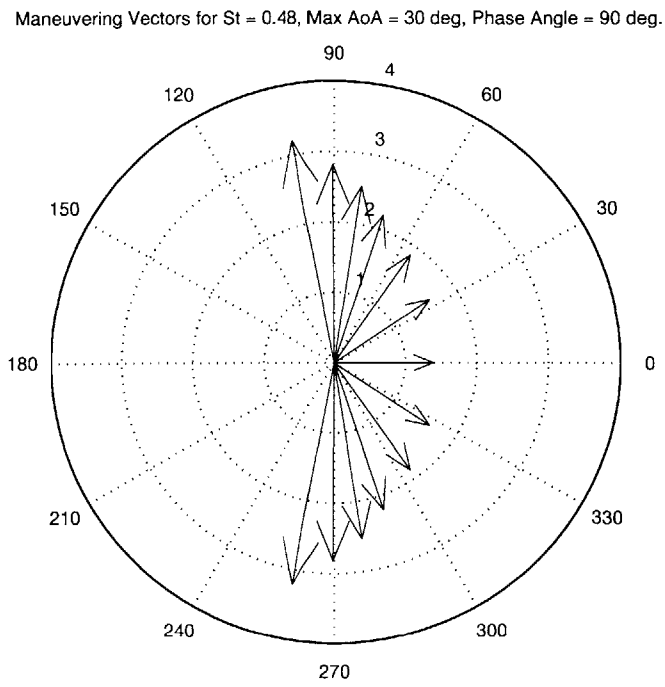

Figure 5-11: Force Vectors, St = 0.48, Max AoA = 30°, $\psi = 90°$

0.60 while Figure 5-13 shows results for St = 0.48. In this case, each vector represents a 10 degree increment in bias angle so that we see a range from 0 to 60 degrees. For these high bias angles we see large forces produced beyond 90 degrees, indicating a braking and maneuvering force. In Figure 5-12 the highest force angle achieved was about 120 degrees while Figure 5-13 shows 130 degrees force angle at the lower Strouhal number.

These compass plots show clearly the fact that the maneuvering forces are large in comparison to the available propulsion forces. For small bias angles, say 5 or 10 degrees, the forces produced occur at an angle of 30 to 60 degrees. In many cases, the thrust and lift components of these forces are each nearly as large as the thrust for zero bias angle. Forces at an angle higher than 90 degrees are larger still, and could allow a ship to slow down and change directions simultaneously and quickly.

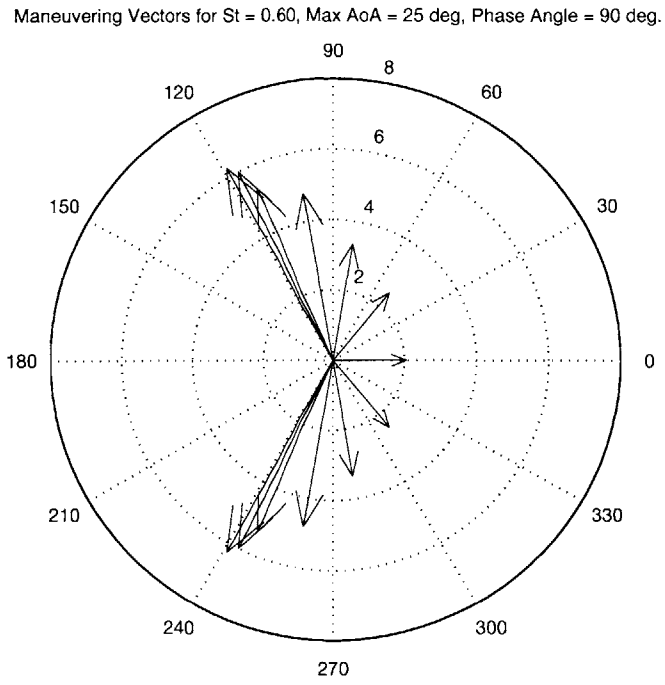

Figure 5-12: Force Vectors, St = 0.60, Max AoA = 25°, $\psi = 90°$

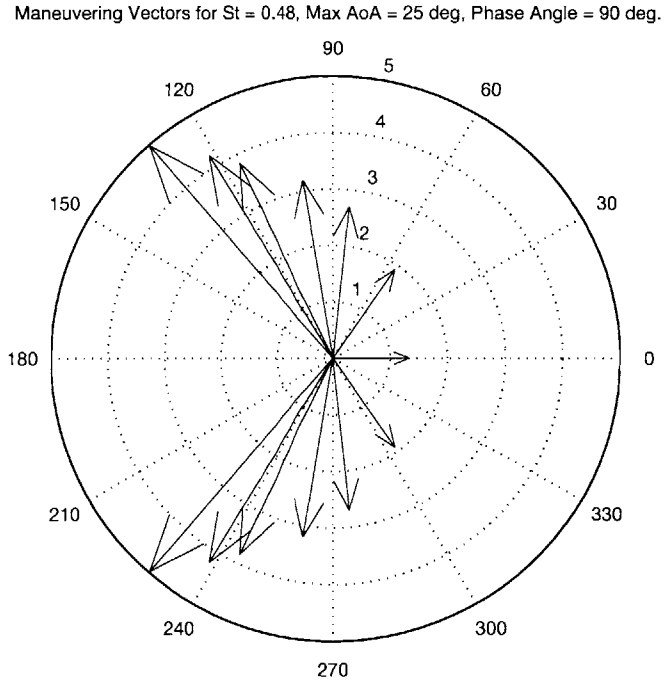

Figure 5-13: Force Vectors, St = 0.48, Max AoA = 25°, $\psi = 90°$

5.2 Starting Maneuvers

The final set of experiments consisted of starting the foil from rest. In these tests, the carriage was stationary and the foil motion consisted of only one half cycle in heave. The purpose of these tests was to begin to quantify the forces produced when a foil propelled body starts from rest.

Two methods of specifying the foil motion were used. In both methods, the foil moved one half cycle in heave, from a positive peak to a negative peak. As in previous test, h/c was set to 1 so that the total peak to peak motion was 2 chord lengths, or 20 cm. Method I, shown in Figure 5-14, specified the pitch motion so that the foil started at zero pitch and finished at 90 degrees positive pitch. The vectors in Figure 5-14 represent the foil, with the arrowheads denoting the trailing edge. Note that 90 degrees positive pitch means the trailing edge moves down.

Method II, shown in Figure 5-15, specified the pitch motion so that the foil started at 90 degrees negative pitch and finished at 90 degrees positive pitch. Note that in this case the foil is perpendicular to the mean flow at maximum heave velocity. Also note that this method is particularly easy on our control system since heave and pitch velocity are zero at the start and end of the motion.

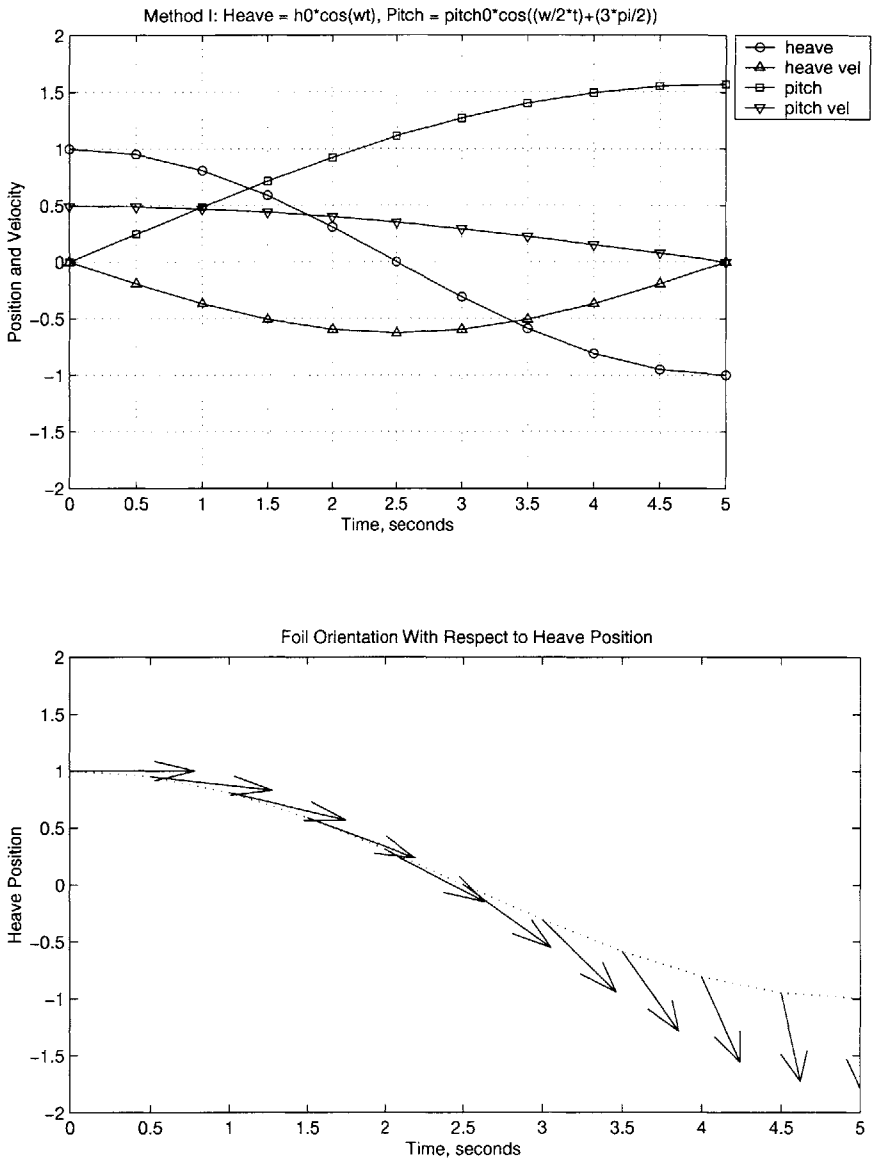

Figure 5-14: Impulse Start, Method I

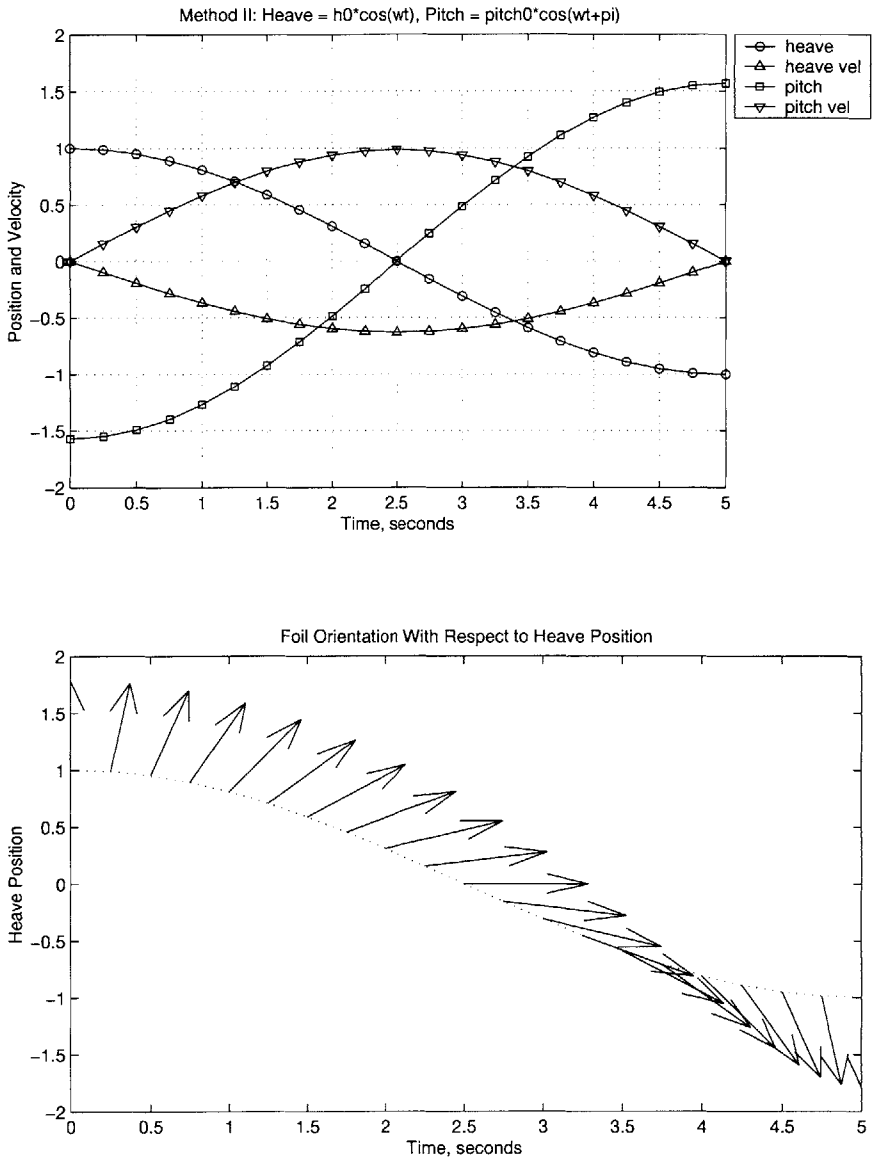

Figure 5-15: Impulse Start, Method II

5.2.1 Results

Since the carriage speed was zero for these tests, the forces could not be nondimensionalized with towing speed. Instead, the maximum heave velocity for each run was used. Forces are also plotted against maximum heave velocity since Strouhal number no longer applies. Plots of both the dimensional and non-dimensional data are shown in Figures 5-16 to 5-19.

In Figure 5-16 we show the dimensional X and Y forces on the foil at each maximum heave velocity for Method I. We see that the foil produces a large impulse force in the Y direction, which is the direction in line with the heave motion. It also produces a smaller negative force in the X direction, perpendicular to the heave motion. The maximum Y force was 72.55 Newtons at the highest maximum heave velocity, 0.754 m/s. The largest X force was -20.77 Newtons at the same heave velocity.

In Figure 5-17 we show the same data in non-dimensional form. The Y force coefficient actually decreases as maximum heave velocity increases, with a maximum value of 5.674 at a maximum heave velocity of 0.503 m/s. The X force coefficient appears to be independent of heave velocity, with a nearly constant value of about -1.0.

In Figure 5-18 we see the dimensional results for Method II. In this case the foil produces a large positive impulse force in both the X and Y directions. Forces are larger than those produced with Method I, and they again occur at the the highest maximum heave velocity. The highest Y force recorded was 138.01 Newtons and the highest X force was 92.96 Newtons.

These data were also non-dimensionalized. We show the results of those calculations in Figure 5-19. Now we see both X and Y force coefficients are almost constant when non-dimensionalized using the heave velocity. The Y force coefficient exhibits an nearly constant value of 8.0, while the X force is around 5.3. A larger range of heave velocities would have to be tested to see if non-dimensionalizing impulse force with maximum heave velocity gives a constant value of force coefficient.

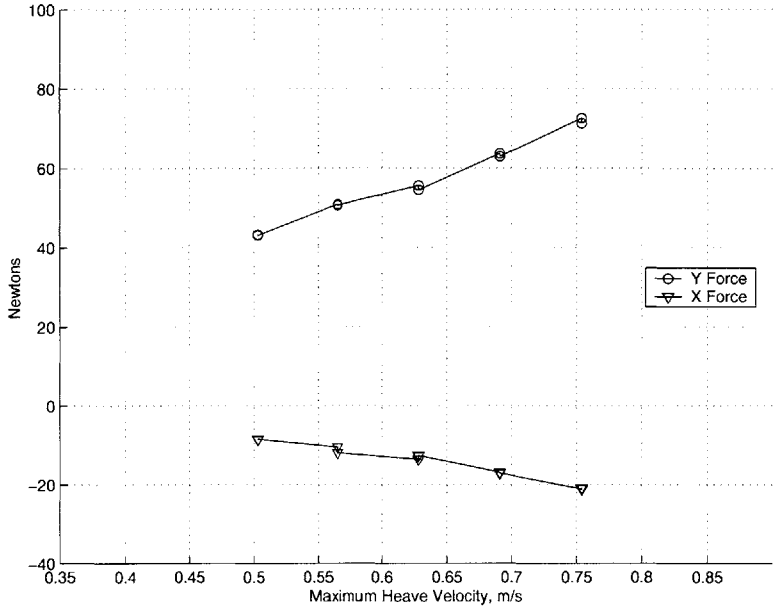

Figure 5-16: Starting Forces, Method I

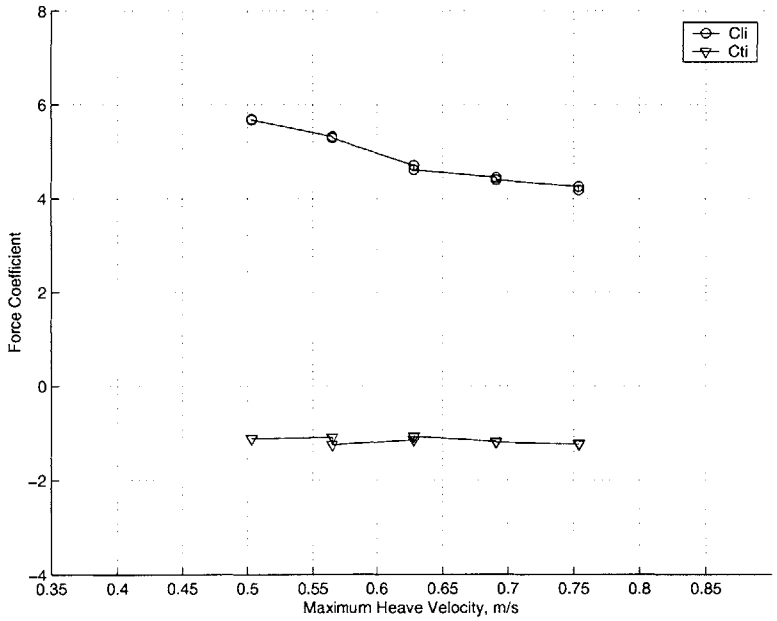

Figure 5-17: Starting Coefficient, Method I

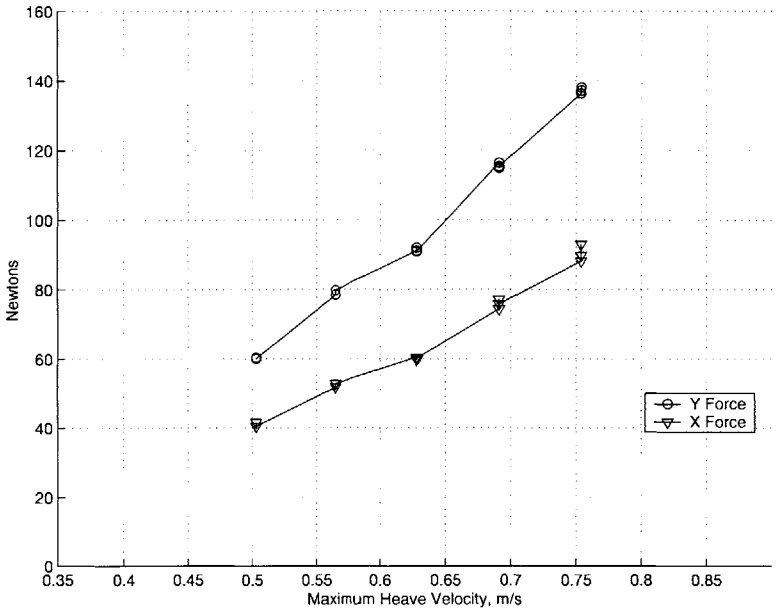

Figure 5-18: Starting Forces, Method II

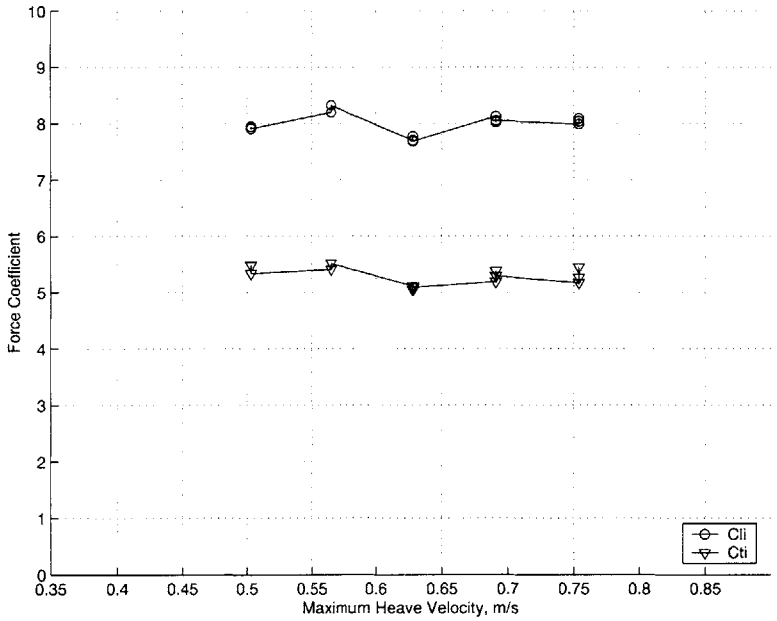

Figure 5-19: Starting Coefficient, Method II

Impulsively started foils can produce large instantaneous forces. The methods presented here are very simple analogies to a foil propelled body starting from rest. The forces involved appear to be limited only by the maximum velocity of the foil. In our experiments, Method II creates larger forces then Method I, probably because the foil is perpendicular to the flow at maximum heave velocity. Different foil motions create different instantaneous force vectors, which would allow a body to perform a variety of maneuvers from rest. Time traces of the impulse forces are presented in Appendix C.

Chapter 6

Summary

In this thesis we have investigated the propulsion and maneuvering characteristics of a heaving and pitching foil. Kinematic analysis of the problem reveals that angle of attack profile is widely varied and plays an important role in determining the thrust characteristics for a parameter set. Propulsion tests reveal good thrust producing qualities. Efficiency is lower than expected, but in some cases moderately high efficiency is paired with very high thrust. The ability of an oscillating foil to produce maneuvering forces is exceptional, showing great potential to improve the agility of rigid body vehicles.

6.1 Propulsion

The propulsive performance of our oscillating foil was good. The highest propulsive efficiency achieved was 71.5% at 15 degrees maximum angle of attack, 90 degrees phase angle, and Strouhal number of 0.16. The corresponding thrust coefficient was 0.18. Two high thrust coefficients were achieved. A planform area thrust coefficient of 2.41 (1.205 swept area thrust coefficient) occurred at 35 degrees maximum angle of attack, 100 degrees phase angle, and Strouhal number of 0.60. Corresponding efficiency was 43.2%. An even higher thrust coefficient of 2.43 (1.215 swept area thrust coefficient) occurred during one of the high order heave motion experiments. The maximum angle of attack for this run was 30 degrees, with 100 degrees phase

angle and Strouhal number 0.60. Corresponding efficiency was 49%.

Besides these maxima, we can also note efficiency plateaus in both the $h_0/c = 0.75$ and $h_0/c = 1.00$ cases. These plateaus represent large areas of the parameter space in which efficiencies reach 50 to 60%. In the high Strouhal number, high angle of attack limit of these plateaus, the thrust coefficient can also be quite high.

As noted above, one of the highest performance runs was one in which higher order heave motion was implemented. While performance was increased by using this higher order motion, it is even more important to note that these gains occurred by altering the heave motion only slightly. Since very small changes in heave motion resulted in large changes in performance, we can conclude that the problem is sensitive to heave and should be studied further.

Finally, we would like to tie the parametric study to the propulsion results. In order to accomplish this task, the angle of attack profile for 90 degrees phase angle was studied in further detail. As stated in Chapter 3, the profile can have several forms. The form of the profile is either sinusoidal, flattened, or multi-peaked. Multi peaked profiles have either four or six peaks per cycle. For angles of attack from 5 to 60 degrees, we calculated four defining points in the angle of attack profile. The results of these calculations are shown in Figure 6-1. The thin solid line is the point at which $\theta_0 = 0$. The dotted line represents the point at which the angle of attack differs from a sinusoid by 20% of the maximum angle of attack. The dash dot line represents the peak value for a flattened sinusoid, just before multiple peaks per cycle begin to appear. The dashed line is the point at which the angle of attack is zero four times per cycle, or more clearly where the heave component of angle of attack is equal to the pitch component:

$$\arctan\left(\frac{h_0\omega\cos(\omega t)}{U}\right) = \theta_0\sin(\omega t + \psi) \tag{6.1}$$

The thick solid line represents the terminal Strouhal number. For simplification, we will refer to these lines as 1, 2, 3, 4, and 5 (labeled in the Figure). All points in the parameter space to the left of line 2 have a sinusoidal angle of attack profile. Points

between lines 2 and 3 have a flattened sinusoidal profile, becoming closer to a square wave as they approach line 3. Points between line 3 and 4 have four peaks per cycle, but no more than two zero crossings. Points *on* line 4 have four peaks per cycle and four zero values. Points between lines 4 and 5 have six peaks per cycle and six zero crossings. Four of these peaks are at the maximum angle of attack and two are less. Points *on* line 5 actually reach the maximum angle of attack six times per cycle.

Data from Anderson has been included on Figure 6-1 for correlation purposes. These data are represented by letters describing the angle of attack profile. Anderson defined the angle of attack profiles as smooth sinusoid (S), smooth square wave (F), double peaked square wave (D), and triple peaked sine wave (T). These data points compare well with our calculated contours. Note that Anderson's double and triple peak descriptions refer to one half cycle of motion, and are thus four and six peaked over one whole cycle.

We can also see from Figure 6-1 that some of these calculated contours could be useful for predicting propulsion results. The line describing the point where $\theta_0 = 0$ estimates the low Strouhal number zero thrust contour fairly well. The small range of high Strouhal number zero thrust contour measured here is predicted quite will by line 3, where equation 6.1 is true. According to our data, these lines form a good estimate of the thrust producing region of the parameter space. In addition, line 2 predicts the angle of attack for maximum thrust coefficient for a given Strouhal number in the best thrust range of about St = 0.45 to 0.60.

Plotting our parametric contours with efficiency does not provide the same result, as we see in Figure 6-2. The zero contour for efficiency coincides with the one for thrust, so the boundary is the same. The highest efficiency levels occur in the range of angle of attack from 15 to 25 degrees and St = 0.20 to 0.60. This good efficiency band actually occurs in three angle of attack profile regions: sinusoidal, flattened, and quadruple peaked. This may be due to the fact that the thrust performance correlates more directly with the angle of attack profile. The efficiency is probably more closely related to the vortex wake type, which cannot be easily predicted from the angle of attack profile.

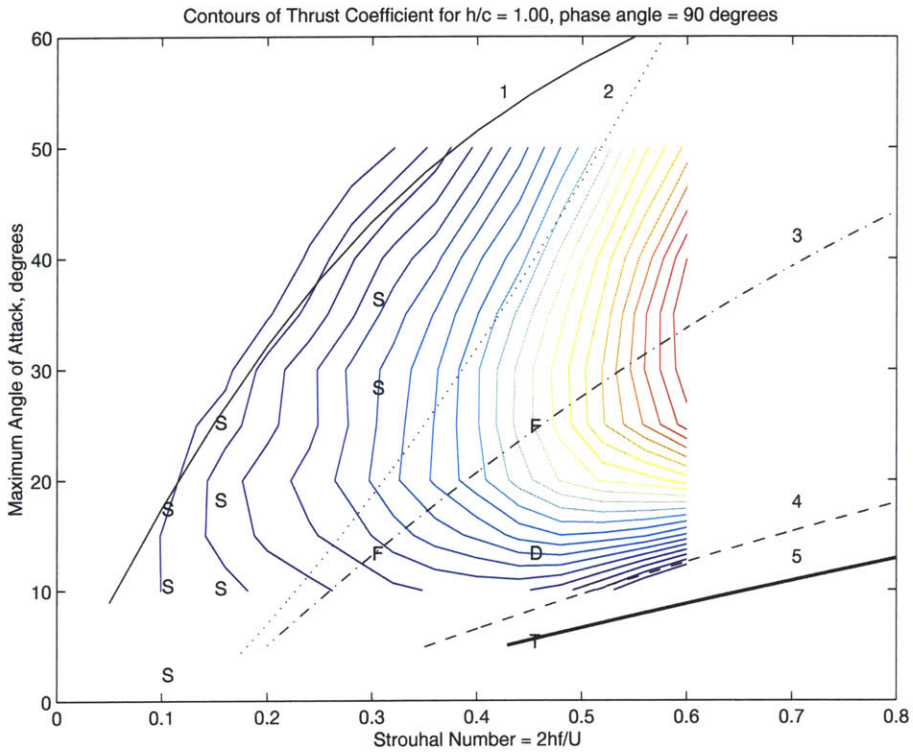

Figure 6-1: Ct compared to Anderson

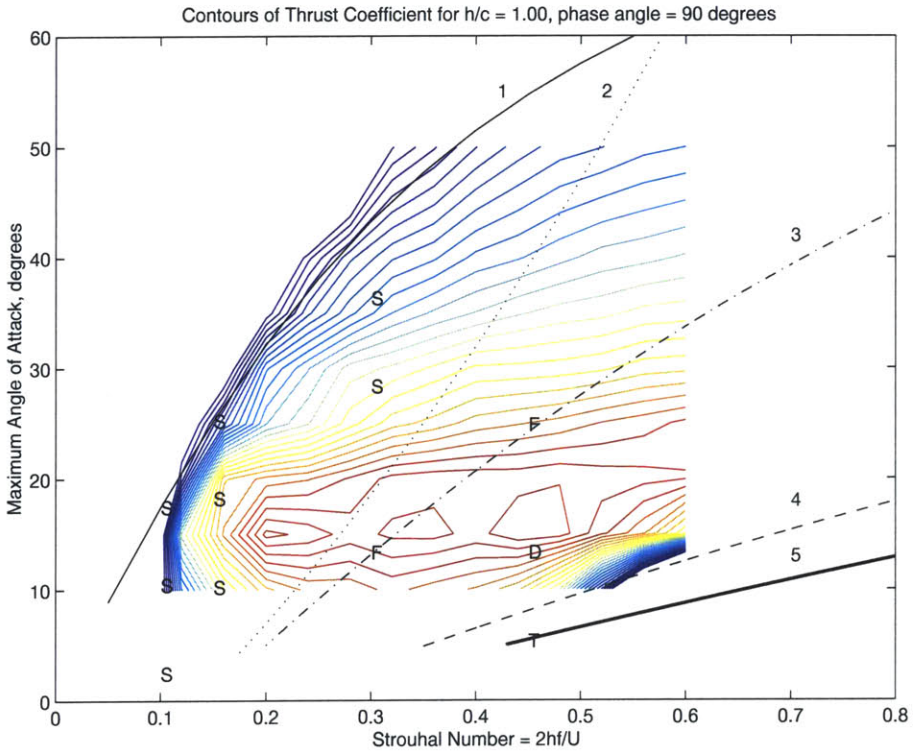

Figure 6-2: Eta compared to Anderson

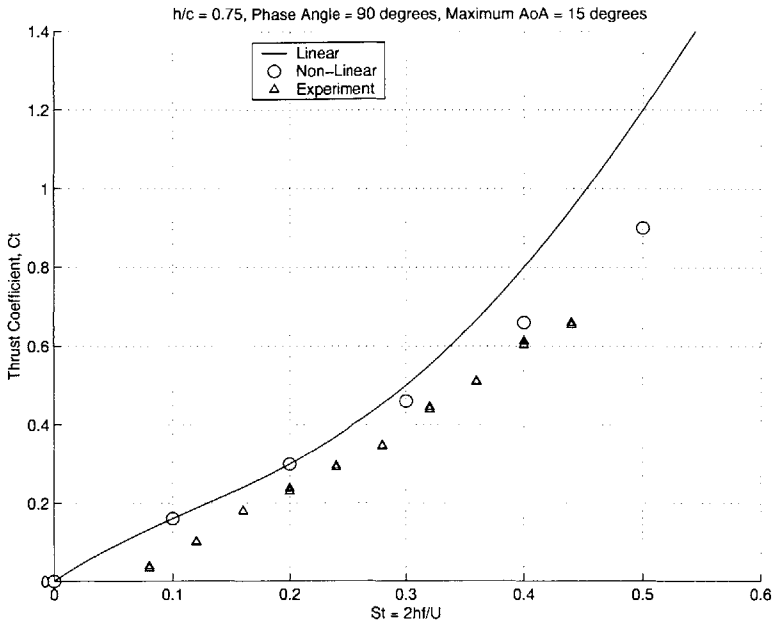

Figure 6-3: Ct compared to theory

We also compare data for one of our runs to linear and non-linear theory for the same parameters from Triantafyllou. The results of this comparison are shown in Figures 6-3 to 6-5. The thrust coefficient for our experiment is consistently less than the theoretical values. The non-linear theory matches the trend in experimental data quite well, but there is a consistent ΔCt. As mentioned previously, our thrust was measured using zero foil and carriage motion as the zero level for thrust. Thus it takes the drag on the foil into account. Using the towing speed foil drag as the zero would exclude this drag and result in an artificially high thrust coefficient. The ΔCt between experiment and theory could be due to the exclusion of foil friction drag in the theory. Looking at the power coefficient, we see that the experimental and theoretical data match quite well in the range tested. The resulting efficiency show trends similar to the thrust coefficient, with a consistent $\Delta\eta$ above St = 0.15.

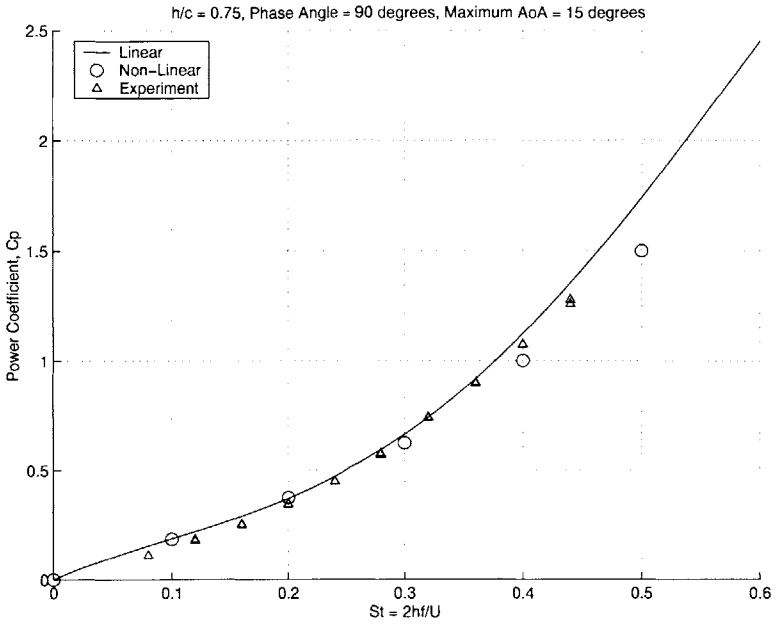

Figure 6-4: Cp compared to theory

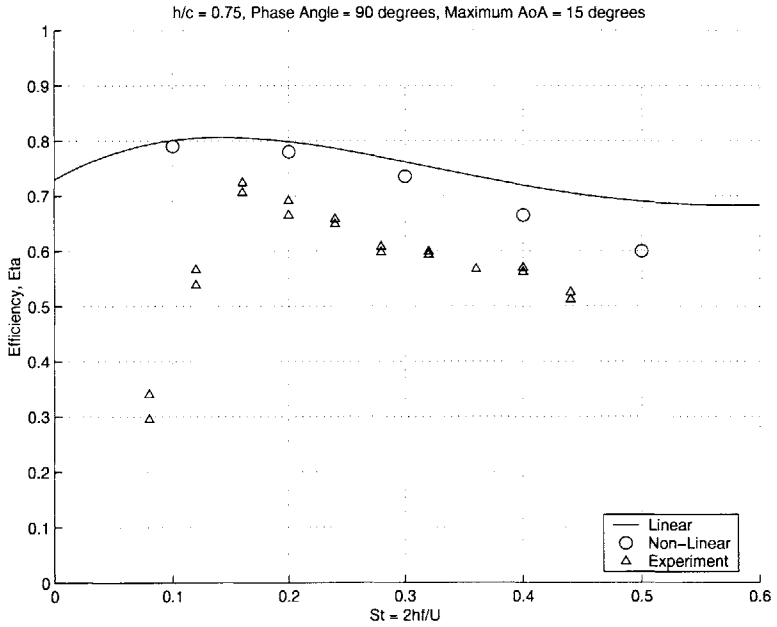

Figure 6-5: Eta compared to theory

6.2 Maneuvering

Maneuvering tests of the oscillating foil proved very promising. By simply adding pitch bias to the harmonic motion, large lift coefficients were achieved. Mean and instantaneous lift coefficients of 5.468 and 16.595 were achieved, respectively. These values were achieved for Strouhal number 0.60, pitch bias 60 degrees, and maximum angle of attack of 25 degrees relative to zero pitch bias. They were, however, accompanied by a large negative thrust force, representing a braking and maneuvering force in context of a marine vehicle. Pitch bias thus demonstrates the ability to provide a large thrust vectoring capability, from a pure propulsive force to a pure lift force (Ct = 0), to the lift and drag force present in the case above. The pure lift forces were estimated for 90 and 100 degrees phase angle and 25 to 35 degrees angle of attack. Based upon these estimates, the highest pure mean lift coefficient was 4.34 at 100 degrees phase angle and 30 degree maximum angle of attack relative to zero pitch bias. The estimated bias angle was 24.02 degrees. The bias angle for pure lift was fairly consistent for the parameters tested, varying between 24.02 to 25.37 degrees, even though zero bias maximum angle of attack varied by 10 degrees.

In general, we should note that the oscillating foil produces large lift forces. In the propulsion case, where the mean angle of attack is zero, this large lift force is cancelled over one cycle of oscillation. By adding a pitch bias, these large lift forces can be utilized effectively. In fact, our data shows that force vectors for pitch bias cases are always larger than those of propulsion cases. Pure lift forces are around twice the magnitude of propulsion forces, and for thrust vectors of 45 degrees the X and Y components can each be almost as large as X force for propulsion.

Our data also show a continually increasing lift coefficient with increasing Strouhal number, with the highest values always occurring at the highest tested Strouhal number of 0.60. Gursul and Ho estimated that the optimum reduced frequency for lift occurred around one. Their oscillating flow experiments exhibited an optimum value of about k = 0.70, where their lift coefficients showed a maxima. For our tests, the highest Strouhal number of 0.60 is equal to a reduced frequency of 0.942. It is

possible that our Strouhal number limit is near the optimum value, and that the lift coefficient will begin to decrease if higher Strouhal numbers could be tested.

The phase averaged lift coefficient (Equation 1.6) presented by Gursul and Ho was also calculated for two of our experiments. We show the results of these calculations in Figures 6-6 and 6-7. In Figure 6-6 we show the phase averaged lift coefficient for 90 degrees phase angle, Strouhal number 0.60, 30 degrees pitch bias, and 35 degrees maximum angle of attack relative to zero bias. Two periods of oscillation are shown, with heave position plotted as a dotted line for reference. We see a peak value of around 10, which occurs on the downstroke midway between the minimum and maximum heave velocity. A second, smaller peak occurs at a similar position on the upstroke. These results differ from those of Gursul and Ho, where a single maxima occurred at the minimum inlet velocity. In their work, the foil was held at a constant angle of attack while the flow velocity oscillated sinusoidally. Our problem is dynamically more complex, and shows slightly different trends. The highest phase average lift coefficient achieved, however, is very close for both cases. As mentioned in Chapter 1, Gursul and Ho achieved a phase average lift coefficient of around 14 for 20 degrees angle of attack and $k = 0.70$. As we show in Figure 6-7, our highest phase averaged lift coefficient was also close to 14. The parameters for this run were 90 degrees phase angle, Strouhal number 0.60, 60 degrees bias angle, and 25 degrees maximum angle of attack relative to zero pitch bias. In this very large pitch bias case, our data show trends more similar to those found by Gursul and Ho in that only one peak occurs per cycle. Finally, we can note that even though similar phase averaged lift coefficients were achieved, our oscillating foil produced mean lift coefficients of around twice the magnitude of those for a fixed foil in an oscillating flow.

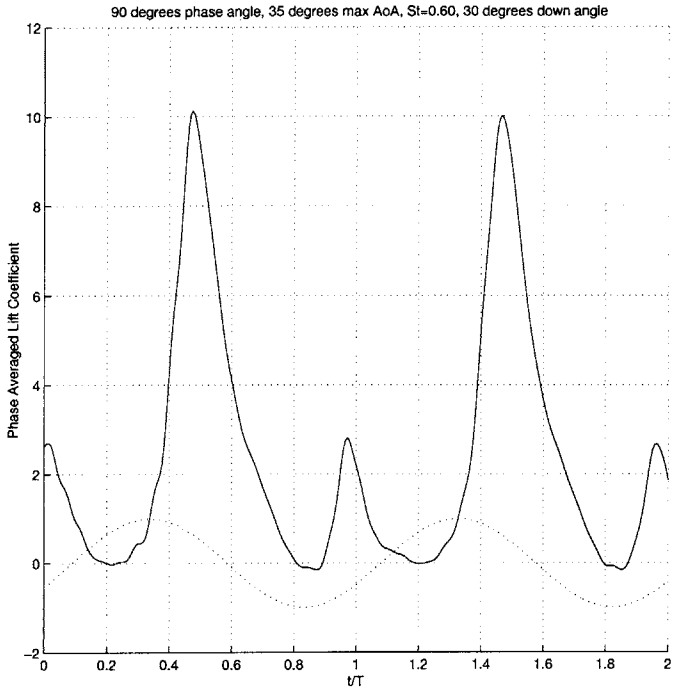

Figure 6-6: Phase averaged lift coefficient, 30° down angle

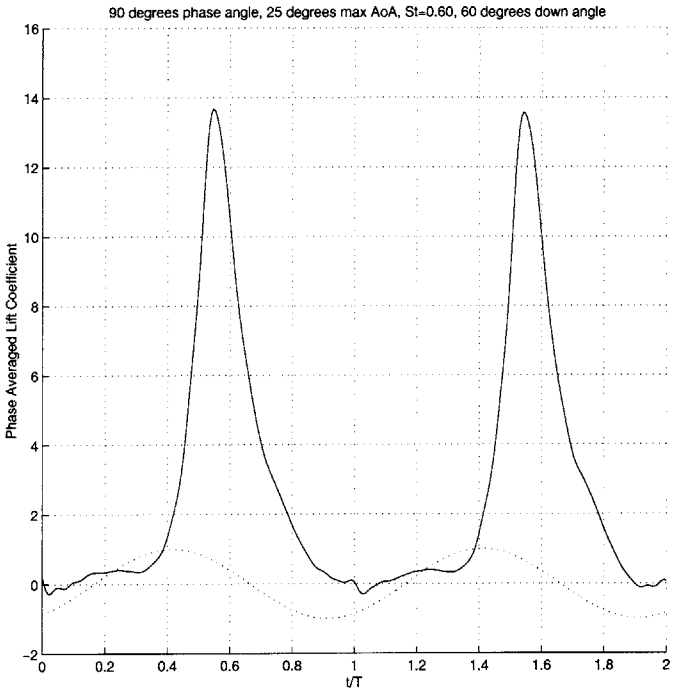

Figure 6-7: Phase averaged lift coefficient, 60° down angle

Impulse starts of the foil revealed that very large starting forces could be created. Tests were performed in which the foil performed one half cycle of heave motion on a stationary carriage. Two methods were used, one in which the foil pitched 90 degrees during one half cycle of heave, and one in which it pitched 180 degrees. Method I tended to produce a large Y force accompanied by a negative X force. This X force was small relative to the Y force. Method II produced even larger Y forces accompanied by a positive X force of similar magnitude. The highest lift forces on our 60 cm by 10 cm foil were 72.55 Newtons for Method I and 138.02 Newtons for Method II. These were both recorded at the highest maximum heave velocity tested, 0.754 m/s. Non dimensionalization of Method II with maximum heave velocity reveals an almost constant force coefficient, hinting that the maximum starting forces available may be extremely high .

6.3 Recommendations for Future Work

High efficiency fell within a plateau in the parameter space. A further set of experiments within this plateau is recommended, especially at more values of maximum angle of attack. It is possible that better performance exists within the plateau.

As noted above, regions of high thrust coefficient can be fairly well predicted based upon the angle of attack profile. High efficiencies fell within three of our angle of attack profile types, so more work needs to be done to describe areas of optimal efficiency. Digital Particle Image Velocimetry (DPIV) from Anderson shows that the vortex wake is optimal within certain regions of the parameter space, and our high efficiencies do in fact fall within the predicted region. Still, the vortex wake pattern in and around the efficiency plateau needs to be studies further. The vortex shedding patterns in the high thrust limit of good efficiency would be of great interest. Specifically, the region from St = 0.50 to 0.60 and angle of attack from 15 to 30 degrees shows the best overall performance. This area of the parameter space has previously been associated with the border between two and four vortex-per-cycle shedding, and visualization in this region could prove very useful.

The tests using higher order heave motion showed promise, and thus lead us to believe that studies should be undertaken beyond simple harmonic motion. We have shown here that small changes in the motion of the foil can have large changes in the angle of attack profile, and thus can drastically change the performance of the foil for a given set of parameters.

Our foil experiments are analogous to a fish or whale tail, which are spanwise stiff and chordwise flexible. Interesting experiments could be conducted by simply performing some of the tests in this thesis with a chordwise flexible foil. In addition, an experiment could be devised to mimic the double angular motion of a penguin or sea lion flipper, instead of the linear and angular combination tested here.

Finally, some of the most encouraging results from this work were from the maneuvering experiments, i.e. using the oscillating foil as a high lift device. The parameter space for these tests was not nearly as large as the one used for propulsion experiments, so many tests remain to be done. Also, almost all of the above recommendations can be repeated for maneuvering tests. Higher order motions should also be applied to the maneuvering case, and visualization of a pitch bias experiment would be most interesting since, to our knowledge, none has been done before.

Appendix A

Propulsion Time Data

In the following figures we show data from selected propulsion experiments. All plotted data has been filtered using a second order Butterworth filter with a cut-off frequency of five times the fundamental oscillation frequency. MATLAB's FILTFILT function was used to prevent any phase shift, and all filtered data were plotted against raw data as a visual check for attenuation. Large attenuation did not occur, but these filtered data are intended for visualization and comparison only. The data used in thrust and efficiency calculations were NOT filtered.

We show all five data traces recorded during an experiment. The angle of attack profile calculated from the heave and pitch position is also presented. This profile was calculated from the potentiometer and heave encoder signal. The heave position derivative was calculated using a center-difference scheme in MATLAB. Note that in some of the high thrust runs, the pitch position is distorted slightly due to small compliance in the system. Although this distortion is noticeable in the calculated angle of attack, the lift and thrust measurements remain more symmetrical.

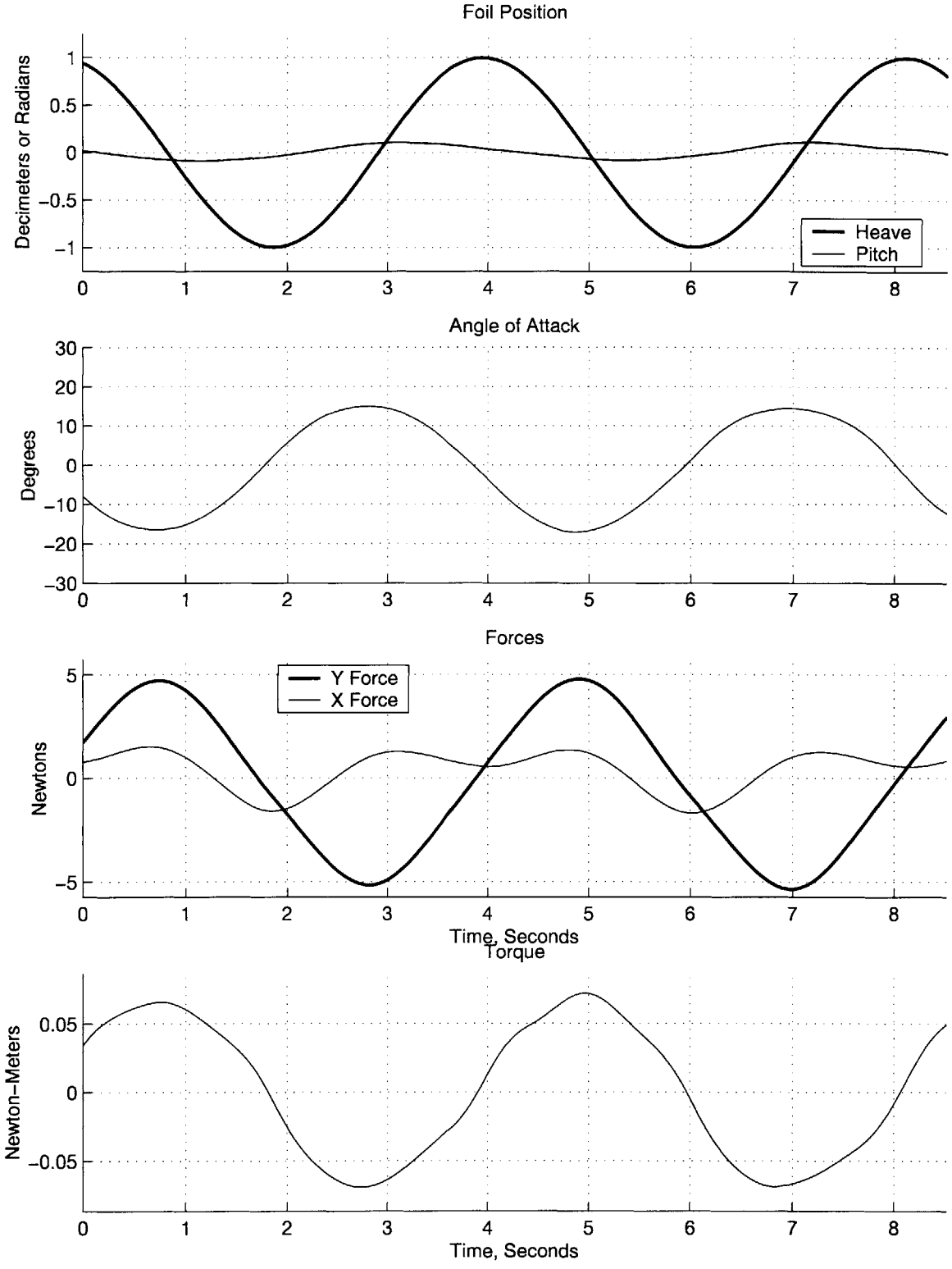

Figure A-1: Phase Angle = 70°, Max AoA = 15°, St = 0.12

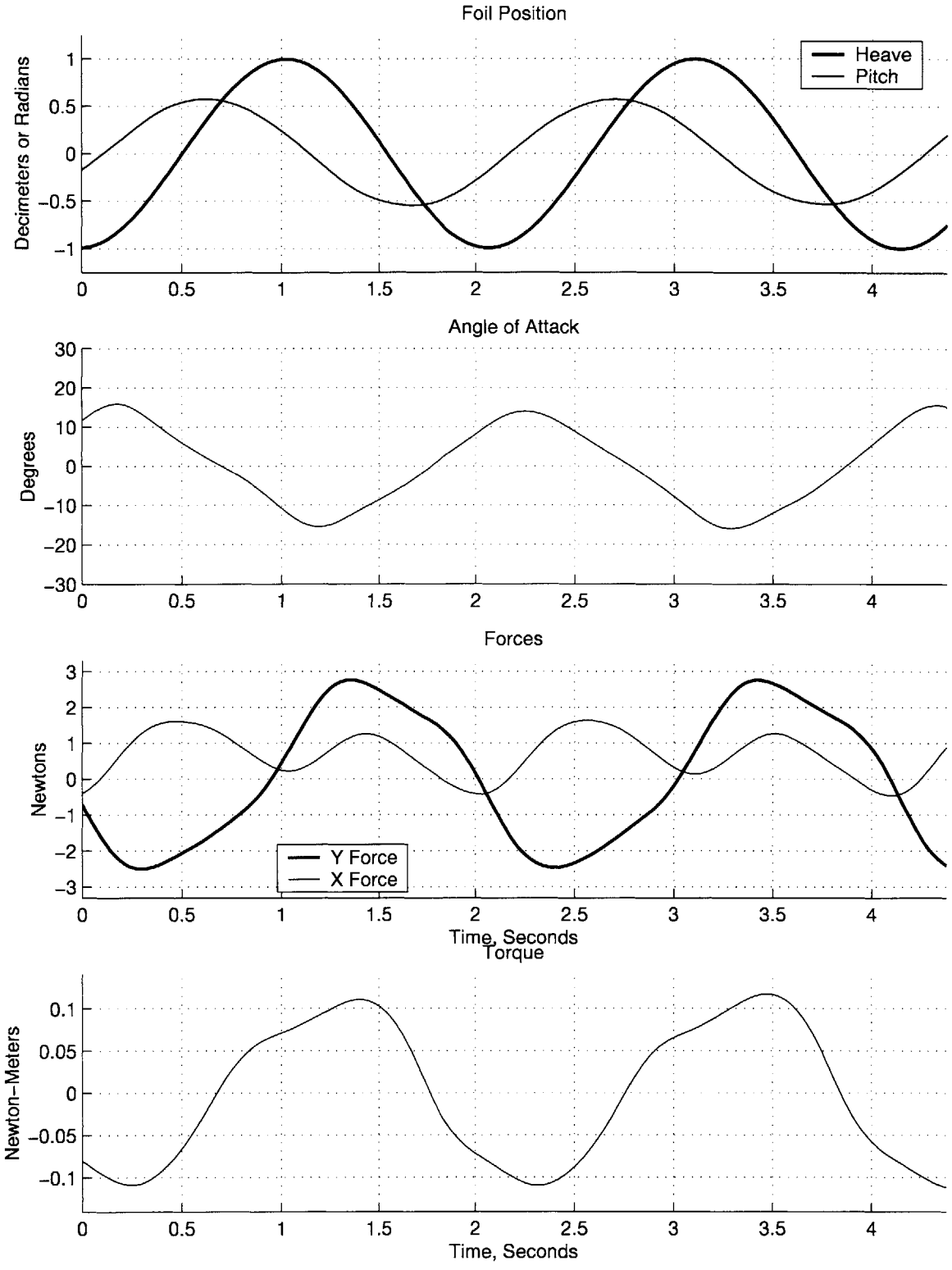

Figure A-2: Phase Angle = 70°, Max AoA = 15°, St = 0.24

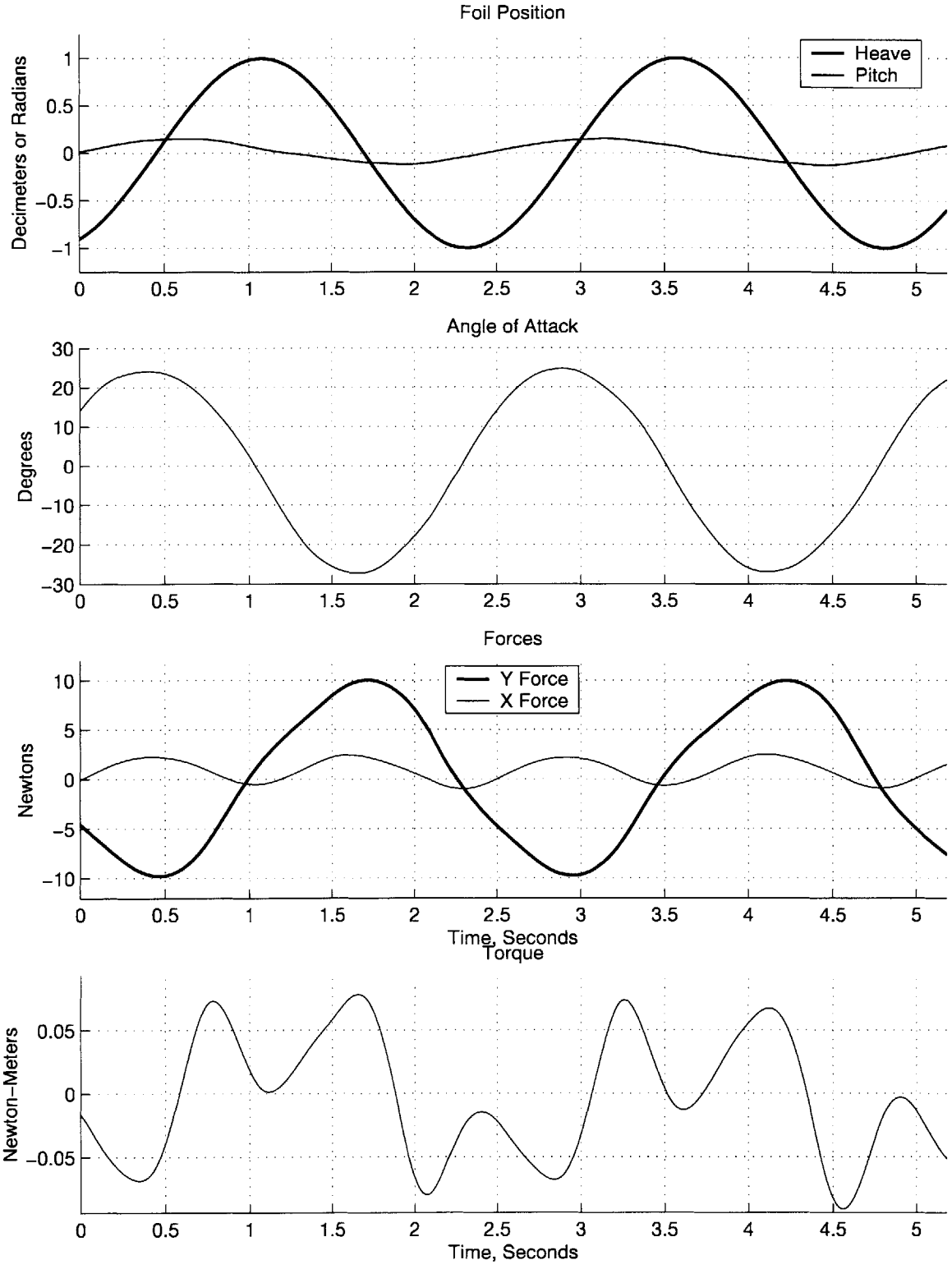

Figure A-3: Phase Angle = 70°, Max AoA = 25°, St = 0.20

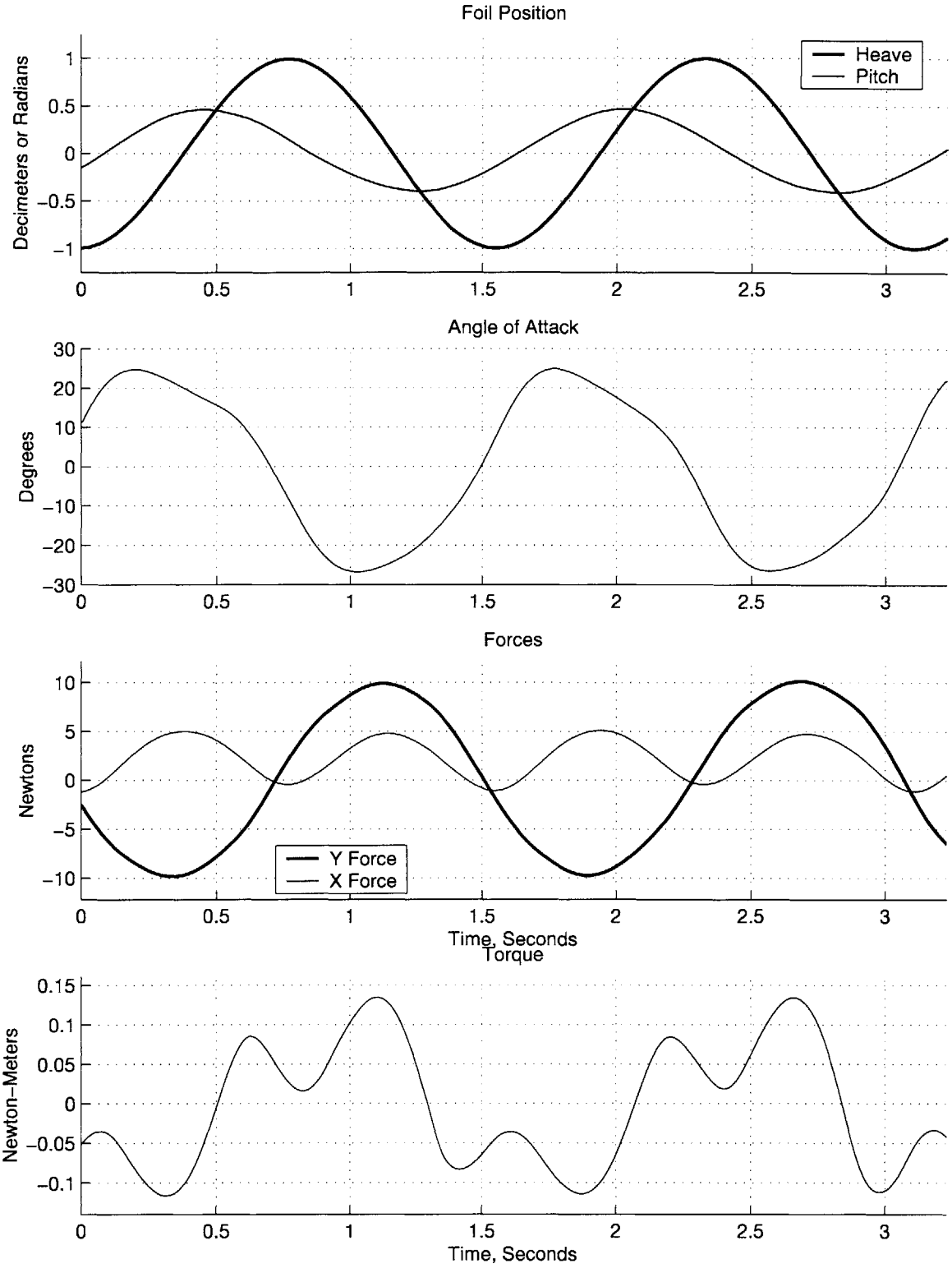

Figure A-4: Phase Angle = 70°, Max AoA = 25°, St = 0.32

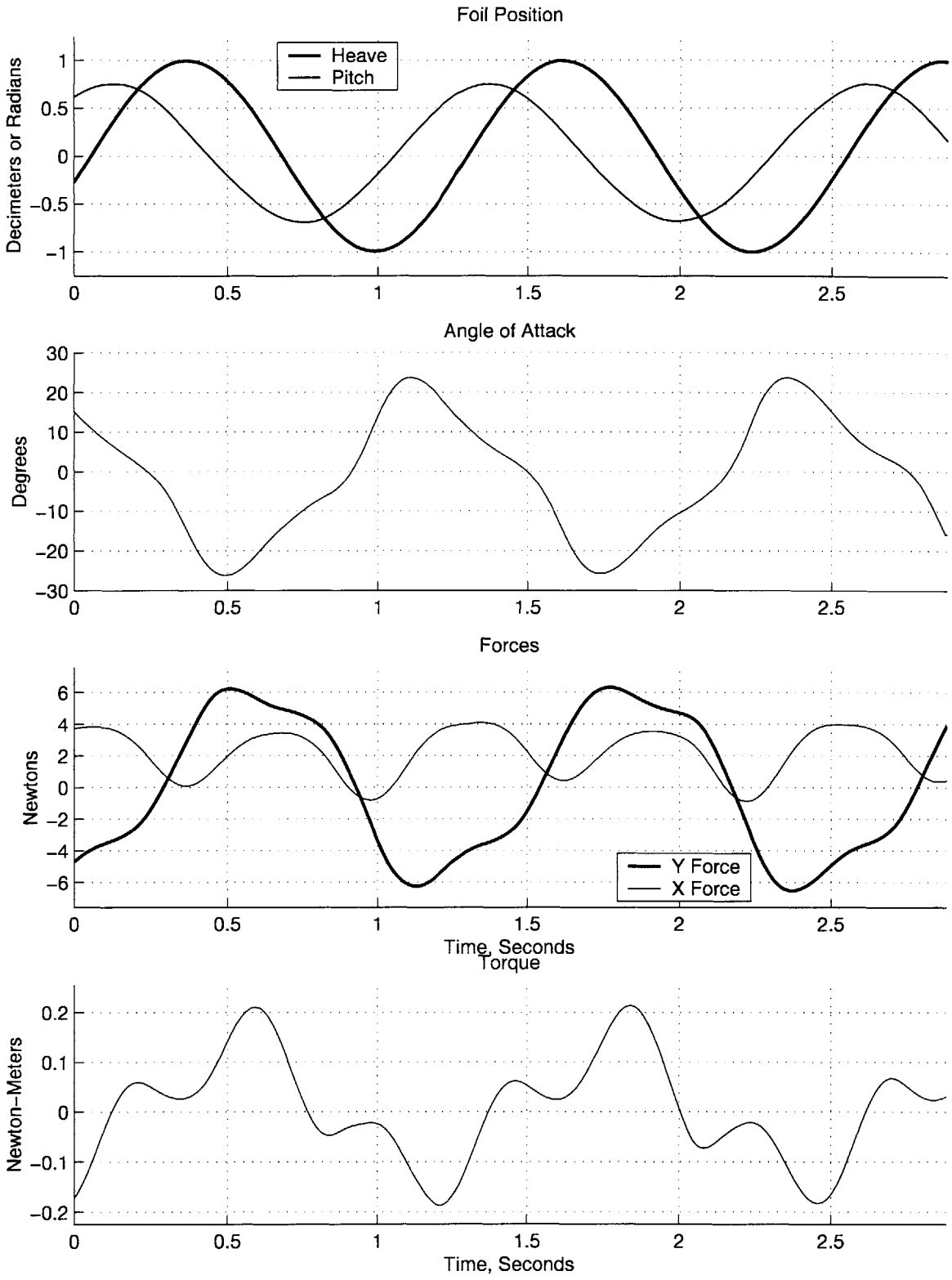

Figure A-5: Phase Angle = 70°, Max AoA = 25°, St = 0.40

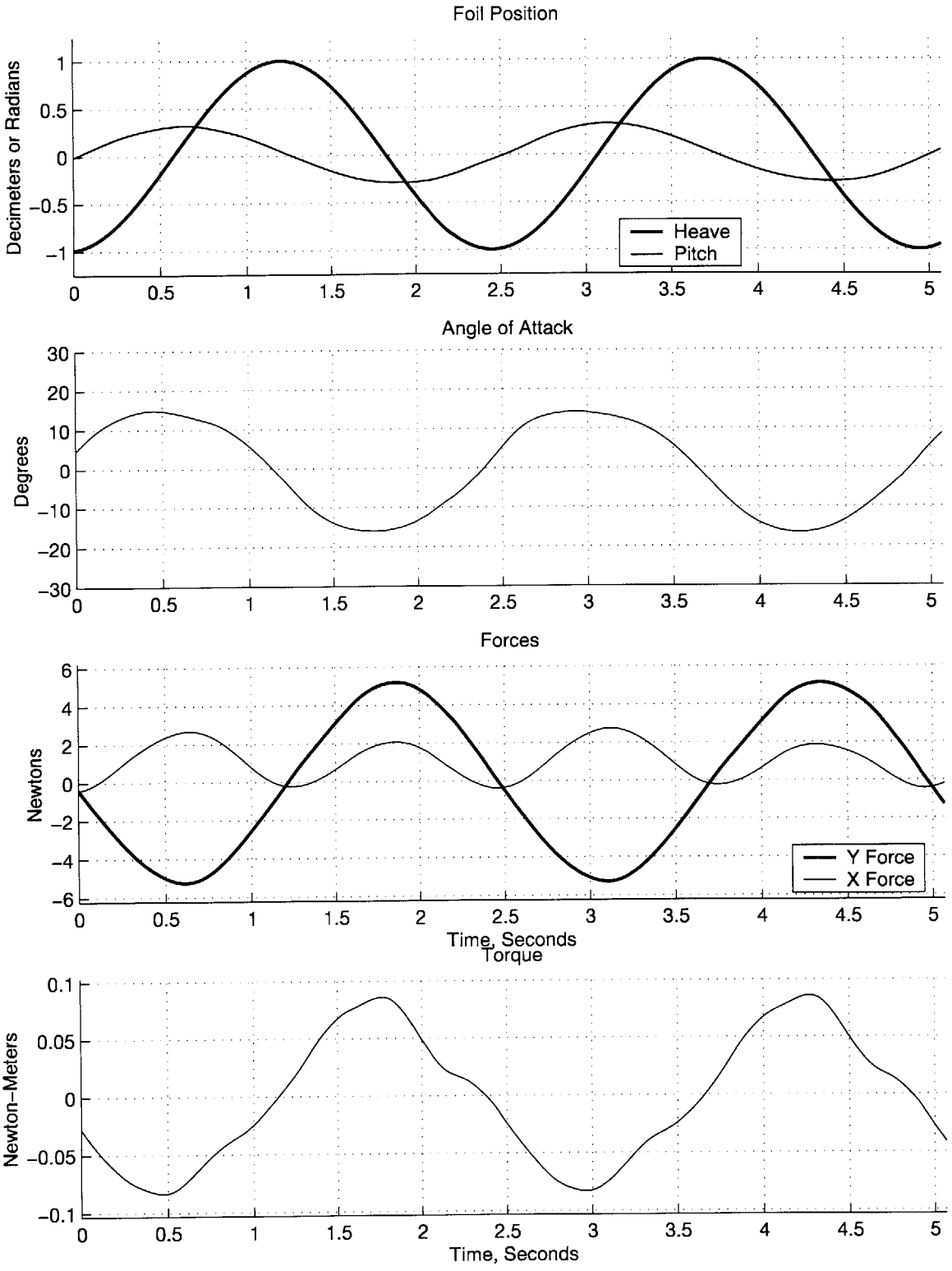

Figure A-6: Phase Angle = 80°, Max AoA = 15°, St = 0.20

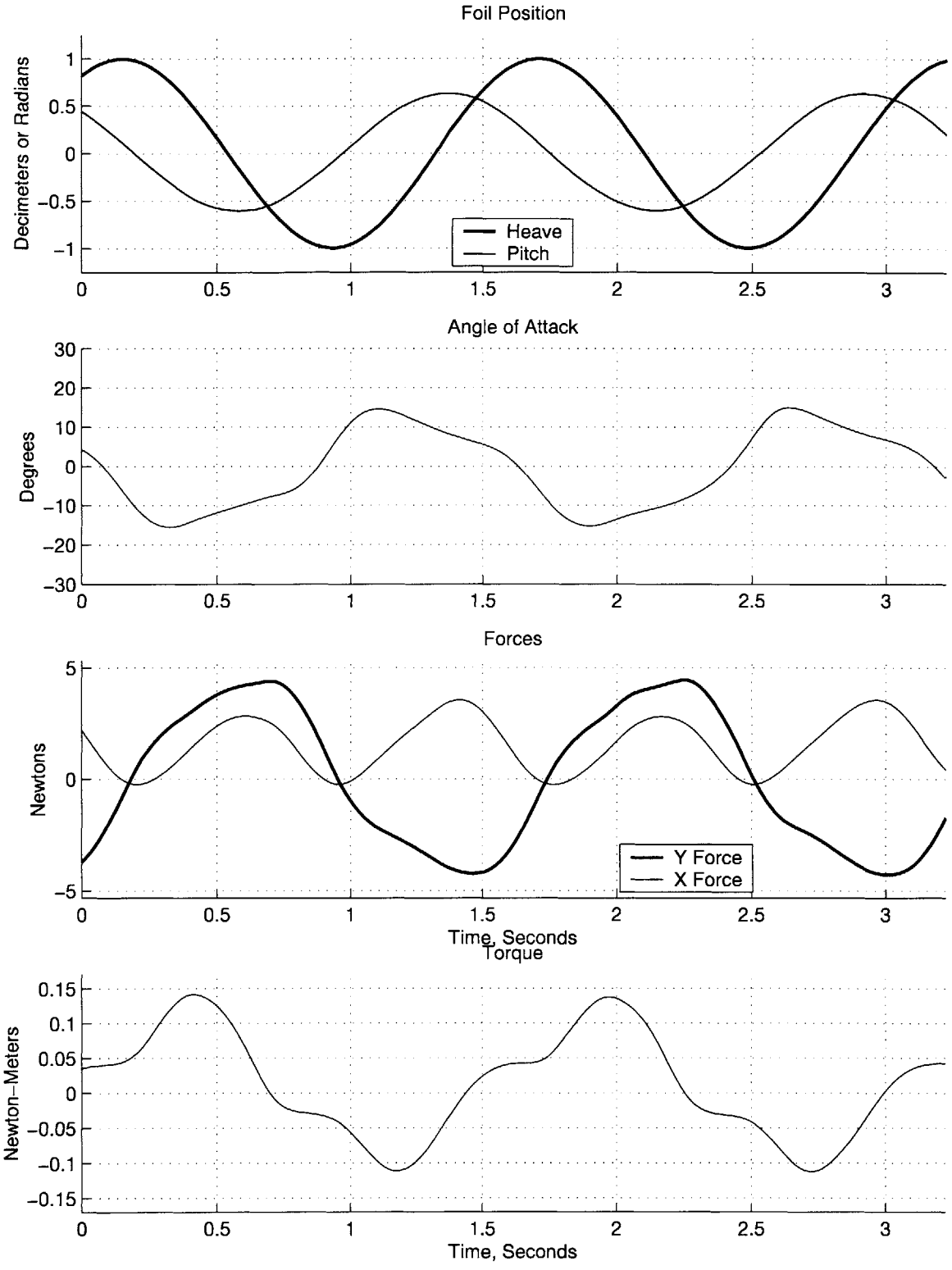

Figure A-7: Phase Angle = 80°, Max AoA = 15°, St = 0.32

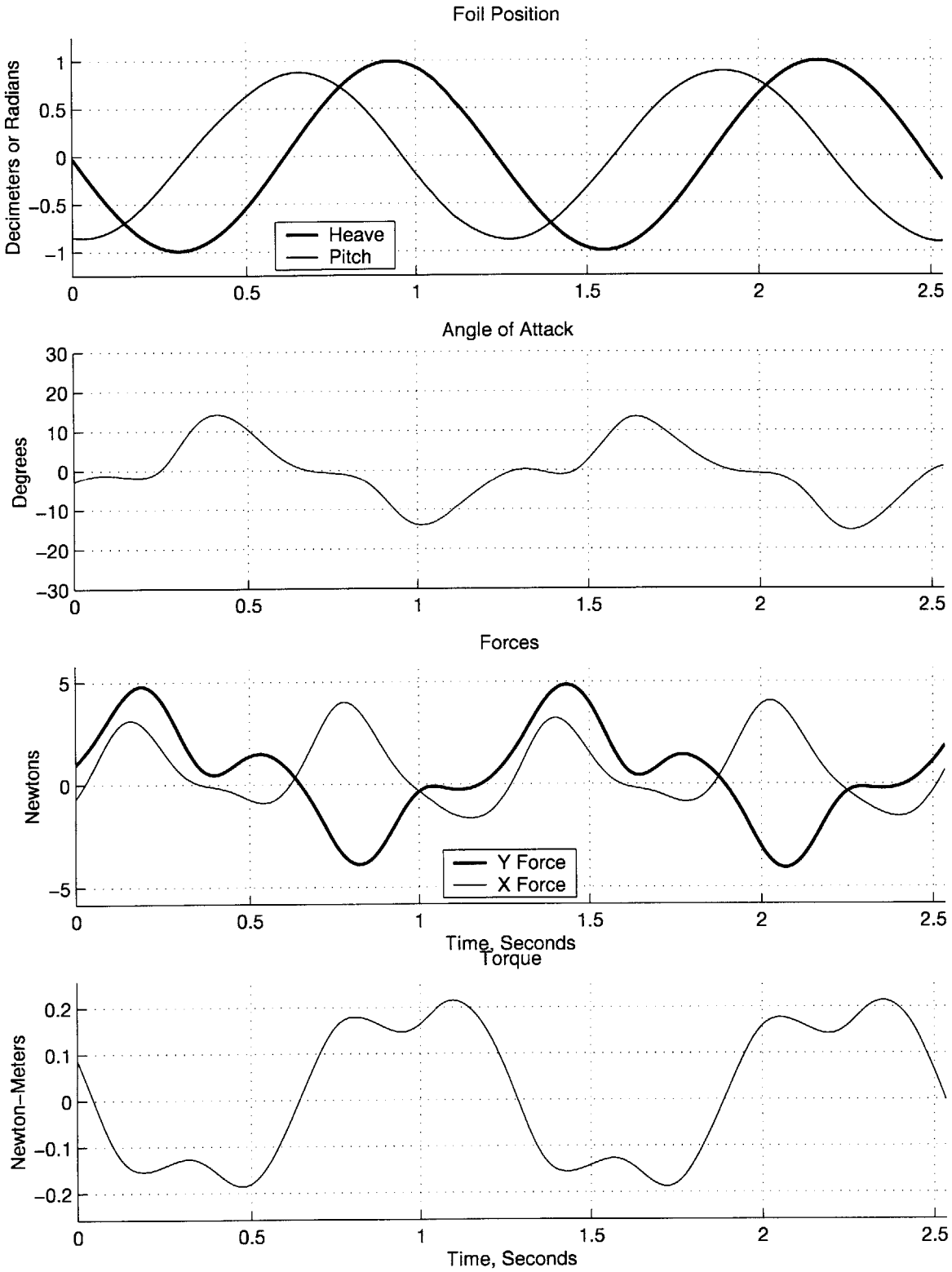

Figure A-8: Phase Angle = 80°, Max AoA = 15°, St = 0.40

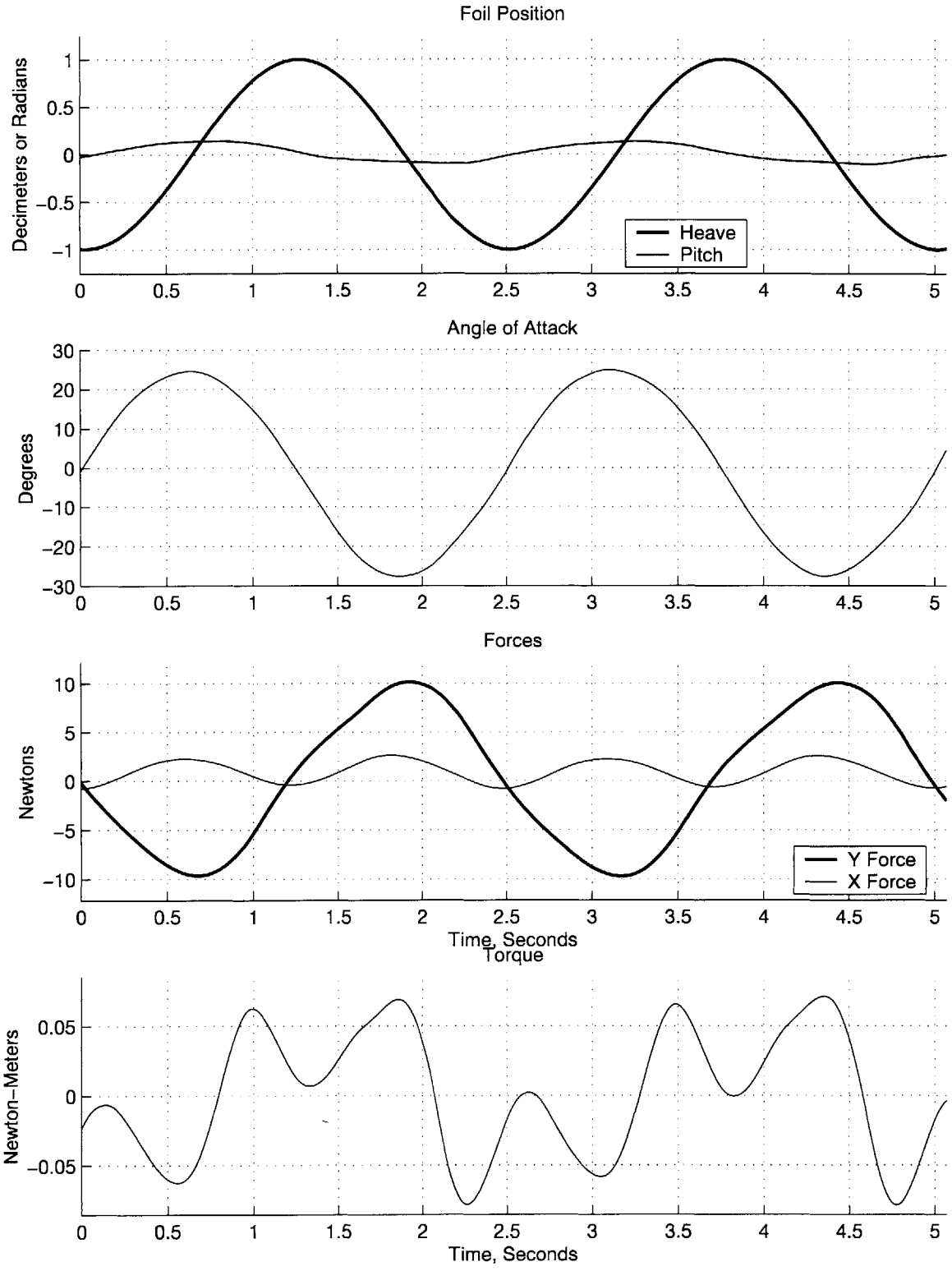

Figure A-9: Phase Angle = 80°, Max AoA = 25°, St = 0.20

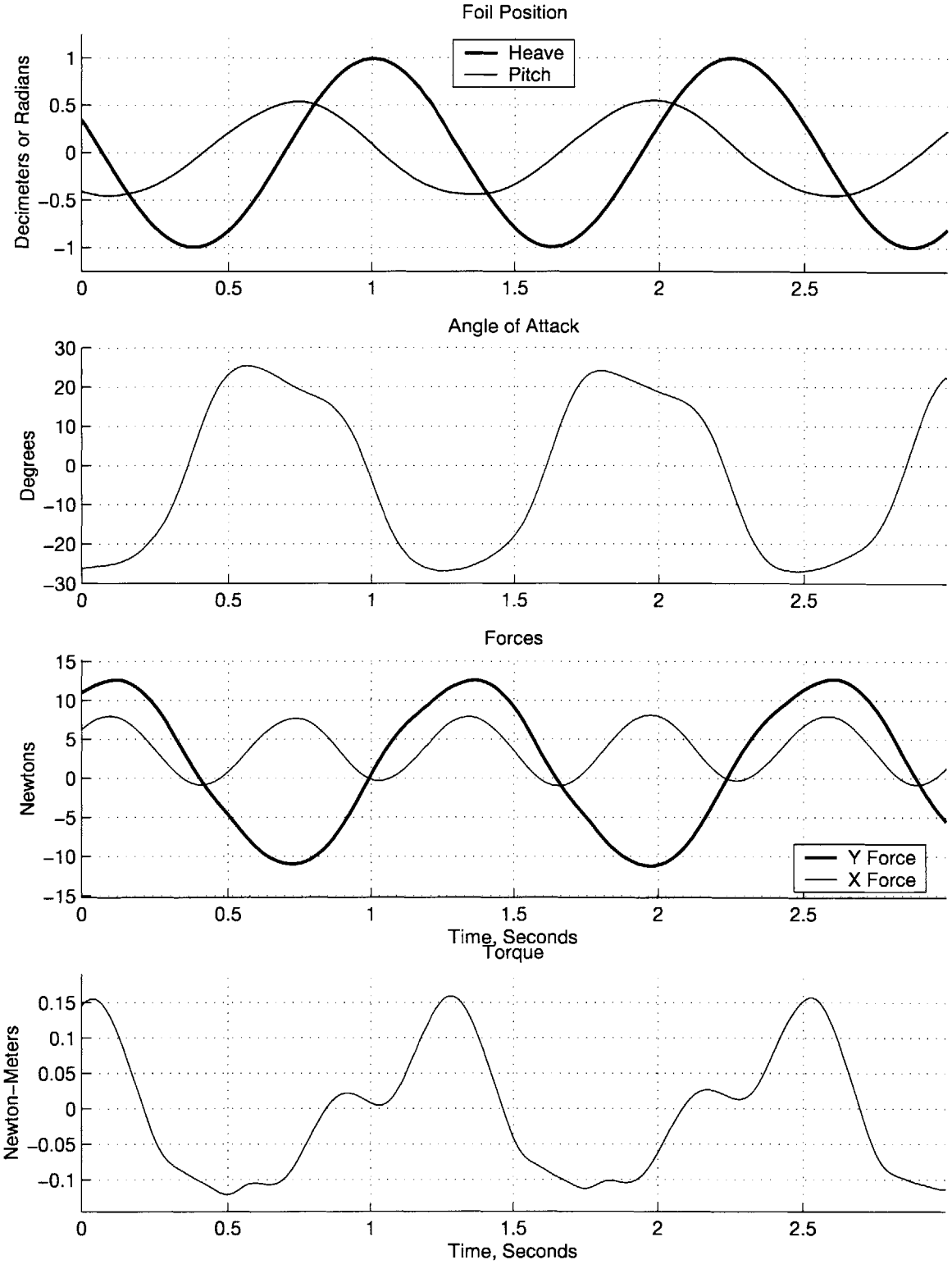

Figure A-10: Phase Angle = 80°, Max AoA = 25°, St = 0.40

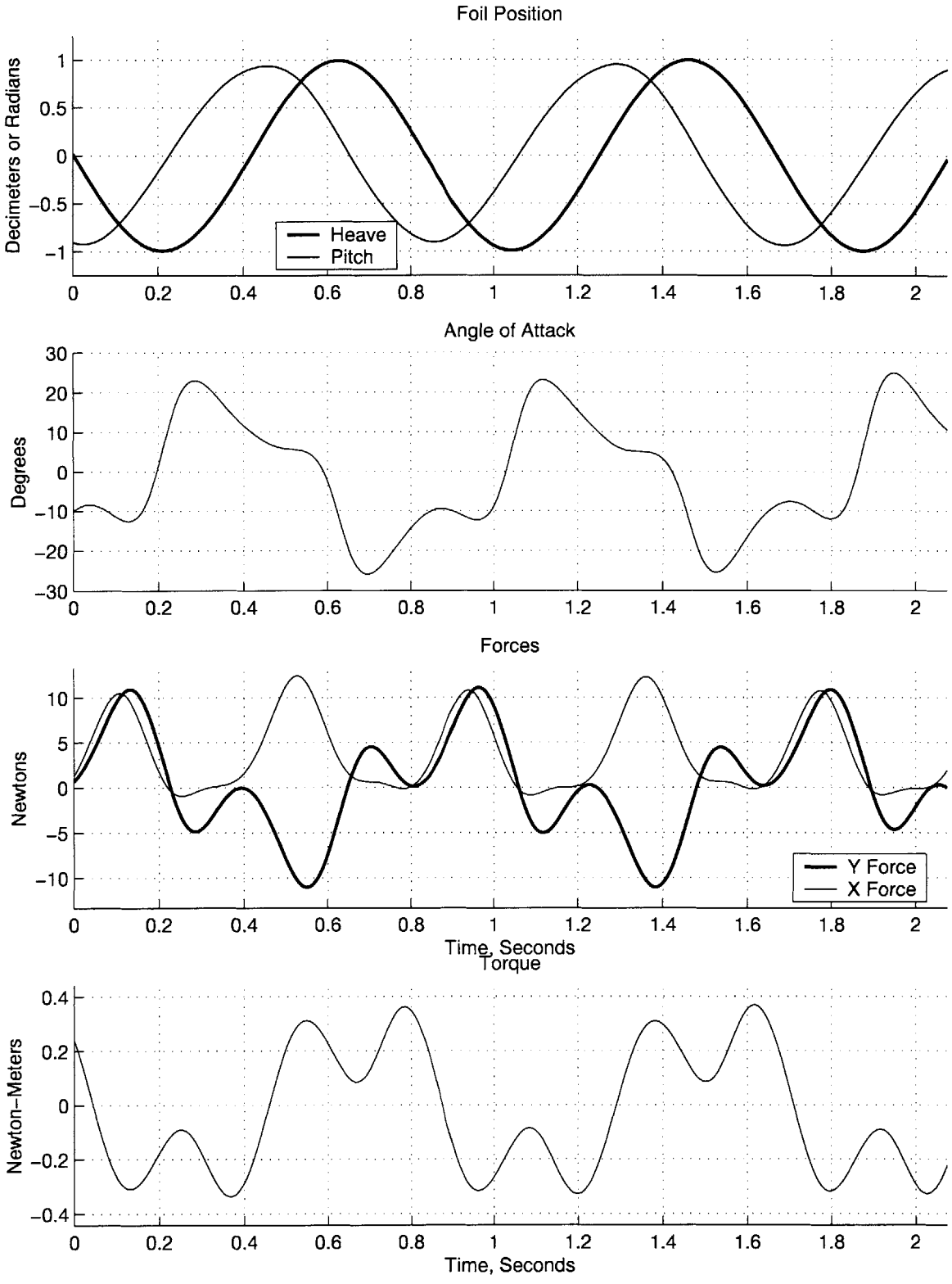

Figure A-11: Phase Angle = 80°, Max AoA = 25°, St = 0.60

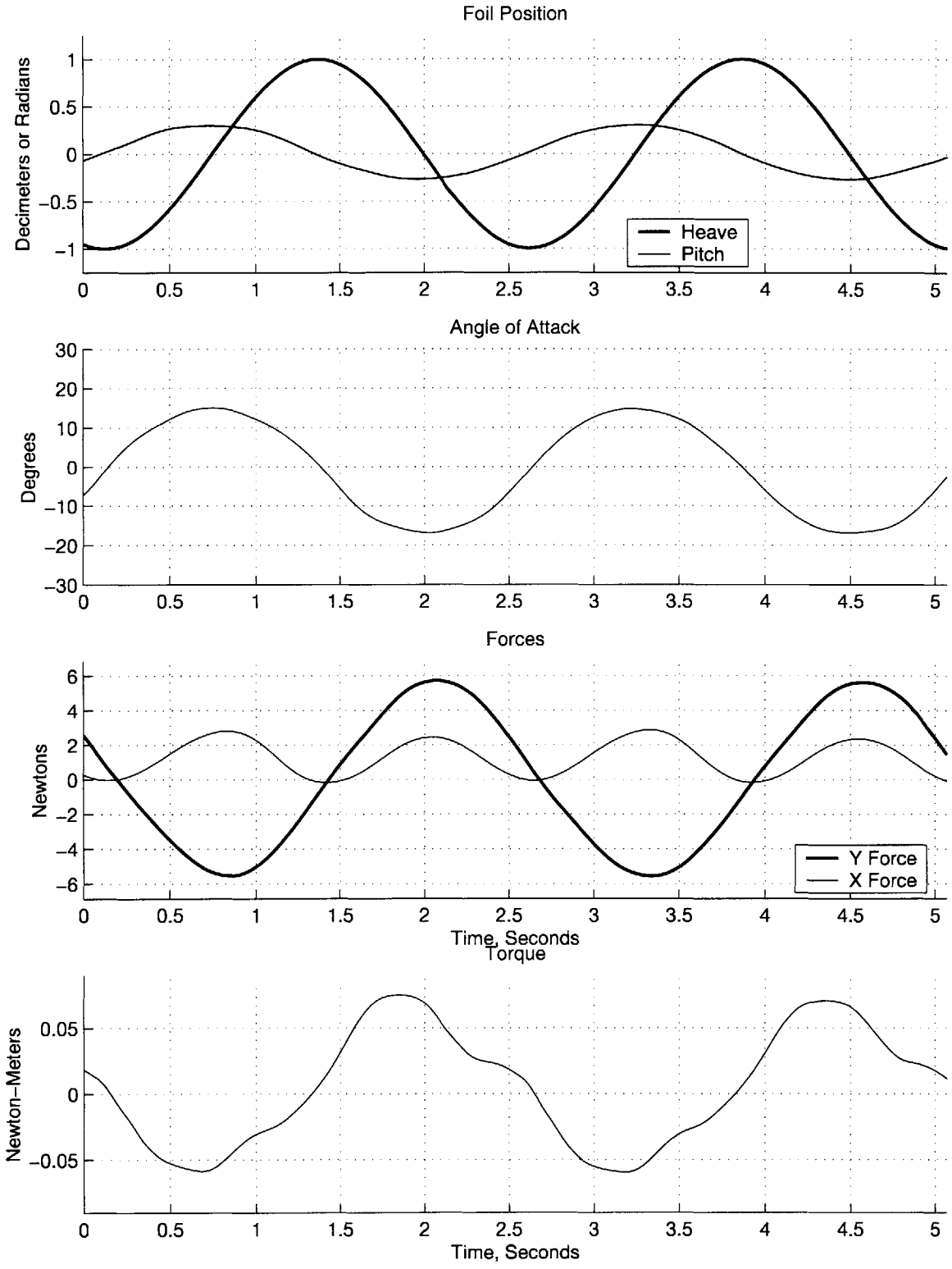

Figure A-12: Phase Angle = 90°, Max AoA = 15°, St = 0.20

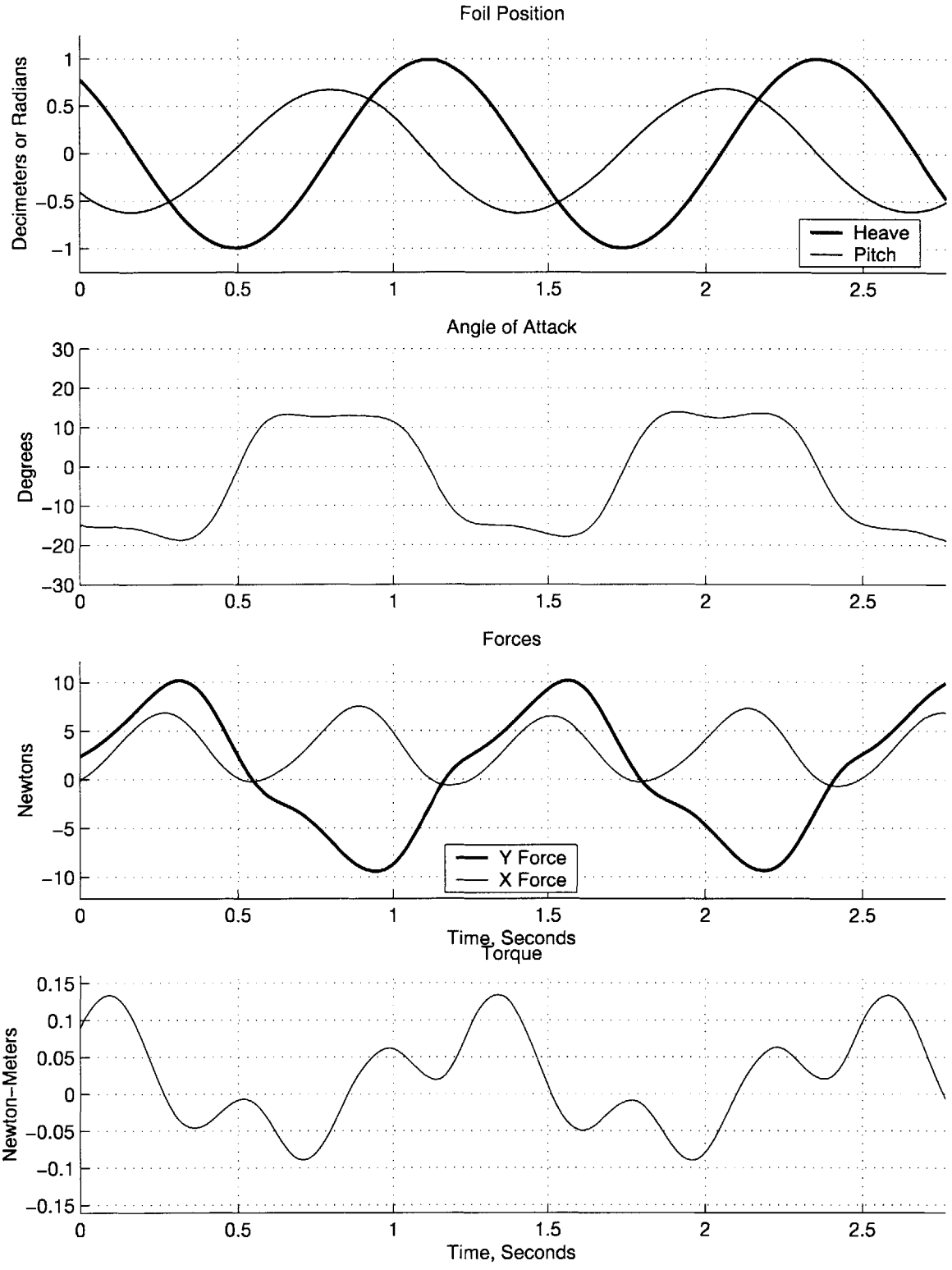

Figure A-13: Phase Angle = 90°, Max AoA = 15°, St = 0.40

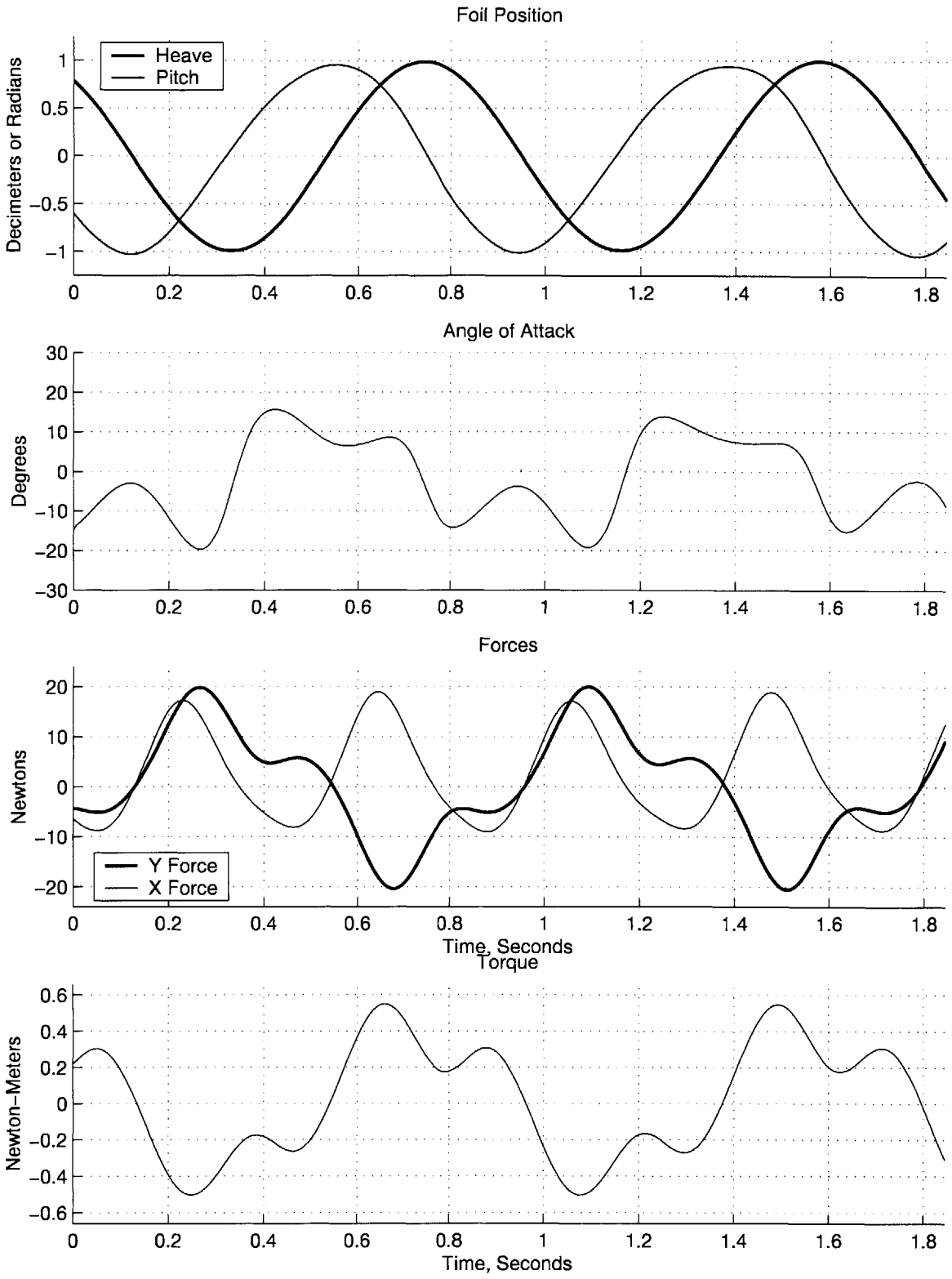

Figure A-14: Phase Angle = 90°, Max AoA = 15°, St = 0.60

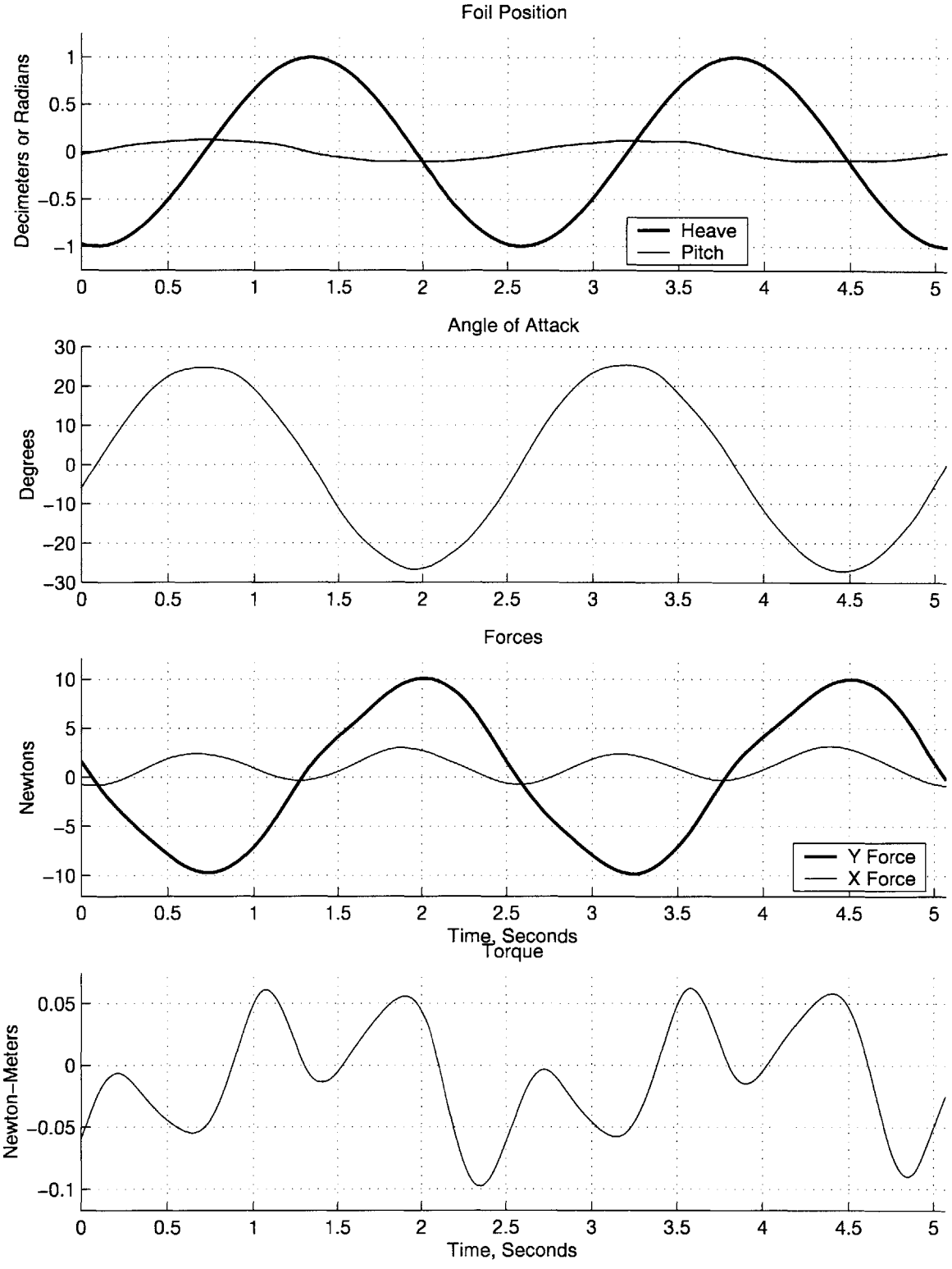

Figure A-15: Phase Angle = 90°, Max AoA = 25°, St = 0.20

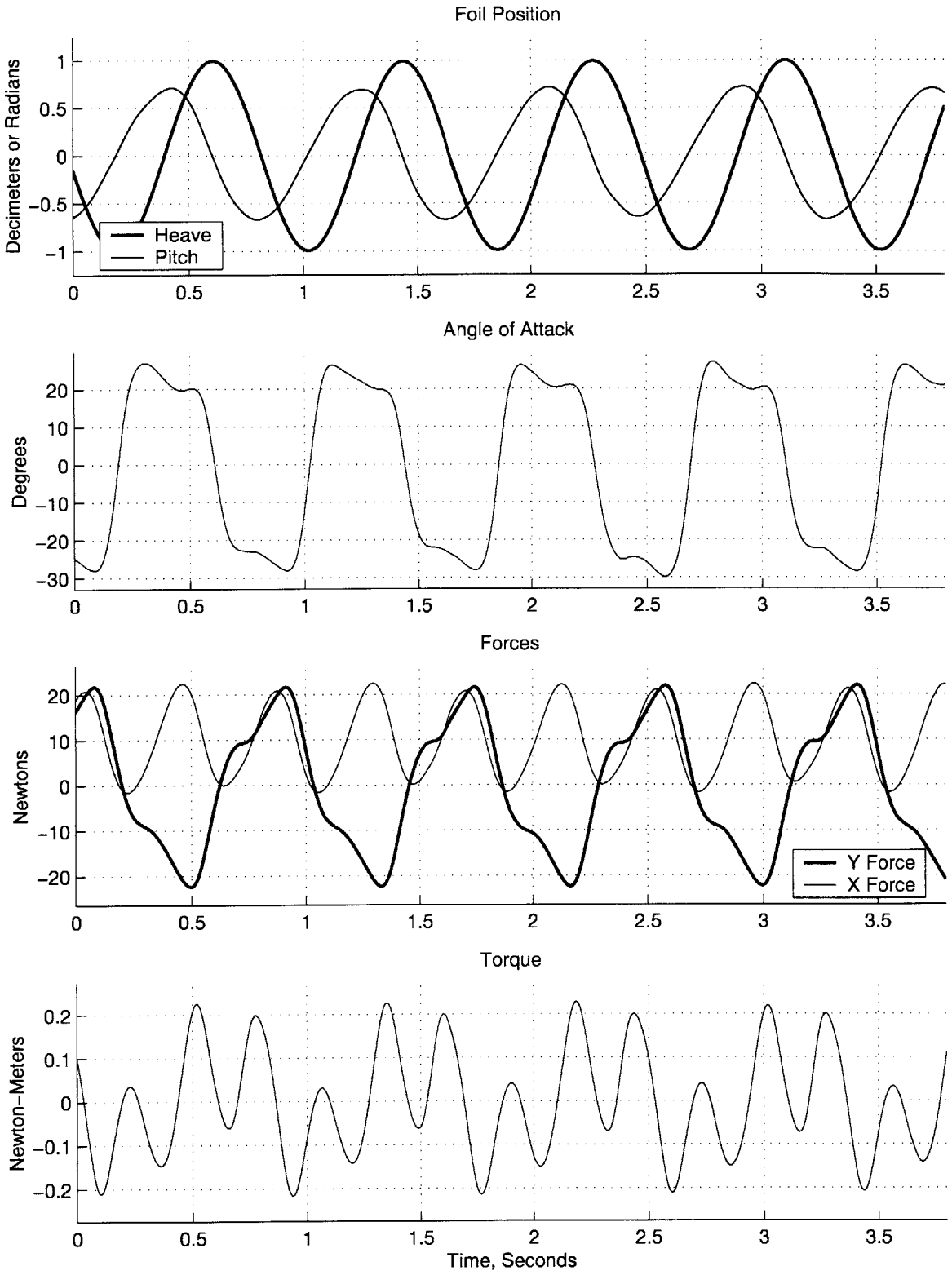

Figure A-16: Phase Angle = 90°, Max AoA = 25°, St = 0.60

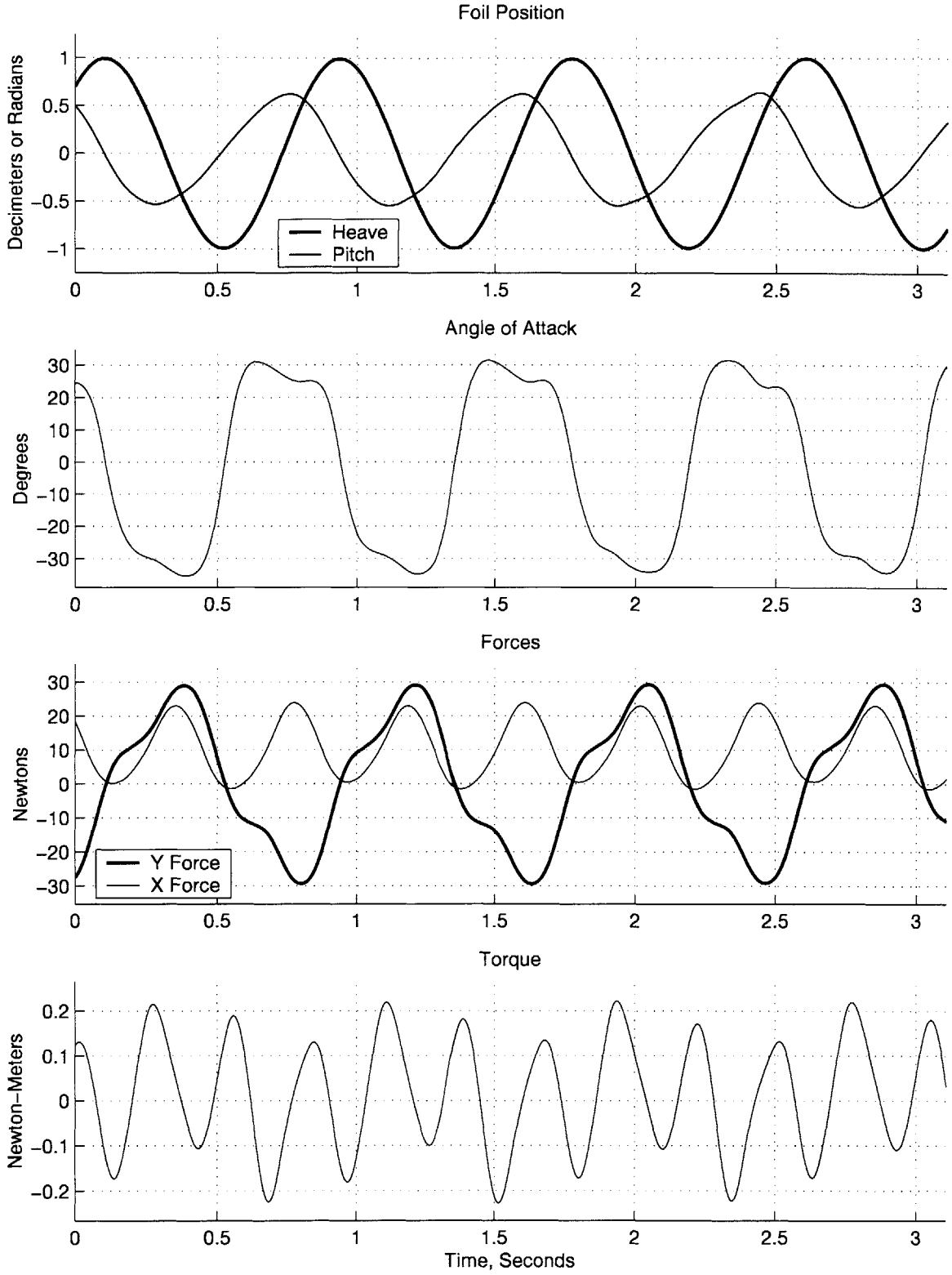

Figure A-17: Phase Angle = 90°, Max AoA = 30°, St = 0.60

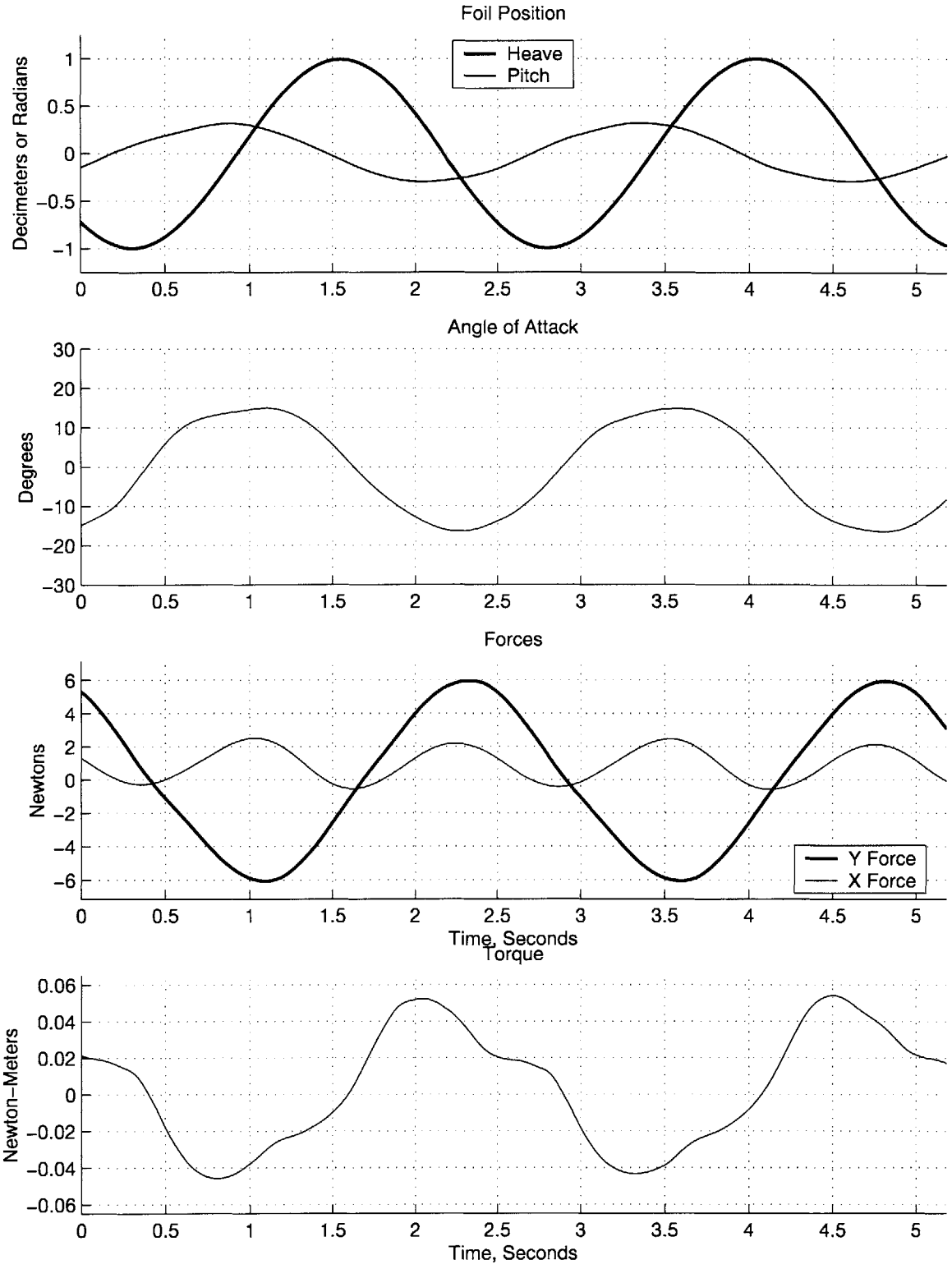

Figure A-18: Phase Angle = 100°, Max AoA = 15°, St = 0.20

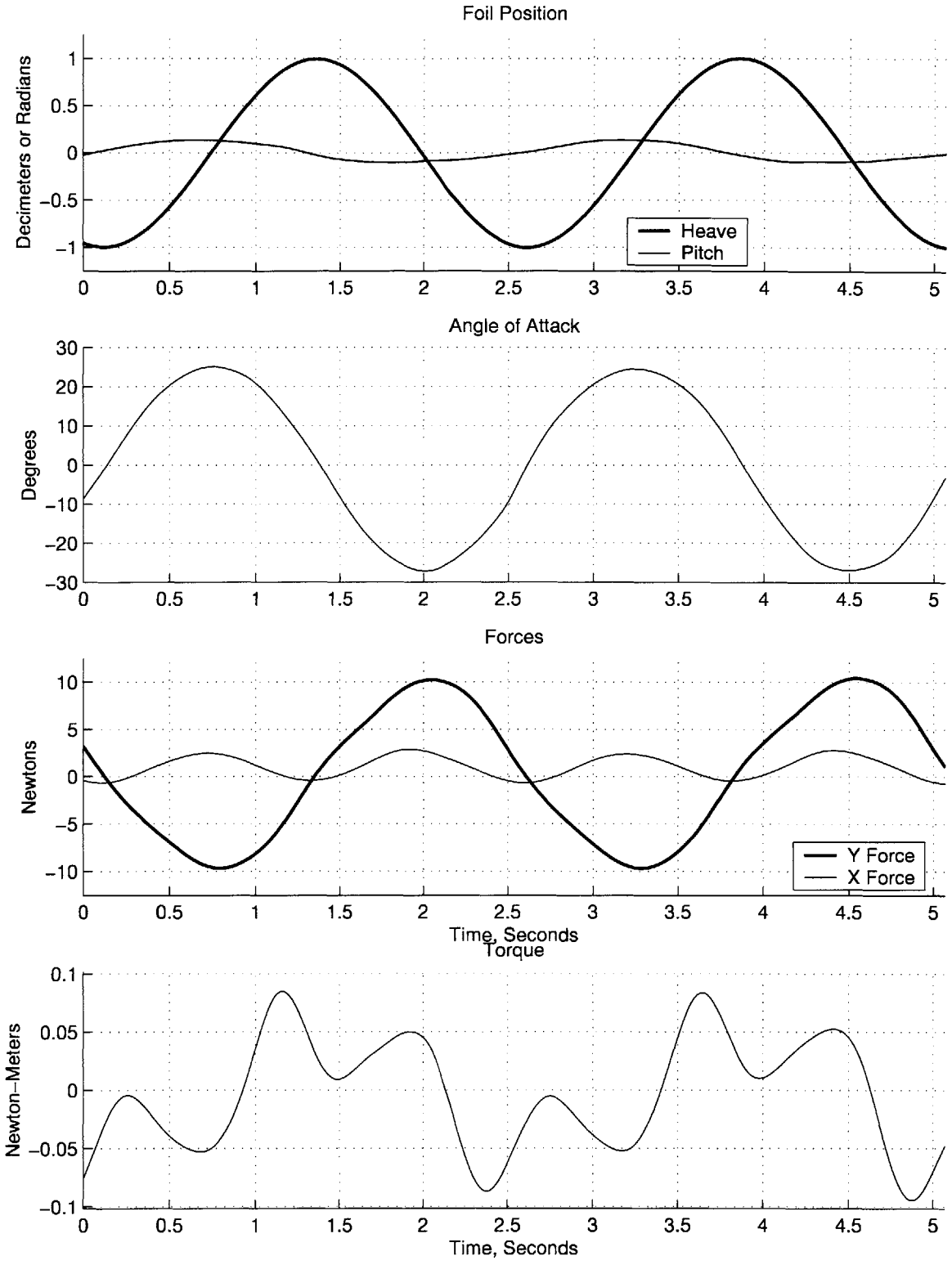

Figure A-19: Phase Angle = 100°, Max AoA = 25°, St = 0.20

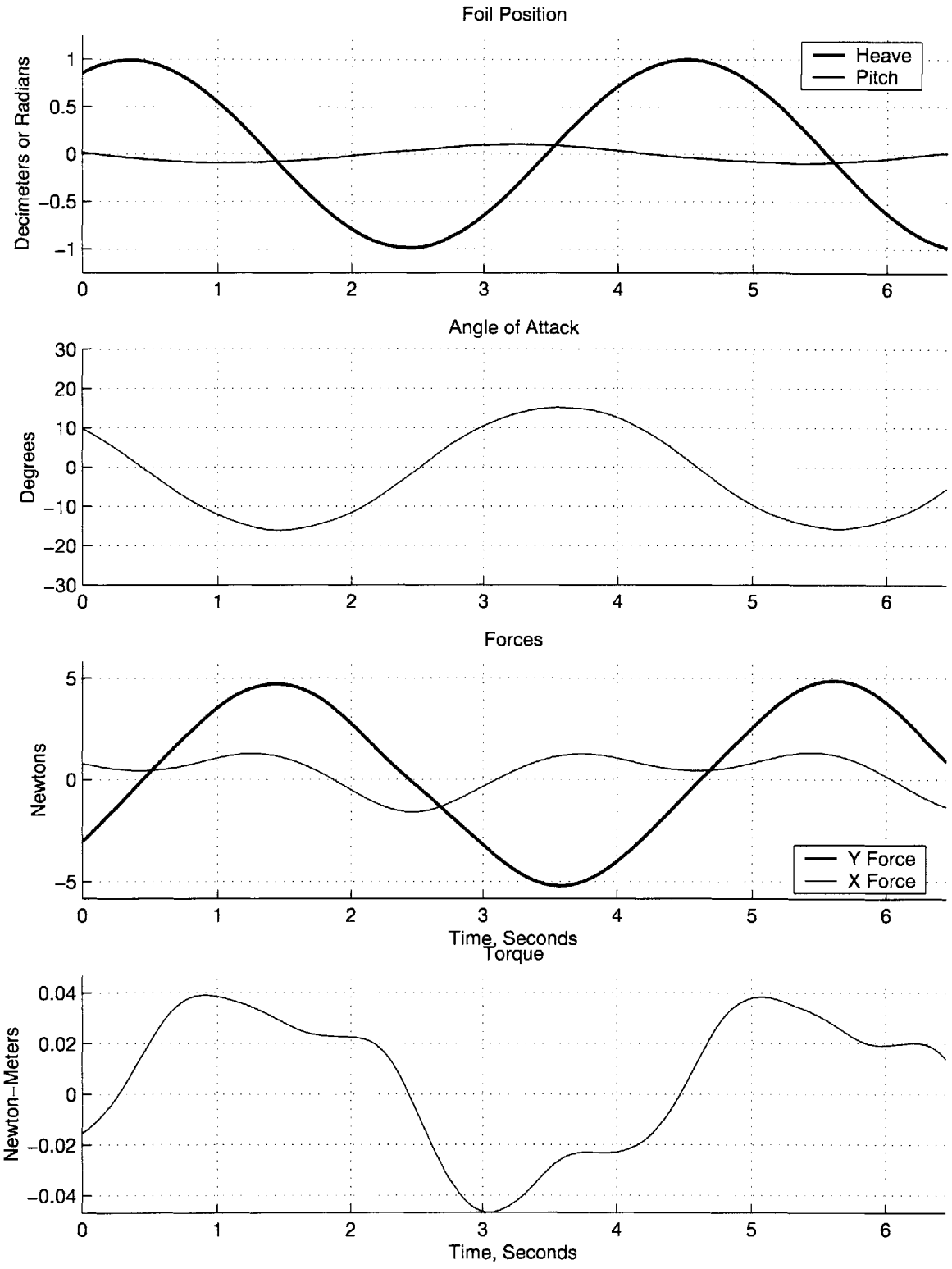

Figure A-20: Phase Angle = 110°, Max AoA = 15°, St = 0.12

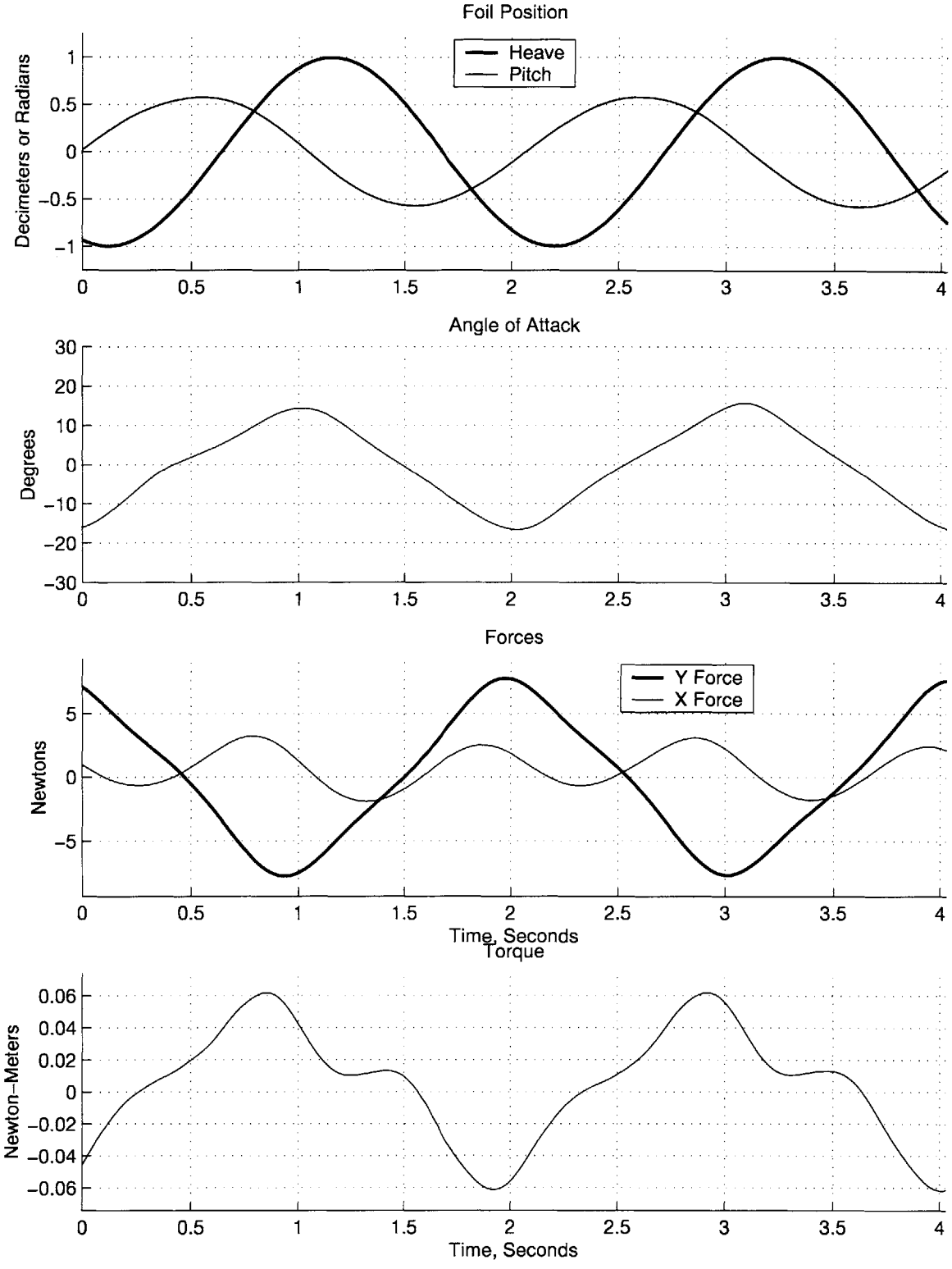

Figure A-21: Phase Angle = 110°, Max AoA = 15°, St = 0.24

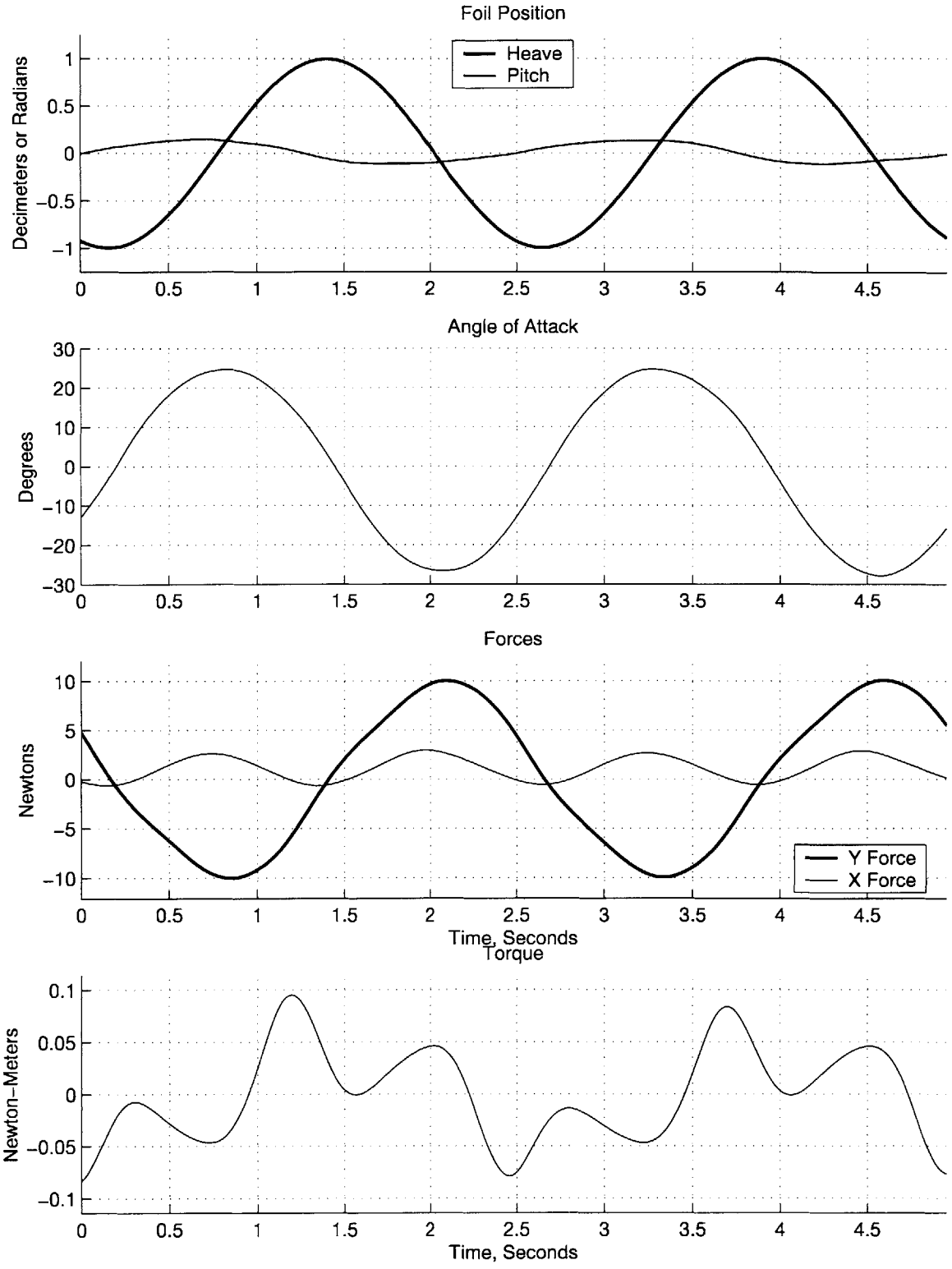

Figure A-22: Phase Angle = 110°, Max AoA = 25°, St = 0.20

Appendix B

Maneuvering Time Data and Vector Plots

In these figures we show data from selected pitch bias experiments. Filter and calculation comments are the same as those for Appendix A. Instantaneous vector plots follow the convention of Figures 4-5 and 4-6. Again, these plots are for general visualization. Scaling between X and Y components of the instantaneous vectors may not be 1:1. Refer to the X and Y force time traces to compare the magnitudes of these force components.

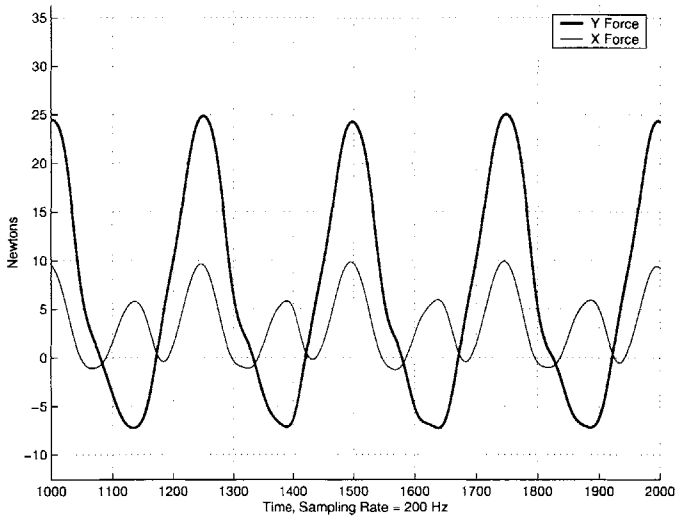

Figure B-1: Phase Angle = 90°, Max AoA = 25°, St = 0.40, Static Offset = 10°

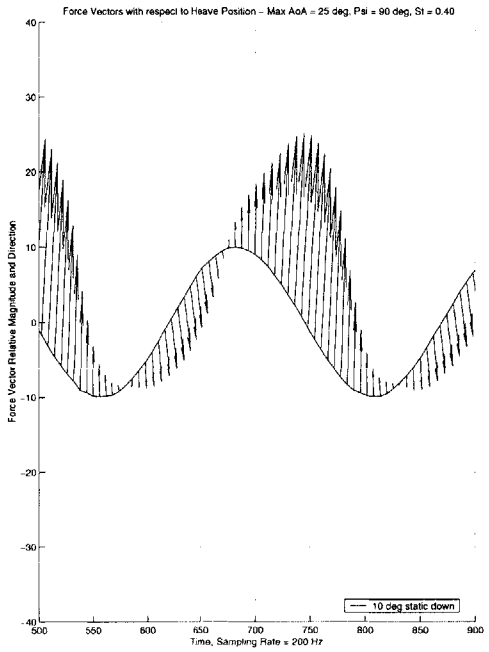

Figure B-2: Instantaneous Force Vectors for B-1

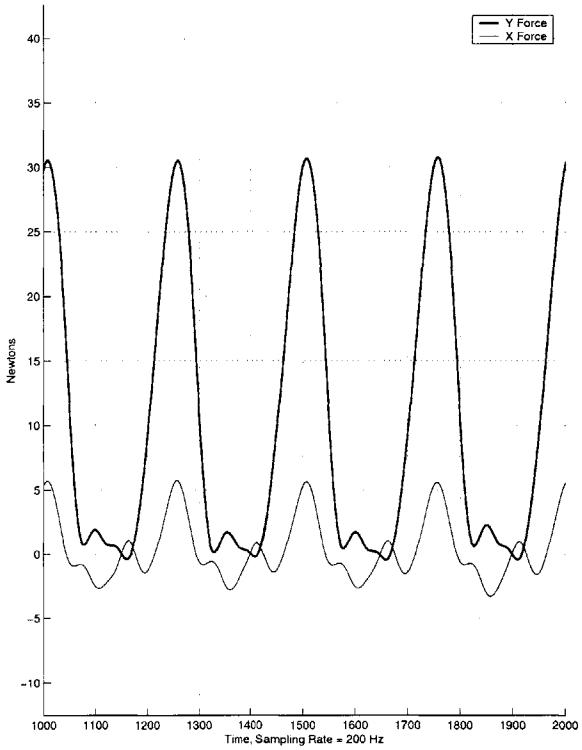

Figure B-3: Phase Angle = 90°, Max AoA = 25°, St = 0.40, Static Offset = 20°

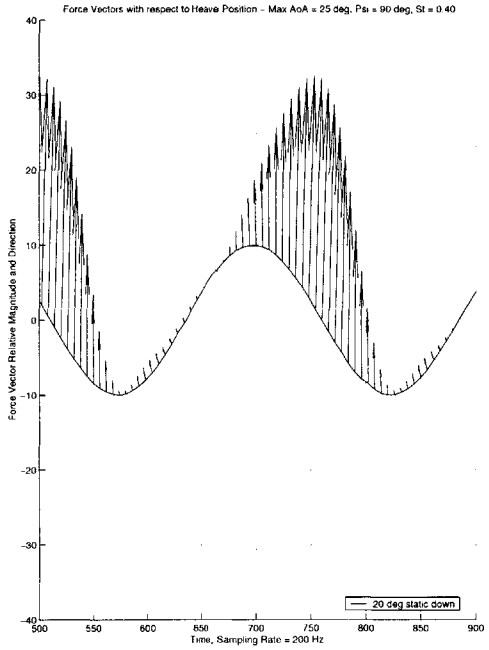

Figure B-4: Instantaneous Force Vectors for B-3

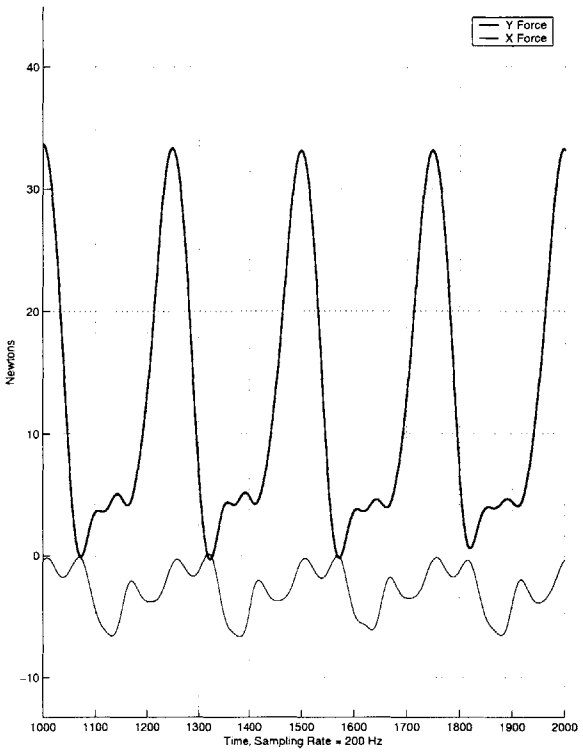

Figure B-5: Phase Angle = 90°, Max AoA = 25°, St = 0.40, Static Offset = 30°

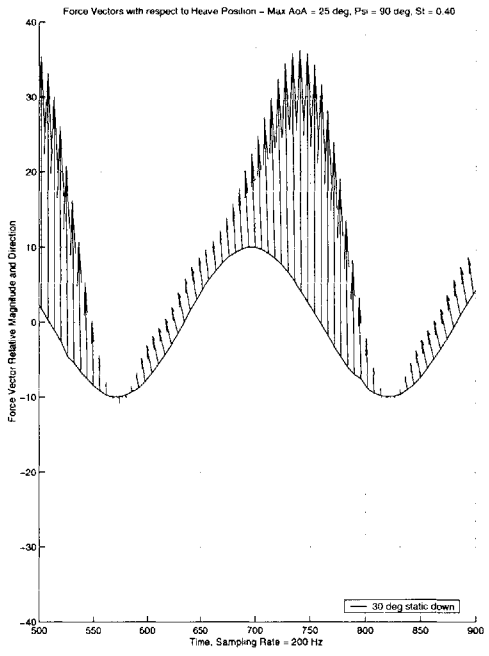

Figure B-6: Instantaneous Force Vectors for B-5

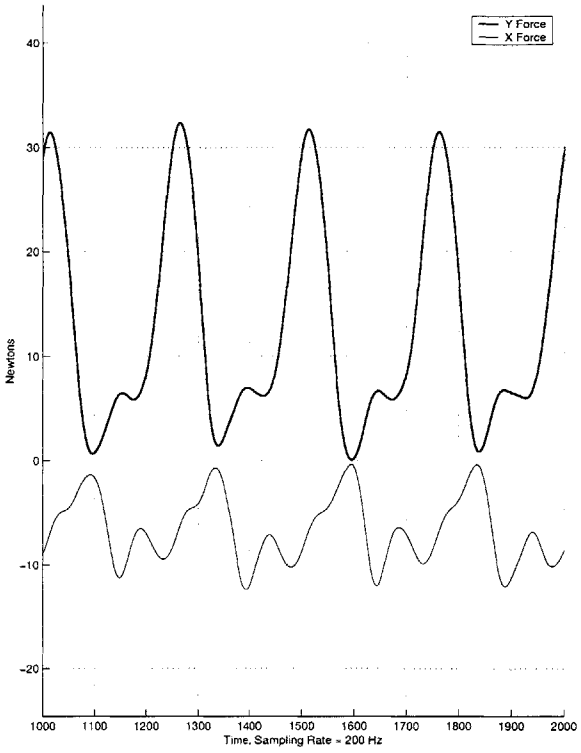

Figure B-7: Phase Angle = 90°, Max AoA = 25°, St = 0.40, Static Offset = 40°

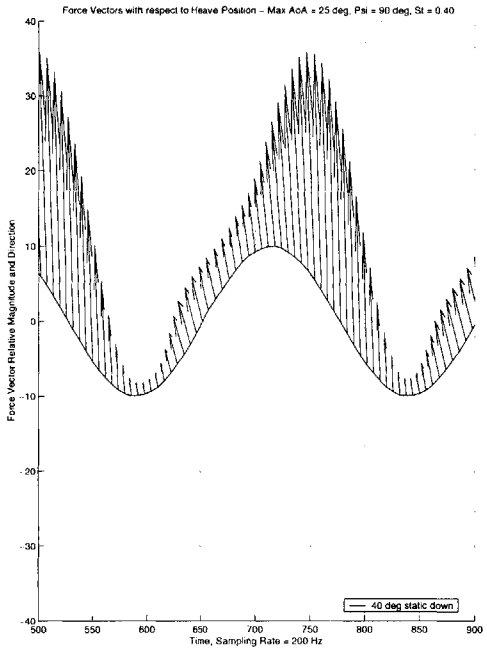

Figure B-8: Instantaneous Force Vectors for B-7

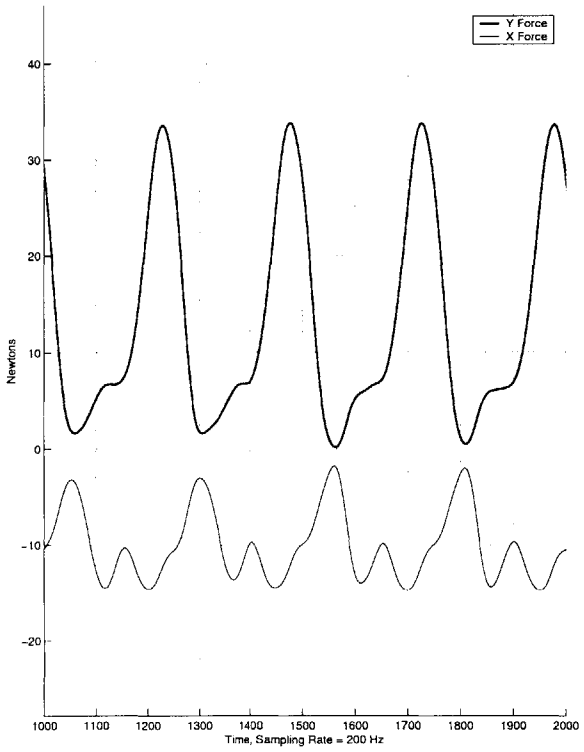

Figure B-9: Phase Angle = 90°, Max AoA = 25°, St = 0.40, Static Offset = 50°

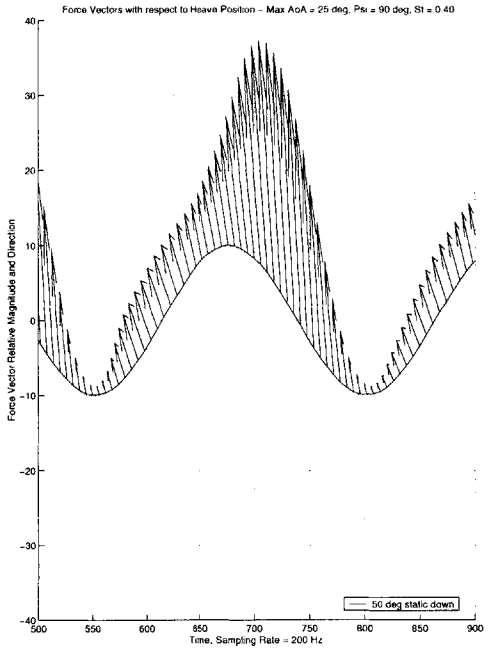

Figure B-10: Instantaneous Force Vectors for B-9

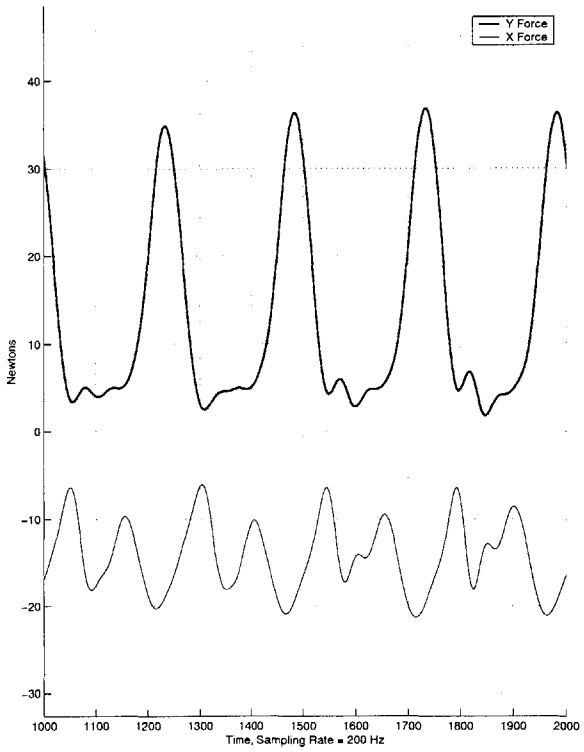

Figure B-11: Phase Angle = 90°, Max AoA = 25°, St = 0.40, Static Offset = 60°

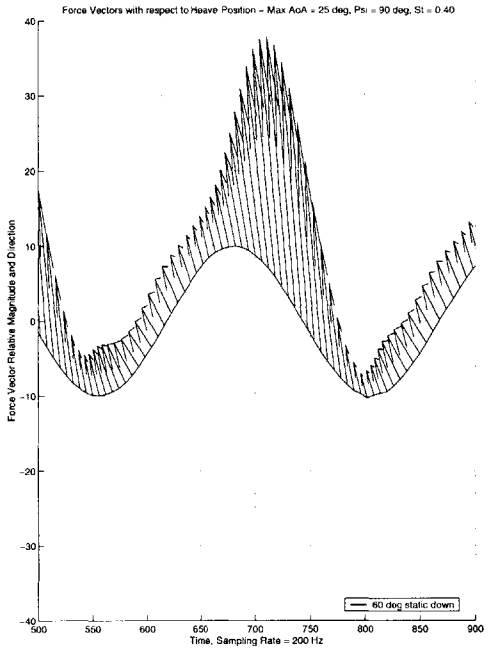

Figure B-12: Instantaneous Force Vectors for B-11

Appendix C

Impulse Start Time Data

In the following figures we show the raw data time traces for the impulse start experiments. These time traces show the unfiltered X and Y force data as well as the pitch and heave position recorded by the potentiometer and heave encoder, respectively. High frequency oscillation of the force signals occurs for all the heave velocities tested and is probably mechanical. Pitch overshoot for Method II runs is due to compliance and the very large forces created during these experiments.

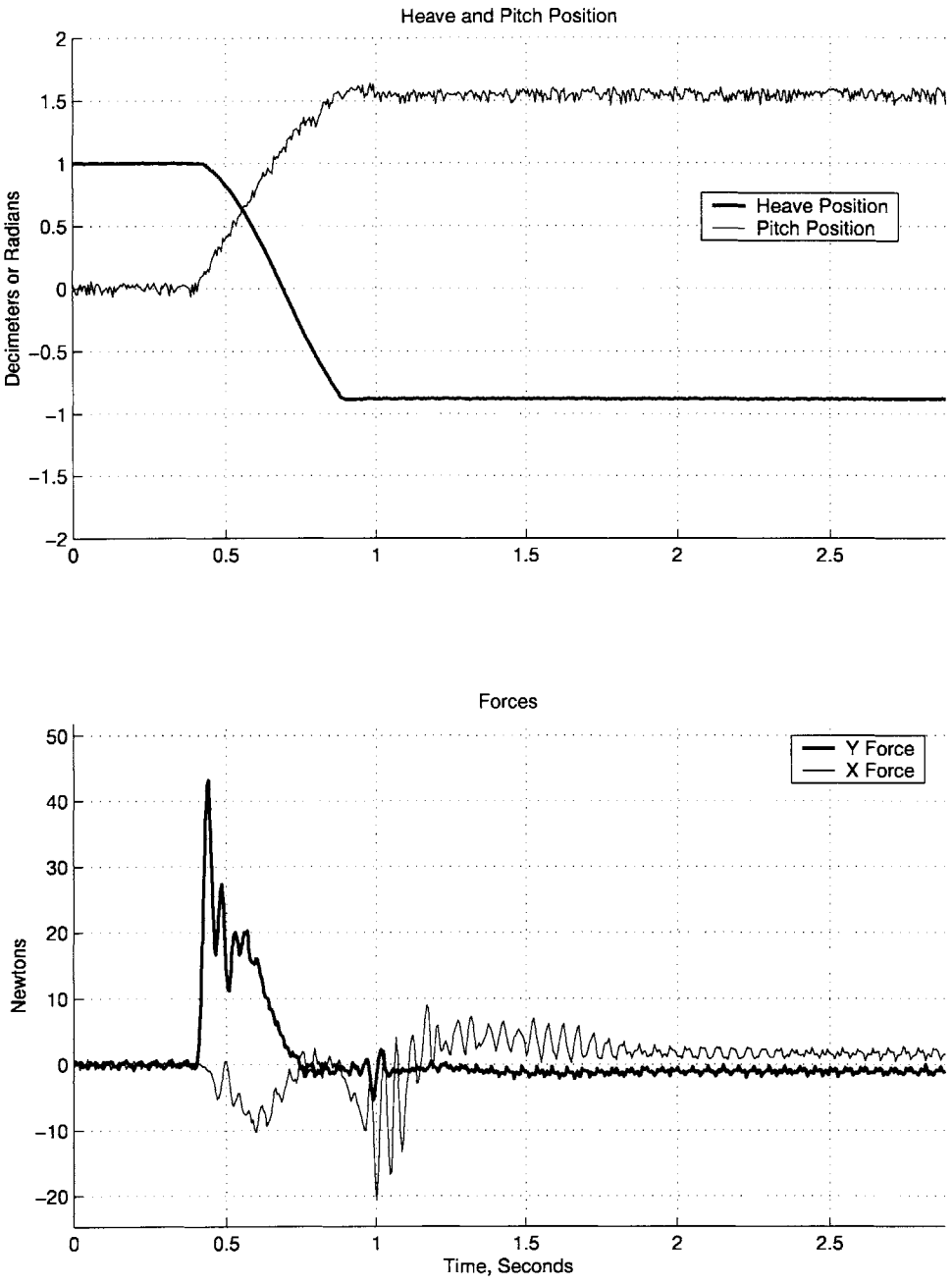

Figure C-1: Method I, Max Heave Velocity = .503 m/s

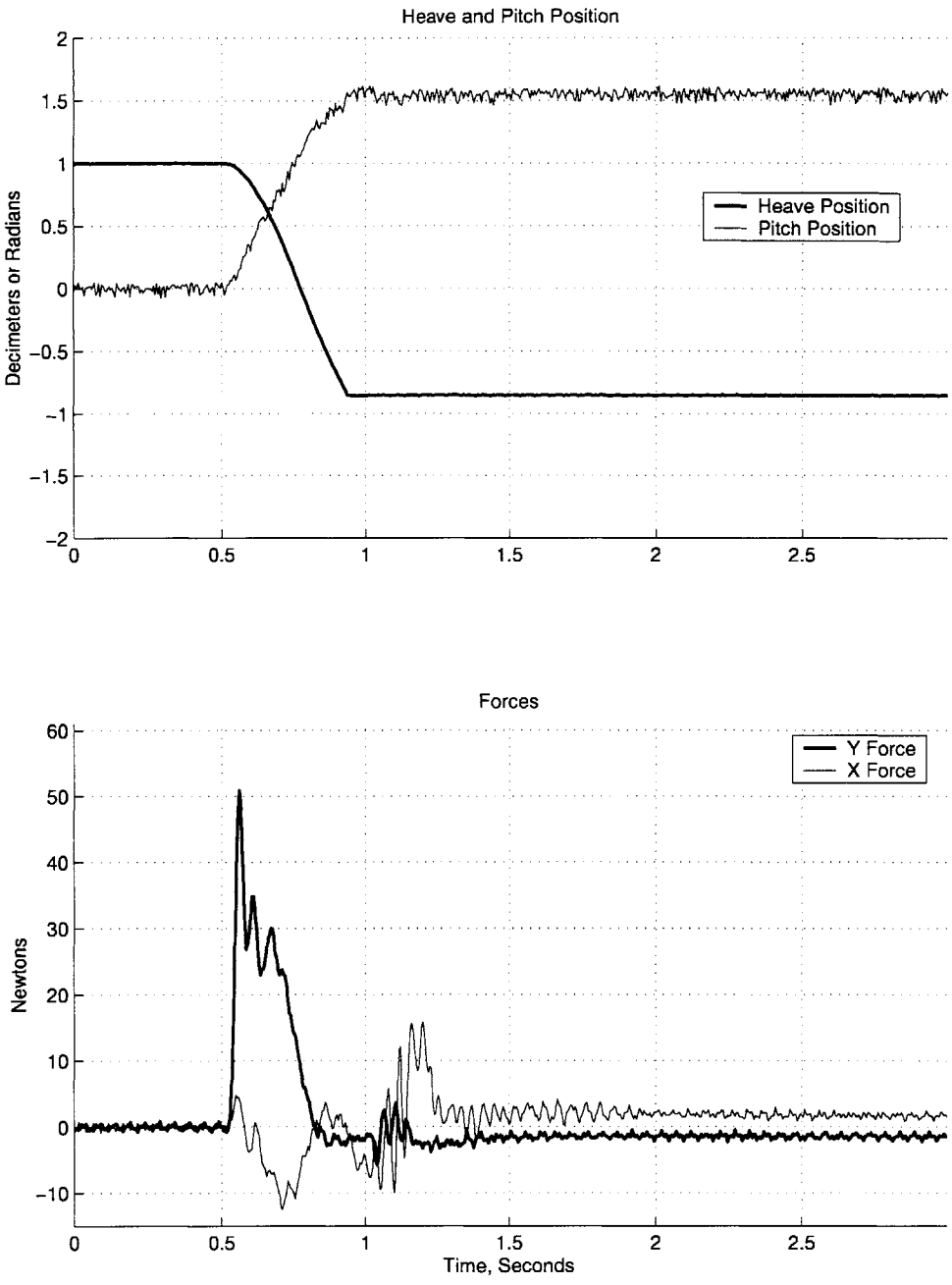

Figure C-2: Method I, Max Heave Velocity = .565 m/s

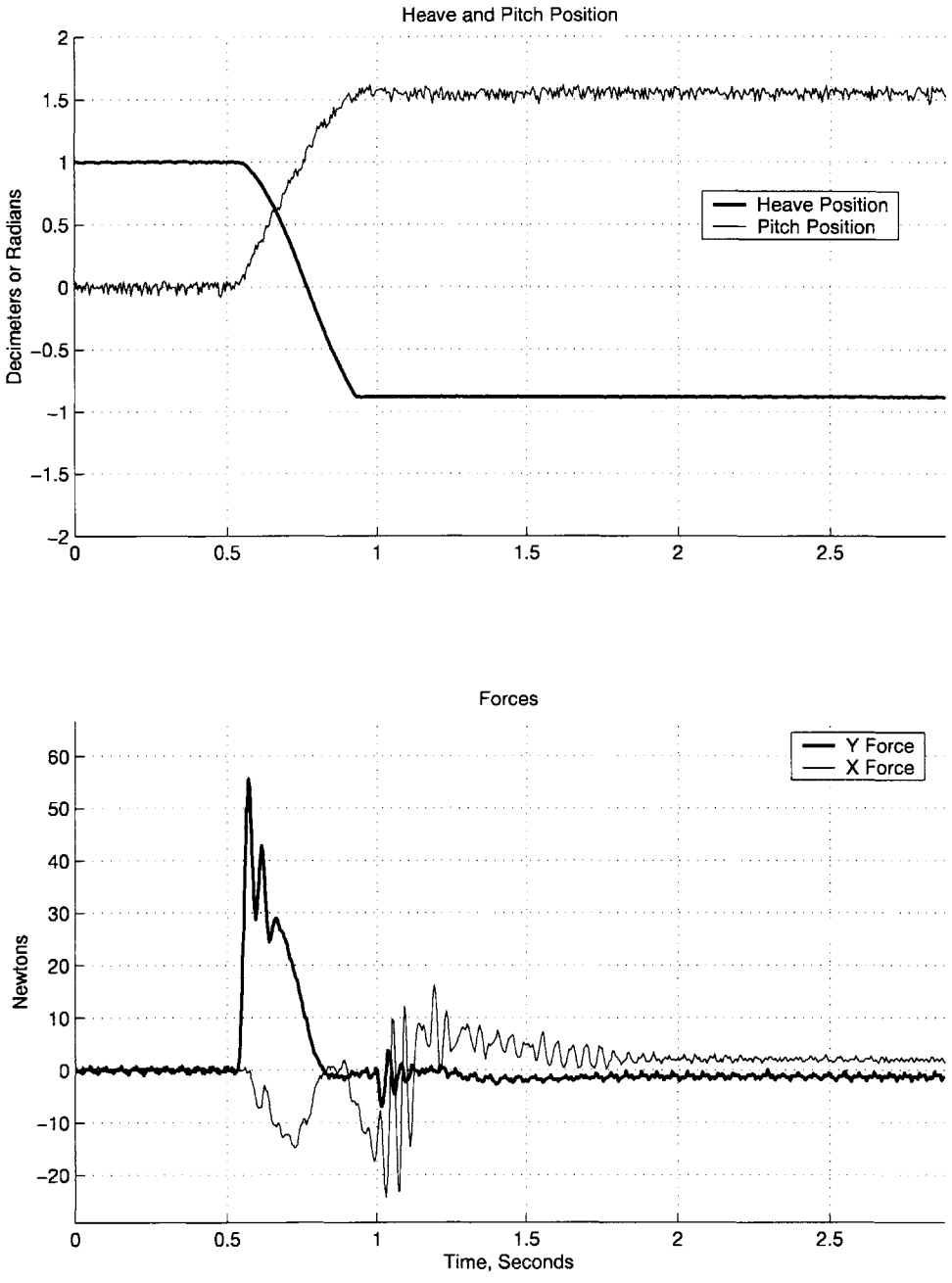

Figure C-3: Method I, Max Heave Velocity = .628 m/s

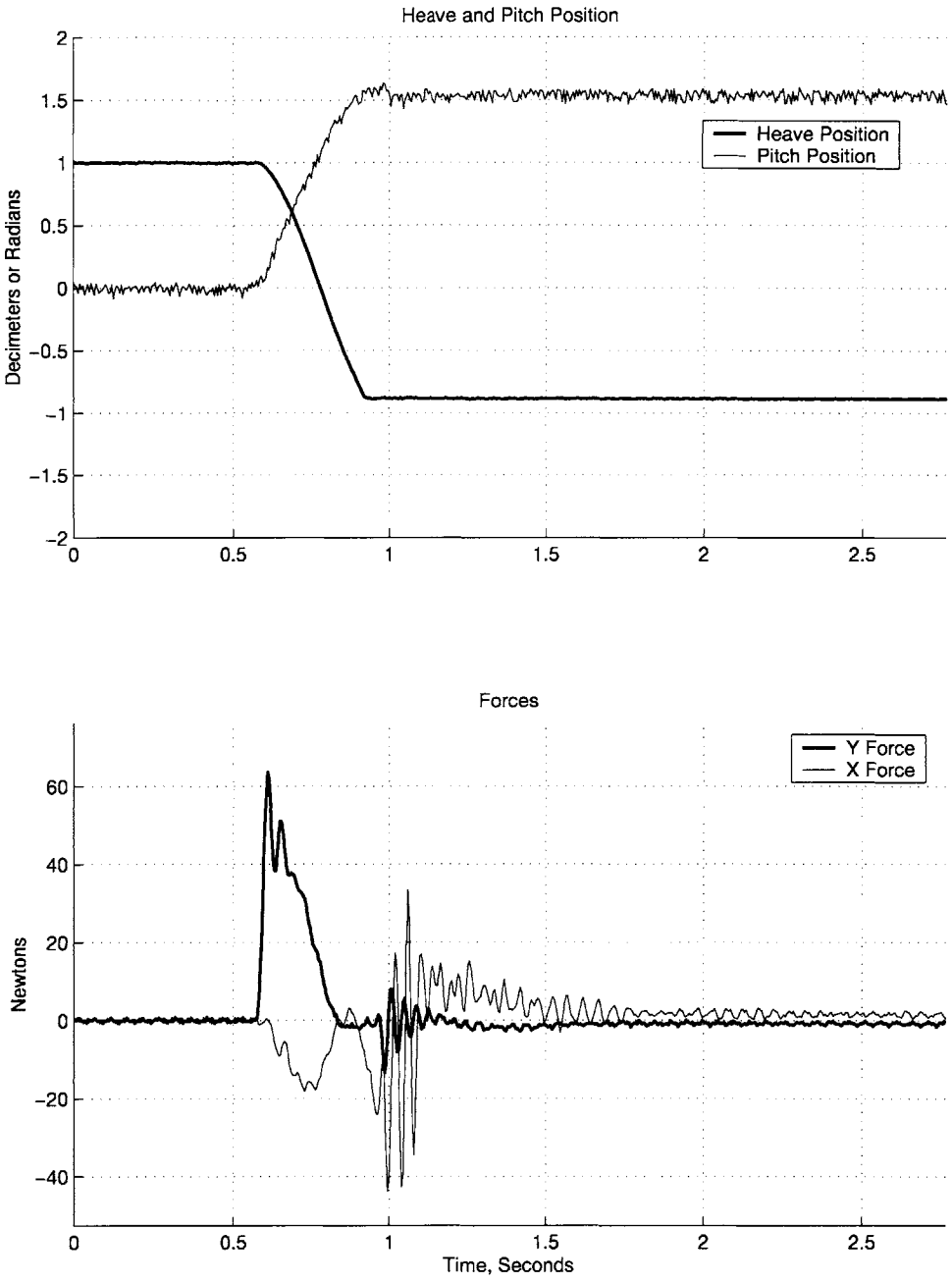

Figure C-4: Method I, Max Heave Velocity = .691 m/s

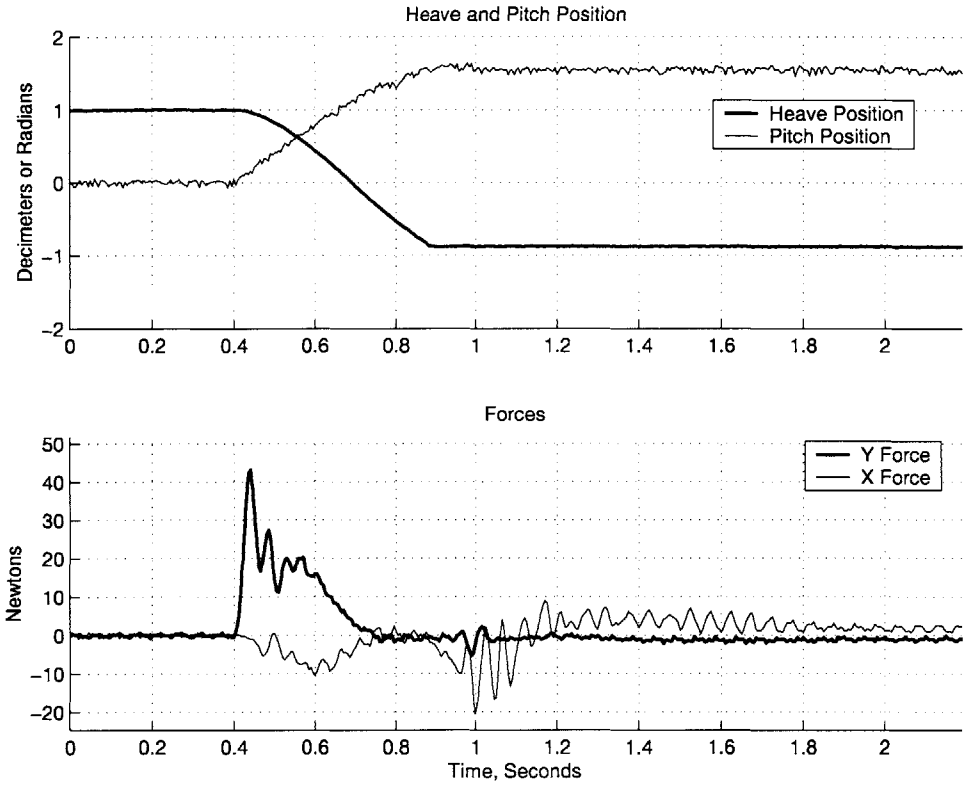

Figure C-5: Method I, Max Heave Velocity = .754 m/s

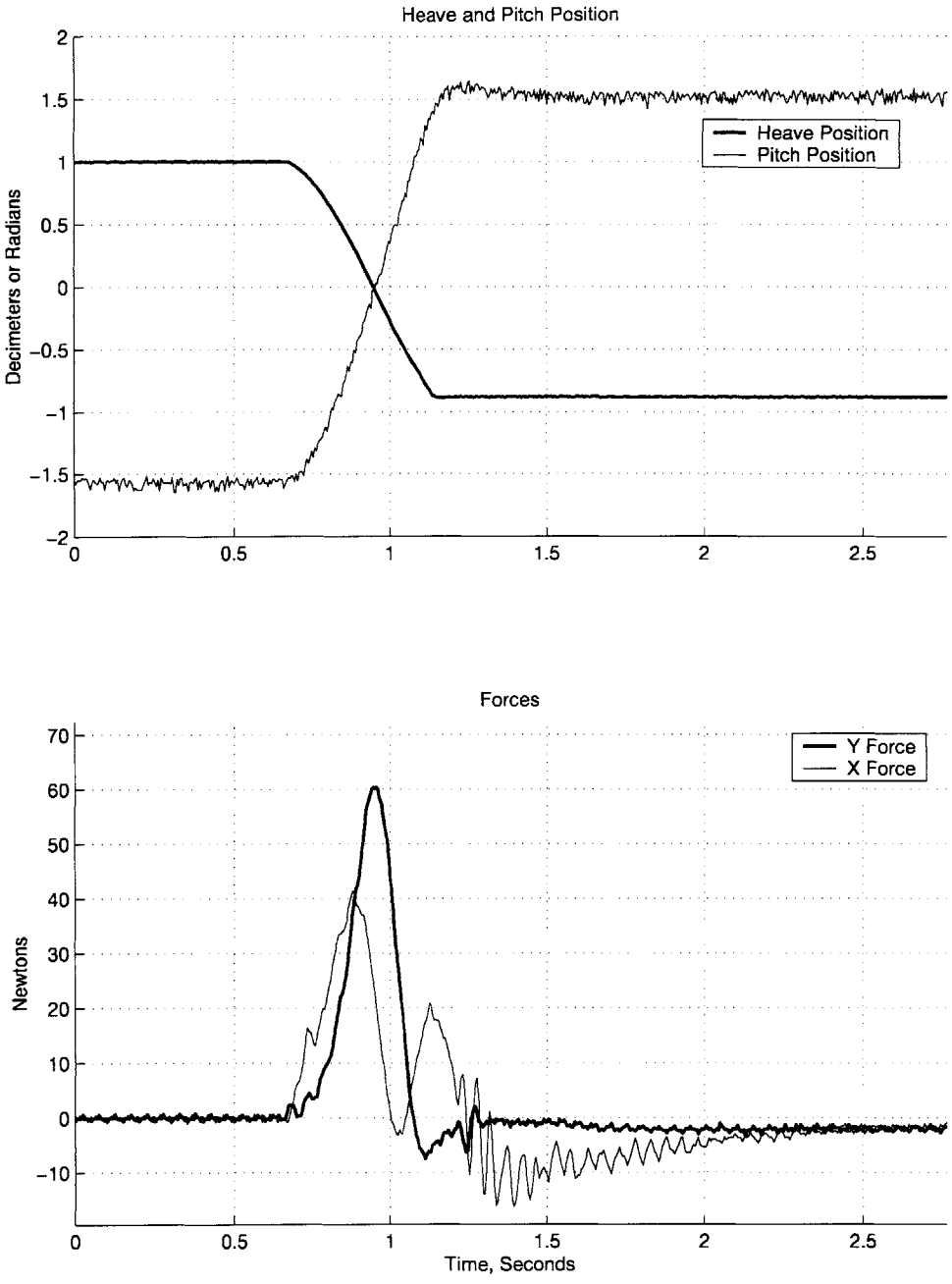

Figure C-6: Method II, Max Heave Velocity = .503 m/s

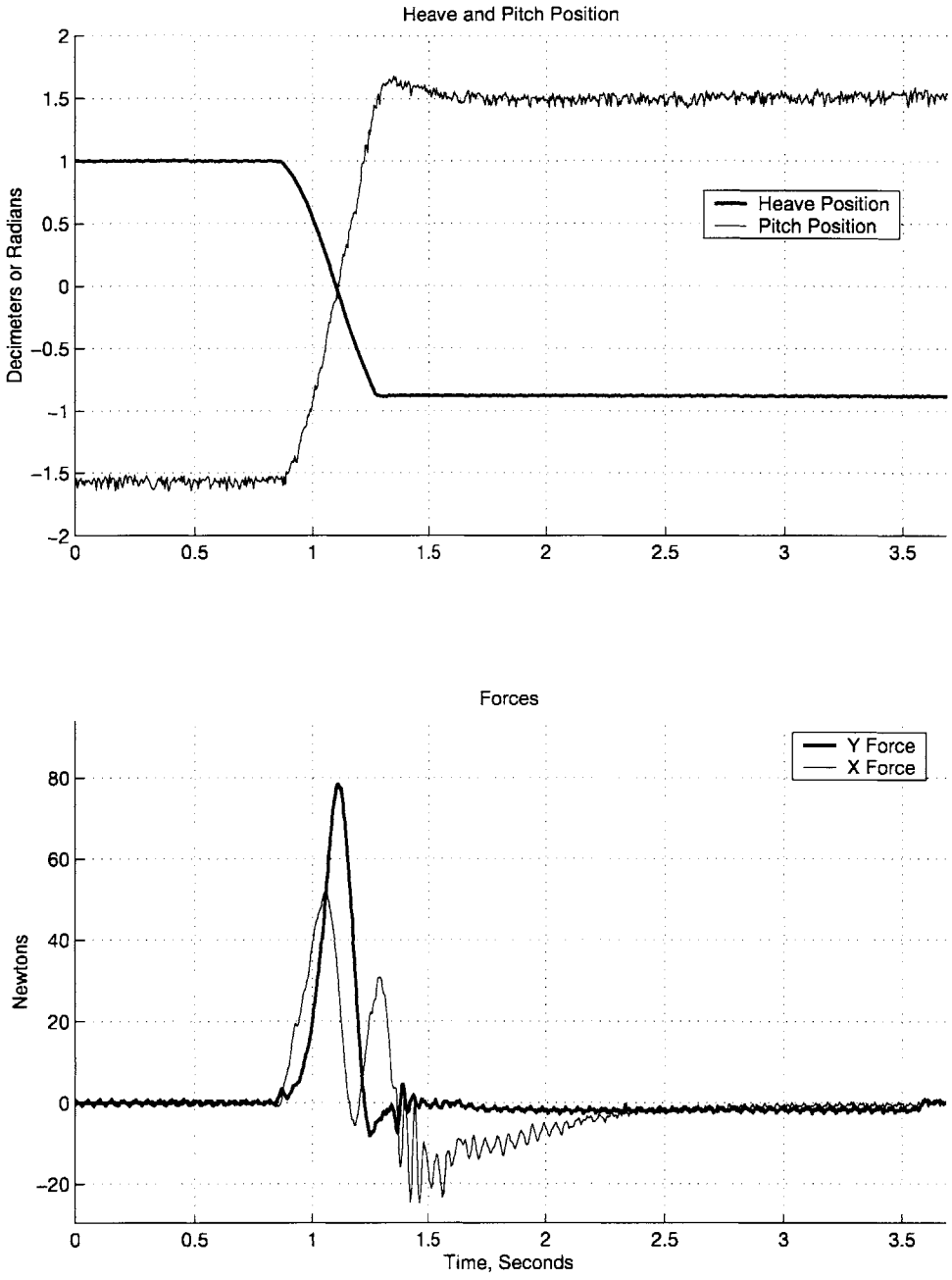

Figure C-7: Method II, Max Heave Velocity = .565 m/s

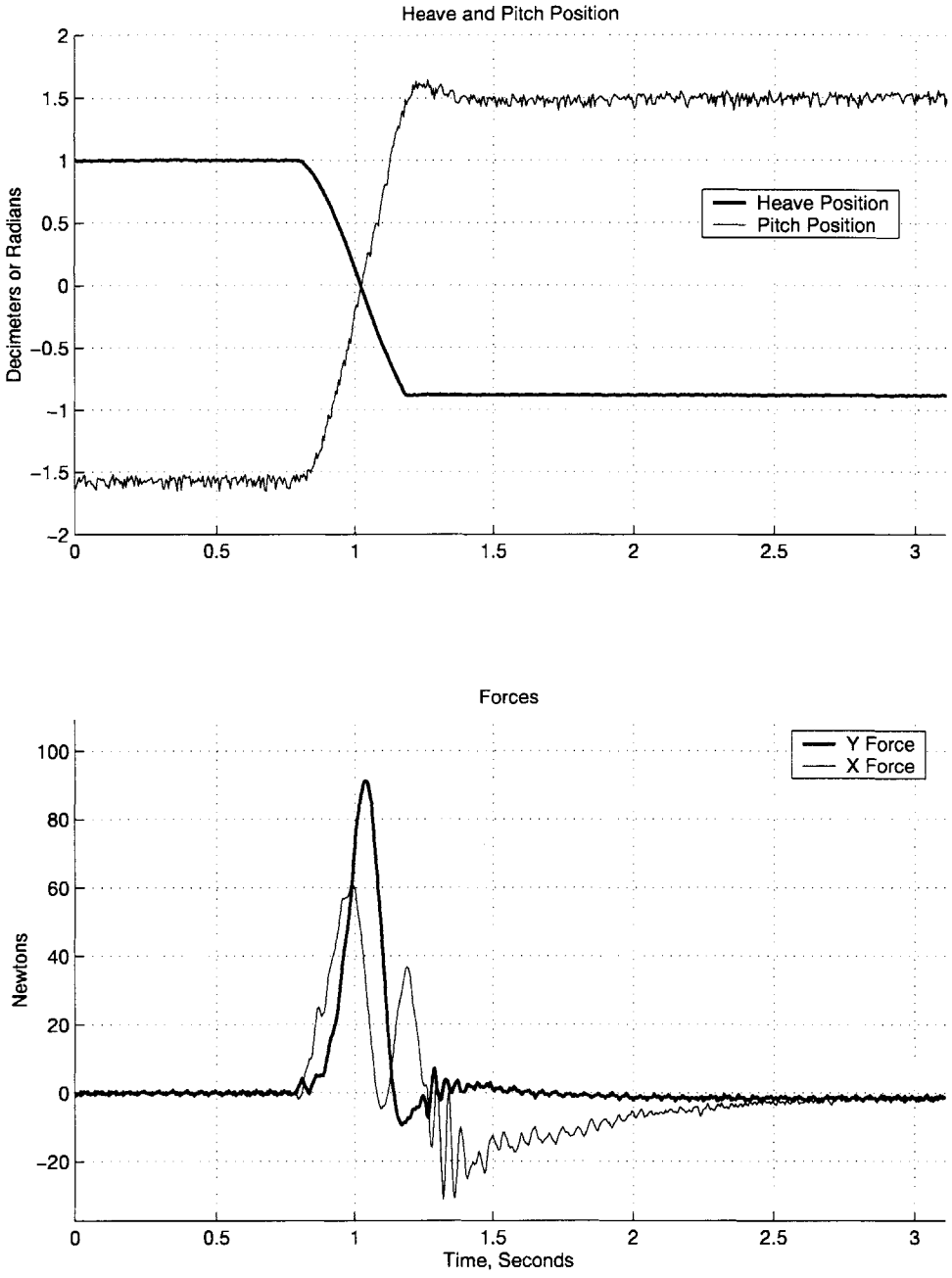

Figure C-8: Method II, Max Heave Velocity = .628 m/s

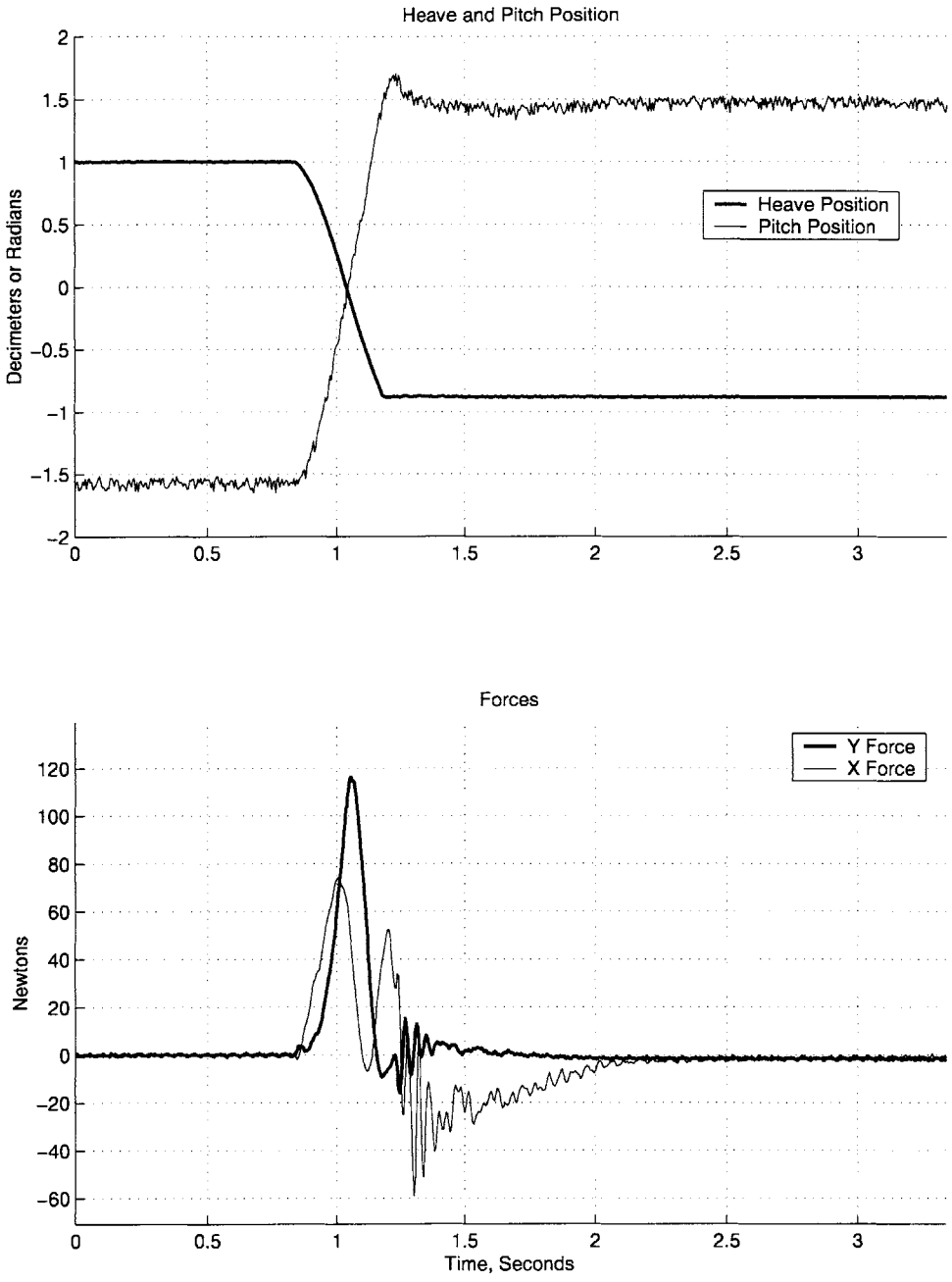

Figure C-9: Method II, Max Heave Velocity = .692 m/s

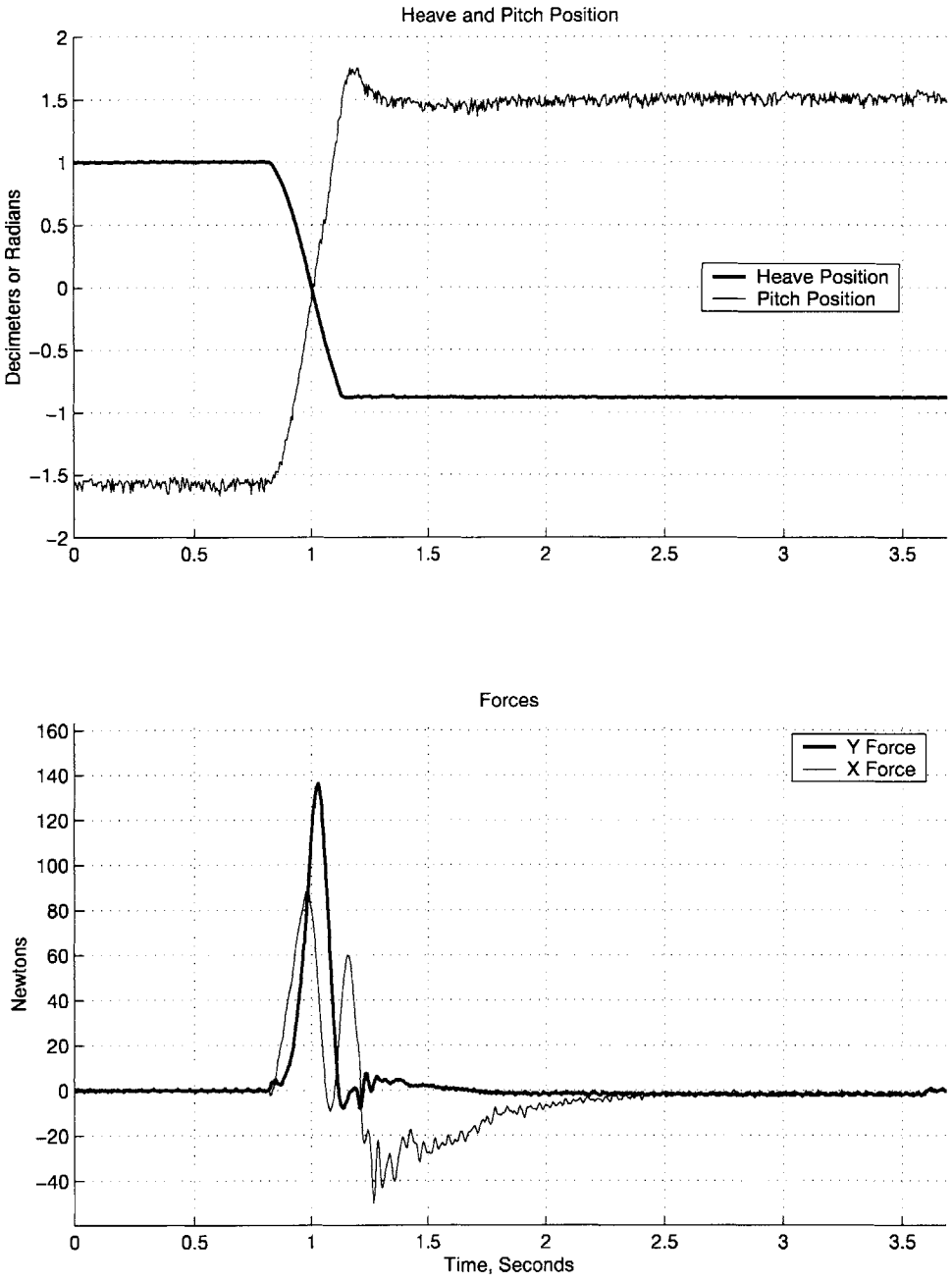

Figure C-10: Method II, Max Heave Velocity = .754 m/s

Appendix D

Strouhal Number Corrections

In these plots we show correction factors for calculating trailing edge Strouhal number for various phase angles and maximum angles of attack.

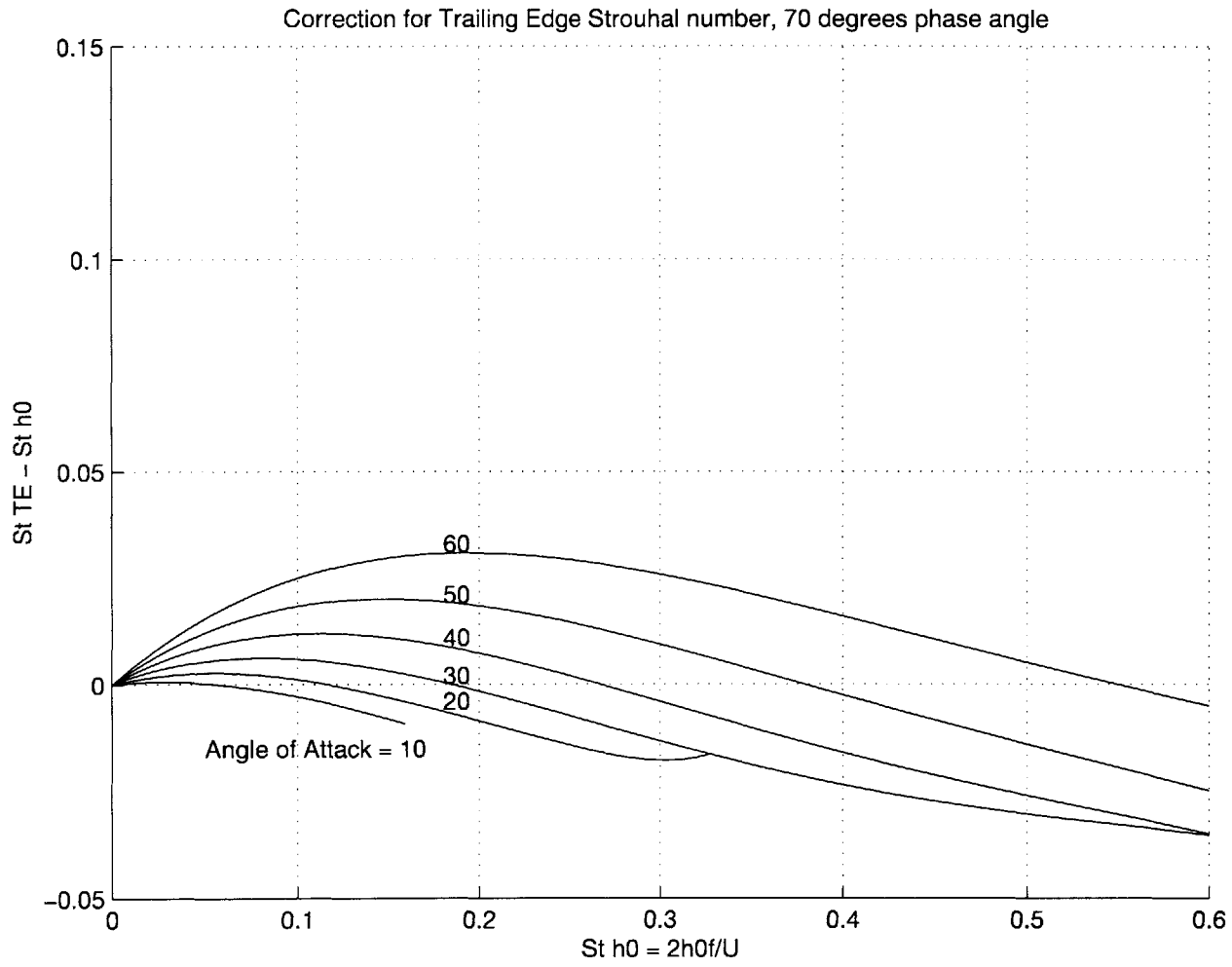

Figure D-1: Strouhal number correction, $\psi = 70°$

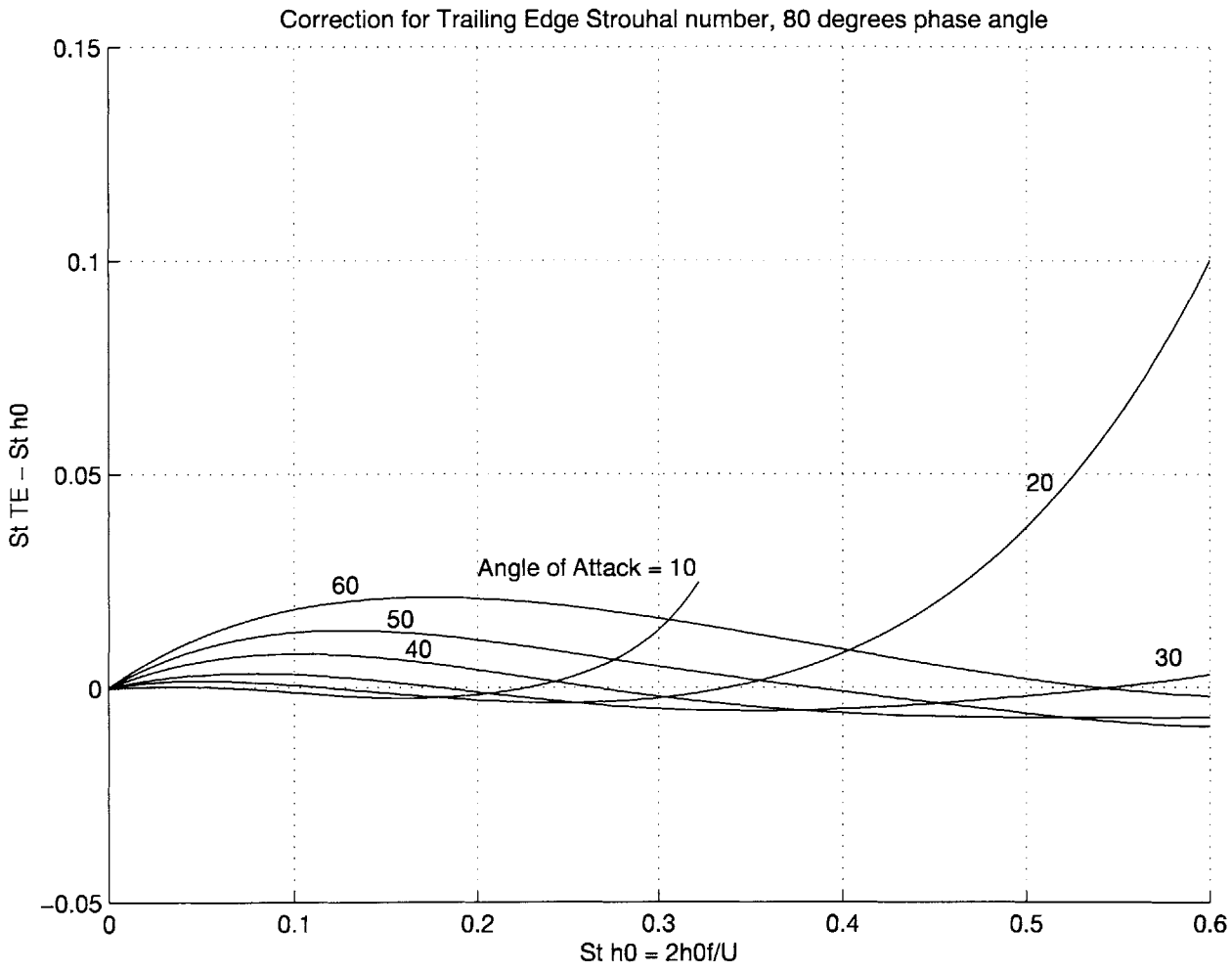

Figure D-2: Strouhal number correction, $\psi = 80°$

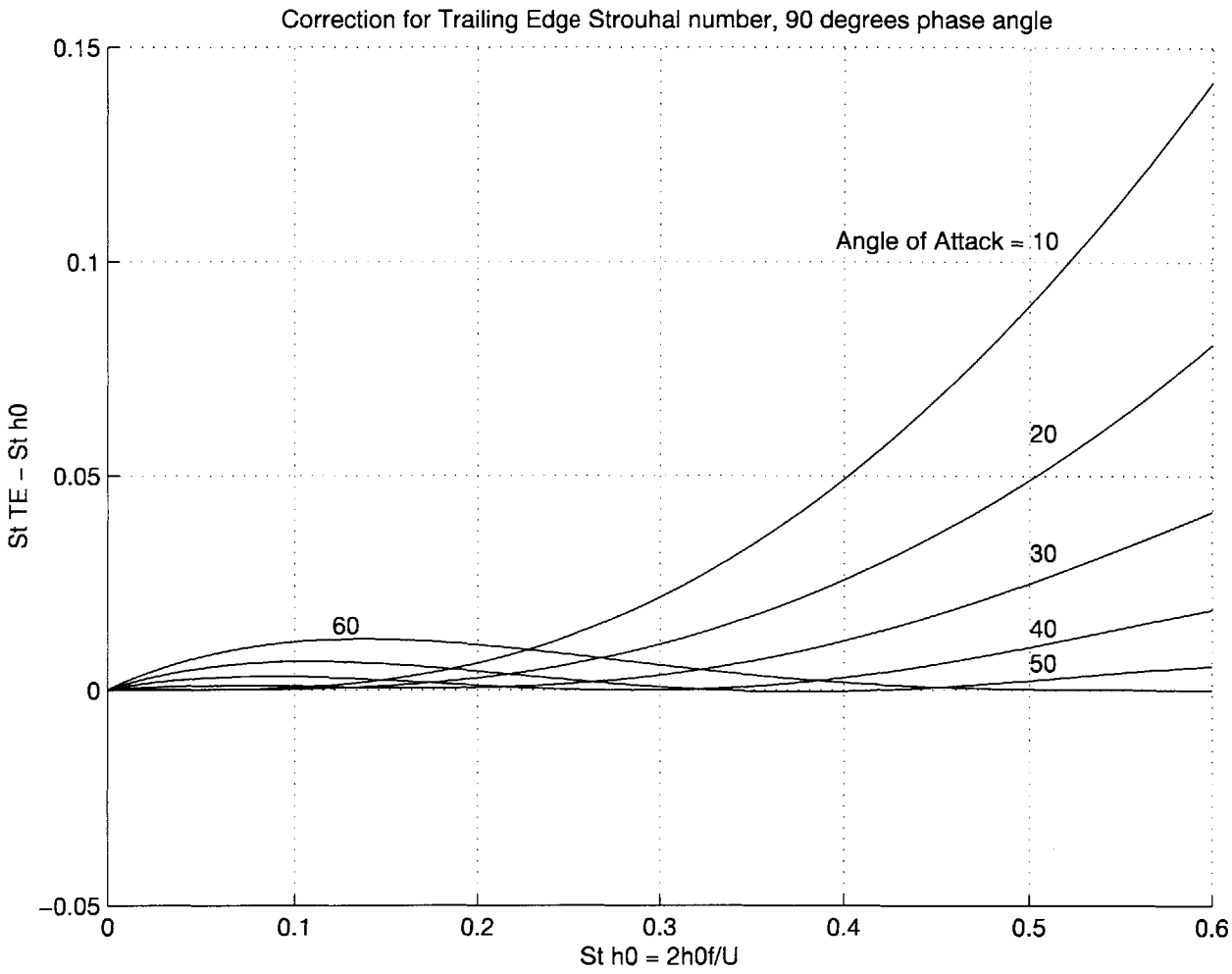

Figure D-3: Strouhal number correction, $\psi = 90°$

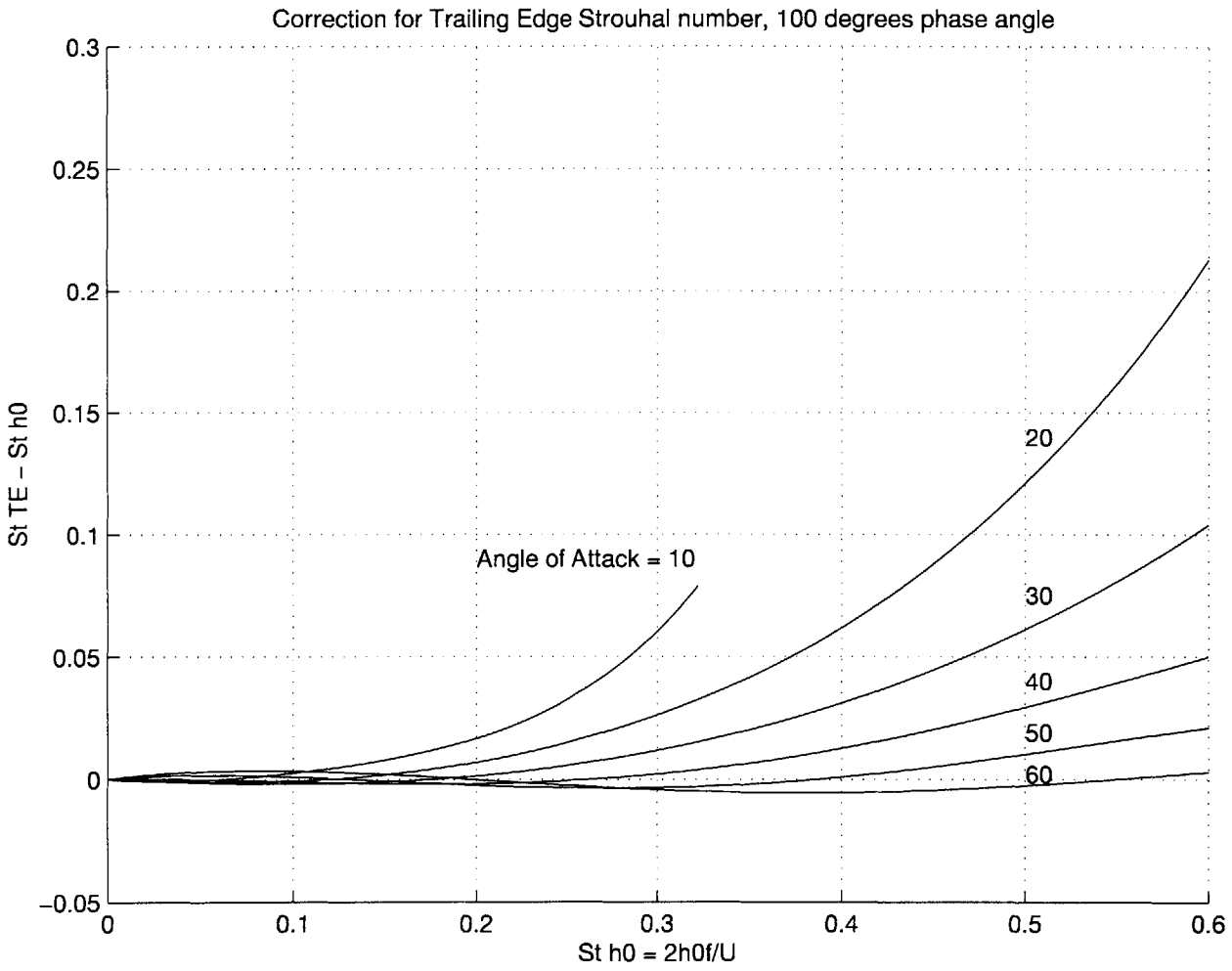

Figure D-4: Strouhal number correction, $\psi = 100°$

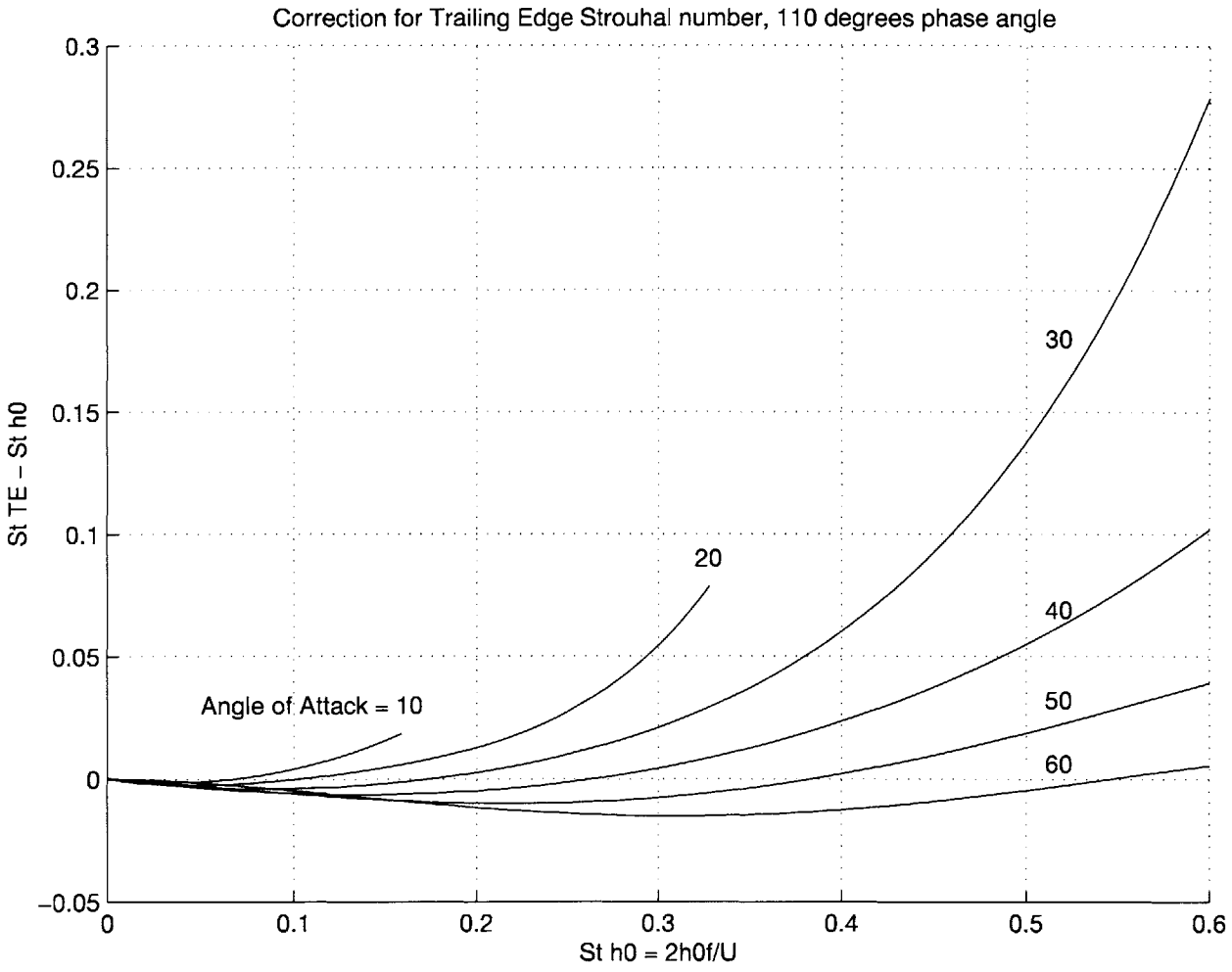

Figure D-5: Strouhal number correction, $\psi = 110°$

Bibliography

[1] J.M. Anderson. *Vorticity Control for Efficient Propulsion.* PhD thesis, Massachusetts Institute of Technology, 1996.

[2] P. Freymuth. Propulsive vortical signature of plunging and pitching airfoils. *AIAA Journal*, 26:881–883, 1988.

[3] I. Gursul and C.M Ho. High aerodynamic loads on an airfoil submerged in an unsteady stream. *AIAA Journal*, 30:1117–1119, 1992.

[4] M.M. Koochesfahani and P. Dimotakis. A cancellation experiment in a forced turbulent shear layer. *AIAA Journal*, 88:3713, 1988.

[5] M.J. Lighthill. Aquatic animal propulsion of high hydrodynamic efficiency. *Journal of Fluid Mechanics*, 44:265–301, 1970.

[6] Sir James Lighthill. *Mathematical Biofluiddynamics.* Society for Industrial and Applied Mathematics, Philadelphia, PA, 1975.

[7] G.S. Triantafyllou, M.S. Triantafyllou, and M.A. Grosenbaugh. Optimal thrust development in oscillating foils with application to fish propulsion. *Journal of Fluids and Structures*, 7:205–224, 1993.

[8] M.S. Triantafyllou, D.S. Barrett, K. Streitlien, and J.M Anderson. Flapping foils of high propulsive efficiency. *(submitted)*, 1996.

[9] M.S. Triantafyllou, G.S. Triantafyllou, and R. Gopalkrishnan. Wake mechanics for thrust generation in oscillating foils. *Physics of Fluids*, 3:2835–2837, 1991.